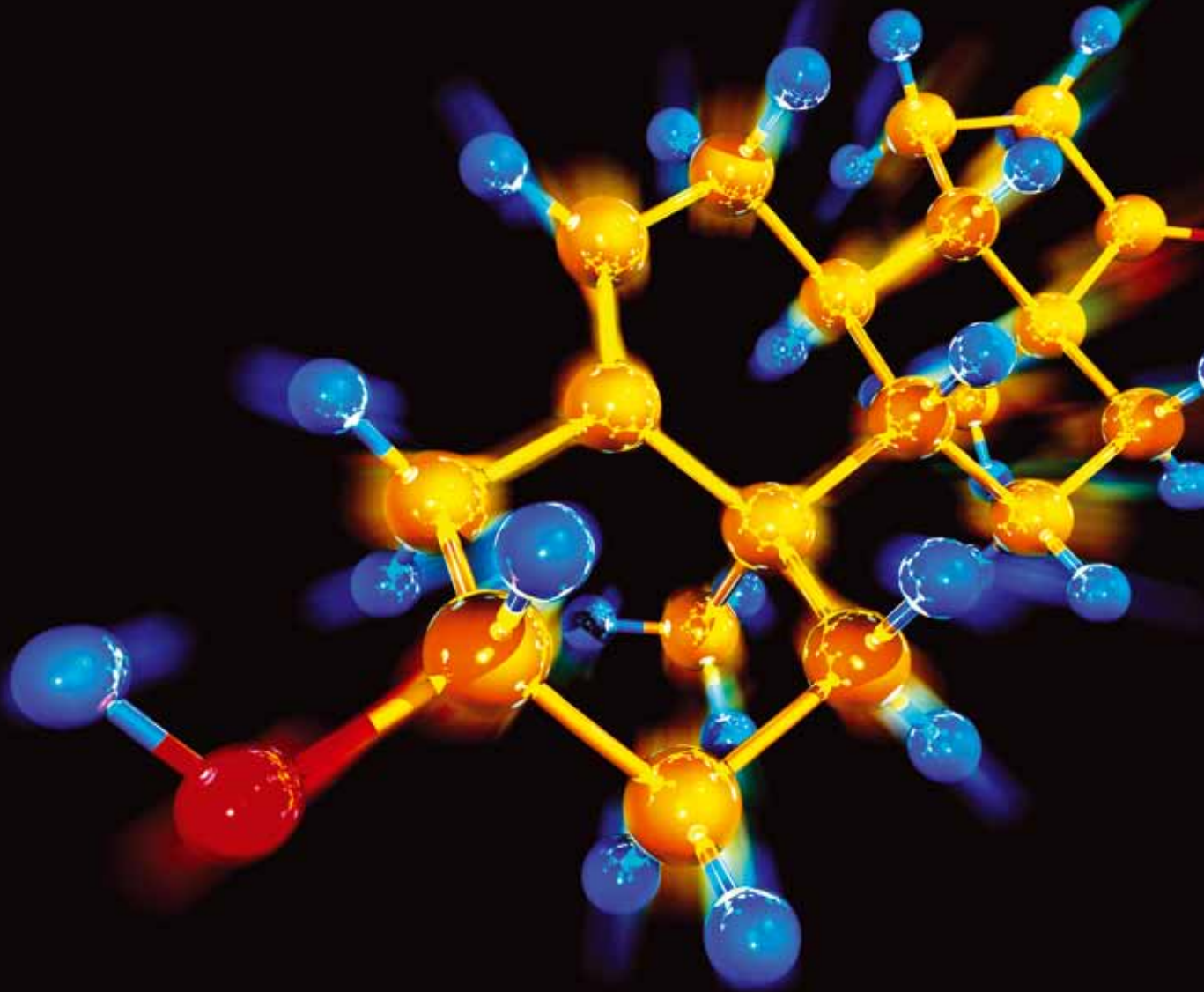


# Molecular Modeling: Advancements and Applications

Guest Editors: André Silva Pimentel, Cristiano R. W. Guimarães, Sebastian O. Danielache, and Yifat Mille





---

# **Molecular Modeling: Advancements and Applications**

## **Molecular Modeling: Advancements and Applications**

Guest Editors: André Silva Pimentel, Cristiano R. W. Guimarães,  
Sebastian O. Danielache, and Yifat Miller



---

Copyright © 2013 Hindawi Publishing Corporation. All rights reserved.

This is a special issue published in "Journal of Chemistry." All articles are open access articles distributed under the Creative Commons Attribution License, which permits unrestricted use, distribution, and reproduction in any medium, provided the original work is properly cited.

# Contents

**Molecular Modeling: Advancements and Applications**, André Silva Pimentel,  
Cristiano R.W. Guimarães, and Yifat Miller  
Volume 2013, Article ID 875478, 2 pages

**Molecular Modeling and Spectroscopic Studies on the Interaction of Transresveratrol with Bovine Serum Albumin**, Xiaoli Liu, Yonghui Shang, Xudong Ren, and Hua Li  
Volume 2013, Article ID 494706, 7 pages

**The Uptake Mechanism of the Cell-Penetrating pVEC Peptide**,  
Ihsan Omur Akdag and Elif Ozkirimli  
Volume 2013, Article ID 851915, 9 pages

**Toward Structure Prediction for Short Peptides Using the Improved SAAP Force Field Parameters**,  
Kenichi Dedachi, Taku Shimosato, Toshiya Minezaki, and Michio Iwaoka  
Volume 2013, Article ID 407862, 13 pages

**Influence of Pyrazine Ring Doping on the  $^{15}\text{N}$  and  $^{11}\text{B}$  NMR and Electronic Structure Parameters in Zigzag Boron Nitride Nanotube: A DFT Study**, Sattar Arshadi, Ameneh Asghari,  
Hojatollah Raheimi, and Saboora Abedini  
Volume 2013, Article ID 948010, 10 pages

**Nuclear Magnetic Resonance Parameters of Pure and Diborinin-Doped (6,0) Single-Walled Zigzag BNNT: DFT Study**, Sattar Arshadi, Saboora Abedini, Ameneh Asghari,  
and Fatemeh Alipour Zaghmarzi  
Volume 2013, Article ID 421091, 9 pages

**ITP Adjuster 1.0: A New Utility Program to Adjust Charges in the Topology Files Generated by the PRODRG Server**, Diogo de Jesus Medeiros, Wilian Augusto Cortopassi, Tanos Celmar Costa França,  
and André Silva Pimentel  
Volume 2013, Article ID 803151, 6 pages

**On the Difference between Self-Assembling Process of Monomeric and Dimeric Surfactants with the Same Head to Tail Ratio: A Lattice Monte Carlo Simulation**,  
Reza Behjatmanesh-Ardakani and Maryam Farsad  
Volume 2013, Article ID 525948, 7 pages

**Adsorption of Trinitrotoluene on a MgO(001) Surface Including Surface Relaxation Effects**,  
Thiago Guerra and Itamar Borges Jr.  
Volume 2013, Article ID 359202, 8 pages

## Editorial

# Molecular Modeling: Advancements and Applications

**André Silva Pimentel,<sup>1</sup> Cristiano R. W. Guimarães,<sup>2</sup> and Yifat Miller<sup>3</sup>**

<sup>1</sup> Departamento de Química, Pontifícia Universidade Católica do Rio de Janeiro, 22451-900 Rio de Janeiro, RJ, Brazil

<sup>2</sup> Pfizer Worldwide Research & Development, Cambridge, MA 02139, USA

<sup>3</sup> Department of Chemistry, Ben-Gurion University of the Negev, 84105 Be'er-Sheva, Israel

Correspondence should be addressed to André Silva Pimentel; [a.pimentel@puc-rio.br](mailto:a.pimentel@puc-rio.br)

Received 12 May 2013; Accepted 12 May 2013

Copyright © 2013 André Silva Pimentel et al. This is an open access article distributed under the Creative Commons Attribution License, which permits unrestricted use, distribution, and reproduction in any medium, provided the original work is properly cited.

Molecular modeling (MM) is one of the fastest growing fields in science. It may vary from building and visualizing simple molecules in three dimensions (3D) to performing complex computer simulations on large proteins and nanostructures. MM is a collection of computer-based techniques for driving, representing and manipulating the structures and reactions of molecules, and those properties that are dependent on these 3D structures. The techniques in MM cover several issues among them computational chemistry, drug design, computational biology, nanostructures, and material science.

This issue compiles eight papers that deal with five issues: new techniques in MM, computational chemistry, computational biology, nanostructures, and material science.

Two new techniques are described in this issue. The first technique is presented by D. J. Medeiros et al. who developed a utility program to compute *ab initio* charges of each atom for relatively large molecules. The second technique is presented by K. Dedachi et al. that developed a new all-atom force-field in applications for 3D structural prediction for short peptides.

Two papers that are related to computational chemistry in this issue are by S. Arshadi et al. One paper illustrates the applications of density functional theory (DFT) to investigate the properties of the electronic structure of Zigzag boron nitride nanotubes and two models of diborinin-doped boron nitride nanotube. The second paper presents the applications of DFT to investigate the electronic structure of pyrazine-doped nitride nanotubes and to compute the nuclear magnetic resonance (NMR) parameters of these structures.

One of the new fields in MM is the study of the self-assembly of molecules that forms nanostructures. The paper

by R. Behjatmanesh-Ardakani and M. Farsad illustrate a MM of critical micelle concentration for a single chain and a double chain of a surfactant with amphiphilic properties. The self-assembly processes of the single chain and the double chain surfactants are compared using Monte-Carlo simulations.

Two papers deal with computational biology in aim to understand biological mechanisms. One paper by X. Liu et al. demonstrates the interaction mechanism of trans-resveratrol with bovine serum albumin using a combination of MM techniques and spectroscopic methods. The second paper by I. O. Akdag and E. Ozkirimli demonstrates the applications of steered molecular dynamics simulations to examine the membrane translocation mechanism of the p-VEC peptide. This short peptide is derived from murine vascular endothelial-cadherin protein that functions in the physical contact between adjacent cells.

Finally, one of the main advancements in the last five years is the study of material science using MM. The paper by T. Guerra and I. Borges Jr. illustrates this advancement using a combination of DFT with periodic boundary conditions and generalized gradient approximation methods. The authors succeeded to describe the electronic charges density of the adsorbed 2,4,6-trinitrotoluene on a MgO (001) surface in aim to understand the interactions between the molecules and the surface. This issue does not include peer-reviewed articles on drug design. Yet, we found that the issue drug design is an interactive topic in MM and contribute to drug discovery both in academia and in industry. Computer-aided and structure-based drug design relies on knowledge of the

3D structure of the biological target. Drug design is an iterative process that begins when a compound is identified to display an interesting biological profile and ends when its activity profile and the chemical synthesis are optimized. Today, MM permeates all aspects of drug design. Scientists have used computer models of new chemical entities to help define activity profiles, geometries, and relativities. Three stages of drug discovery can be achieved by MM: virtual screening, hit-to-lead optimization of affinity and selectivity, and lead optimization of other pharmaceutical properties while maintaining affinity.

We thoroughly reviewed these papers and we believe that they contribute to the advancements and the applications of new MM techniques for both chemical and biological molecules. Moreover, we believe that the papers in this special issue will be milestones of the advancement for the next generation of MM researchers.

*Yifat Miller*  
*Cristiano R. W. Guimarães*  
*André S. Pimentel*

## Research Article

# Molecular Modeling and Spectroscopic Studies on the Interaction of Transresveratrol with Bovine Serum Albumin

Xiaoli Liu,<sup>1,2</sup> Yonghui Shang,<sup>3</sup> Xudong Ren,<sup>4</sup> and Hua Li<sup>4</sup>

<sup>1</sup> College of Life Sciences, Northwest University, Xi'an 710069, China

<sup>2</sup> College of Environmental Science and Engineering, Chang'an University, Xi'an 710054, China

<sup>3</sup> Department of Chemistry, Xi'an Normal College, Xi'an 712000, China

<sup>4</sup> College of Chemistry and Materials Science, Northwest University, Xi'an 710069, China

Correspondence should be addressed to Hua Li; [nwufxkx2012@126.com](mailto:nwufxkx2012@126.com)

Received 7 January 2013; Revised 25 February 2013; Accepted 2 March 2013

Academic Editor: André Silva Pimentel

Copyright © 2013 Xiaoli Liu et al. This is an open access article distributed under the Creative Commons Attribution License, which permits unrestricted use, distribution, and reproduction in any medium, provided the original work is properly cited.

The interaction of transresveratrol (TRES) with bovine serum albumin (BSA) has been investigated by ultraviolet-visible, fluorescence, Fourier transform infrared spectroscopic methods and molecular modeling techniques. The fluorescence results show that the intrinsic fluorescence of BSA is quenched by TRES through a static quenching procedure. The binding constants of TRES with BSA at 292, 297 and 302 K are calculated as  $10.22 \times 10^4$ ,  $8.71 \times 10^4$ , and  $7.59 \times 10^4 \text{ L mol}^{-1}$ , respectively, and corresponding numbers of binding sites are approximately equal to unity. The thermodynamic parameters  $\Delta H$  and  $\Delta S$  are estimated to be  $-21.82 \text{ kJ mol}^{-1}$  and  $+21.15 \text{ J mol}^{-1} \text{ K}^{-1}$ , which indicates that the interaction of TRES with BSA is driven mainly by hydrophobic forces and there are also hydrogen bonds and electrostatic interactions. The competitive experiments suggest that the binding site of TRES to BSA is probably located on site II. The results of infrared spectra show that the binding of TRES with BSA leads to conformational changes of BSA, and the binding stabilizes the  $\alpha$ -helix and  $\beta$ -sheet at the cost of a corresponding loss in the  $\beta$ -turn structure of BSA. The results of molecular modeling calculation clarify the binding mode and the binding sites which are in good accordance with the experiment results.

## 1. Introduction

Serum albumins, the major soluble protein constituents in the blood stream, bind and transport several exogenous and endogenous molecules like fatty acids, nutrients, steroids, and a large list of drugs. The formed complexes are involved in transport and regulatory processes. Since most of the administered drugs bind extensively and reversibly to serum albumins and drugs are transported mainly as complexes with proteins, the biological activities of the drug such as the overall distribution, metabolism, and efficacy in the body are correlated with their affinities towards serum albumins. Therefore, protein-drug interaction has an enormous biological interest and has been found to play a significant role in pharmacology [1]. Among the serum albumins, bovine serum albumin (BSA) is an appropriate protein model for studying the interaction between serum albumins and drugs because of its medically important, unusual ligand-binding

properties, low cost, availability, and structural homology with human serum albumin (HSA) [2, 3].

Transresveratrol (trans-3,5,4'-trihydroxystilbene, TRES) is a polyphenolic natural product existing in a variety of plant species including *Polygonum cuspidatum*, grapes, peanuts, and various berries. TRES has been shown to prevent or slow the progression of a wide variety of diseases, including cancer, cardiovascular disease, ischemic injuries, and Alzheimer's disease [4–8]. These properties accompanied with the lack of harmful effects make TRES attractive as a phytoalexin. The molecular structure of TRES is provided in Figure 1. So far, most researches are focusing on its pharmacological activities; only a little has been done on the interaction of TRES with serum albumin. Li et al. [9], Wei et al. [10], and Cao et al. [11] had reported the interaction between resveratrol and BSA, but the binding site of TRES on BSA had not been identified, the changes of secondary structure of BSA had not been quantitatively analyzed, and the binding

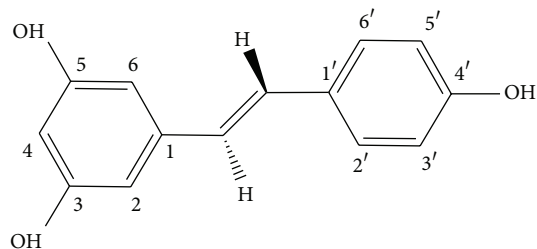


FIGURE 1: Molecular structure of TRES.

had not been calculated by molecular modeling techniques. In this paper, the interaction of TRES with BSA is investigated in detail with the purpose to provide basic information for pharmaceutical applications of TRES.

In this work, the interaction of TRES with BSA has been investigated under imitated physiological conditions via spectroscopic methods and molecular modeling techniques. Fluorescence and UV-vis spectroscopy were employed to understand the quenching mechanism of BSA-TRES binding. The binding constants, number of binding sites, and thermodynamic parameters have been calculated, and the binding site of TRES on BSA was identified by fluorescence displacement experiments. Furthermore, Fourier transform infrared (FTIR) spectroscopy was used to demonstrate the conformational changes of BSA, and the changes of secondary structure were quantitatively analyzed by the curve fitting method. In addition, the molecular modeling was used to improve the understanding of the interaction of TRES with BSA.

## 2. Experimental

**2.1. Materials.** BSA was purchased from Huamei Bioengineering Company (Shanghai, China). TRES was obtained from Xi'an Sino-Herb Biotechnology Company (Xi'an, China). All other reagents were analytical-reagent grade, and double-distilled water was employed for solutions.

**2.2. Fluorescence and UV-Vis Experiments.** The fluorescence experiments were performed with an F-4500 fluorescence spectrophotometer (Hitachi). For different samples, the concentrations of BSA were constant at  $3 \times 10^{-7} \text{ mol L}^{-1}$  and the concentrations of TRES were alterable and ranged from 0 to  $2.4 \times 10^{-6} \text{ mol L}^{-1}$ . Fluorescence quenching spectra were measured at 292, 297 and 302 K with exciting wavelength of 280 nm. The UV-vis absorption experiments were performed on a UV-2450 spectrophotometer (Shimadzu, Japan).

**2.3. Displacement Experiments.** The displacement experiments were performed using three different site probes, namely, phenylbutazone, flufenamic acid, and digitoxin, for site I, II, and III, respectively. BSA and the site probe were added to colorimeter tube first, and the concentrations were constant at  $3 \times 10^{-7} \text{ mol L}^{-1}$  and  $2 \times 10^{-7} \text{ mol L}^{-1}$ , respectively. Then appropriate amount TRES was added to the BSA-phenylbutazone/flufenamic acid/digitoxin systems.

**2.4. FTIR Experiments.** FTIR spectra were measured on a Vertex 70 FTIR spectrometer (Bruker Optics, Germany). All FTIR spectra were taken via the attenuated total reflection method. The spectra processing procedure involved collecting spectra of Tris-HCl buffer solution, BSA solution, TRES solution, and BSA-TRES solution under the same conditions. Next, the absorbance of the buffer solution was subtracted from the spectrum of the BSA solution to obtain the spectrum of free BSA, and the absorbance of the TRES solution was subtracted from the spectrum of the BSA-TRES solution to obtain the spectrum of the BSA after interaction. At last, the two difference spectra were compared and analyzed.

**2.5. Molecular Modeling.** The crystal structure of BSA was obtained from protein databank (PDB) (<http://www.rcsb.org/pdb>, PDB ID: 3V03), the PDB file was imported into AutoDock Tools, all water molecules were removed, and Kollman charges and solvation parameters were added. The initial 3D structures of TRES were generated by ChemSketch software, and the geometries of TRES were subsequently optimized using GAMESS software on DFT/B3LYP/6-31G level. AutoDock4.2 (<http://autodock.scripps.edu>) program was applied to calculate the interaction modes between TRES and BSA. First the grid box was set as  $126 \times 100 \times 126$  points with a grid spacing of  $0.560 \text{ \AA}$ , whole protein was covered, and the initial search was carried out. The region of the most populated of the first five clusters was selected as the probable binding region. Then the accurate search was executed in the probable binding region with a smaller grid map. Lamarckian genetic algorithm was applied in the docking. 100 genetic algorithm (GA) runs were performed with the following parameters: population size of 150, maximum number of  $2.5 \times 10^6$  energy evaluations, and maximum number of 27,000 generations, and other parameters were default. The resulting conformations were clustered using a root-mean-square deviation (RMSD) of  $2.0 \text{ \AA}$  and the clusters were ranked in order of increasing binding energy of the lowest binding energy conformation in each cluster. Finally the lowest energy conformation in the most populated of the first five clusters was used for docking analysis. The output from AutoDock was rendered with PyMOL.

## 3. Results and Discussion

**3.1. Fluorescence Quenching Mechanism.** The fluorescence spectra of BSA in the presence of different concentrations of TRES are shown in Figure 2. It is obvious that BSA has a strong fluorescence emission peak at about 347 nm, and the fluorescence intensity decreases gradually with increasing concentration of TRES, which indicates that TRES can interact with BSA and quench its intrinsic fluorescence. Furthermore, there is a slight red shift of maximum emission wavelength occurring with the addition of TRES, implying that the microenvironment around the chromophore of BSA is changed.

Fluorescence quenching can occur by different mechanisms, usually classified as dynamic quenching and static

TABLE 1: Stern-Volmer quenching constants for the interaction of TRES with BSA at different temperatures.

$T/K$	$K_{sv}$ (L mol <sup>-1</sup> )	$K_q$ (L mol <sup>-1</sup> s <sup>-1</sup> )	Correlation coefficient
292	$7.36 \times 10^4$	$7.36 \times 10^{12}$	0.9978
297	$5.27 \times 10^4$	$5.27 \times 10^{12}$	0.9921
302	$4.64 \times 10^4$	$4.64 \times 10^{12}$	0.9960

quenching. In order to clarify the quenching mechanism of TRES on BSA, the Stern-Volmer equation (1) is used to analyze the fluorescence quenching data [12], where  $F_0$  and  $F$  are the fluorescence intensities in the absence and presence of quencher,  $K_q$  is the quenching rate constant of the biomolecule,  $\tau_0$  is the average lifetime of the biomolecule in the absence of quencher which equals  $10^{-8}$  s [13],  $K_{SV}$  is the Stern-Volmer quenching constant, and  $[Q]$  is the concentration of quencher. One has

$$\frac{F_0}{F} = 1 + K_q \tau_0 [Q] = 1 + K_{sv} [Q]. \quad (1)$$

Within certain concentration, the curve of  $F_0/F$  versus  $[Q]$  would be linear if the quenching type is single static or dynamic process. The Stern-Volmer curves of TRES with BSA at three different temperatures exhibit good linear relationship within the investigated concentrations, so the values of  $K_q$  and  $K_{SV}$  can be determined from the slope of regression curve of  $F_0/F$  versus  $[Q]$ , and the results are listed in Table 1. For dynamic quenching, the maximum scatter collision quenching constant of various quenchers with the biopolymers is  $2.0 \times 10^{10}$  L mol<sup>-1</sup> s<sup>-1</sup>. In addition, dynamic and static quenching can be distinguished by temperature dependence of the quenching, the values of  $K_{SV}$  decrease with an increasing temperature for static quenching and the reverse result for dynamic quenching. From Table 1, the results show that the values of  $K_{SV}$  and  $K_q$  decrease with the increasing of temperature and the values of  $K_q$  is much greater than  $2.0 \times 10^{10}$  L mol<sup>-1</sup> s<sup>-1</sup>, which indicates that the probable quenching mechanism of BSA-TRES interaction is initiated by static quenching rather than by dynamic collision [14, 15]. The results are also confirmed by UV-vis experiments as shown in Figure 3. Figure 3 illustrates that the UV-vis absorption spectrum of BSA and the difference absorption spectrum between BSA-TRES and TRES at the same concentration could not be superposed. After interaction with TRES, the absorbance band intensity of BSA at 280 nm decreases and the peak position shows a slight blue shift, suggesting the formation of BSA-TRES complex.

**3.2. The Binding Constant and Number of Binding Sites.** When small molecules bind independently to a set of equivalent sites on a macromolecule, the binding constant ( $K_b$ ) and the number of binding sites ( $n$ ) can be obtained from fluorescence intensity data by [16]

$$\log \left[ \frac{(F_0 - F)}{F} \right] = \log K_b + n \log [Q]. \quad (2)$$

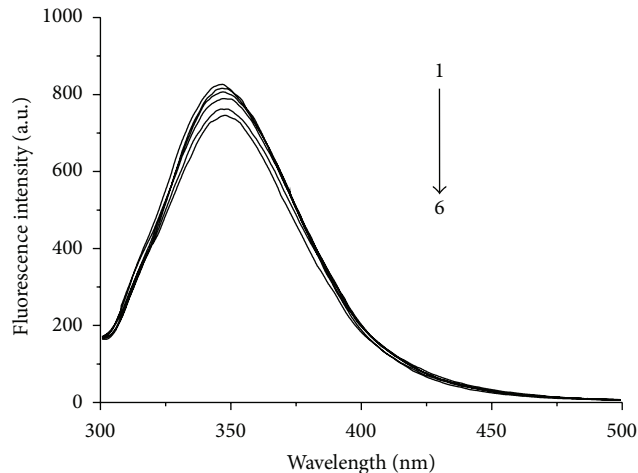


FIGURE 2: Fluorescence quenching spectra of BSA in presence of different concentrations of TRES.  $C_{BSA} = 3.0 \times 10^{-7}$  mol L<sup>-1</sup>;  $C_{TRES}$  ( $\times 10^{-7}$  mol L<sup>-1</sup>) (1-6): 0, 3, 6, 12, 18, and 24, respectively;  $\lambda_{ex} = 280$  nm;  $T = 302$  K.

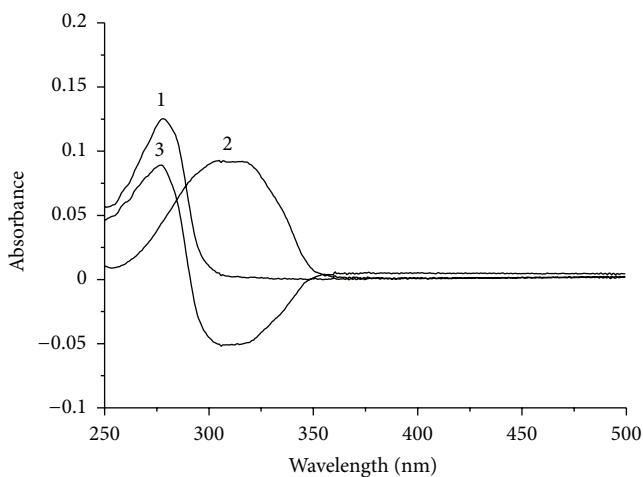


FIGURE 3: UV-vis absorption spectra of BSA (1), TRES (2), and the difference spectrum between TRES-BSA and TRES (3).  $C_{BSA} = C_{TRES} = 3.0 \times 10^{-5}$  mol L<sup>-1</sup>; pH = 7.4.

Based on (2), the values of  $n$  and  $K_b$  can be determined from the slope and intercept of the double logarithm regression curve ( $\log [(F_0 - F)/F]$  versus  $\log [Q]$ ), and the corresponding calculated results are listed in Table 2. It is found that the values of  $K_b$  decrease with the increasing of temperature, indicating that the stability of BSA-TRES complex reduces with the temperature rising. The values of  $n$  approximately equal unity, indicating that there is one independent class of binding sites in BSA for TRES.

**3.3. Thermodynamic Analysis and Binding Mode.** Thermodynamic parameters relying on temperatures are analyzed to characterize the acting forces between TRES and BSA. Generally speaking, the binding forces between drugs and biomolecules mainly include electrostatic interaction, hydrogen bond, van der Waals interaction, and hydrophobic

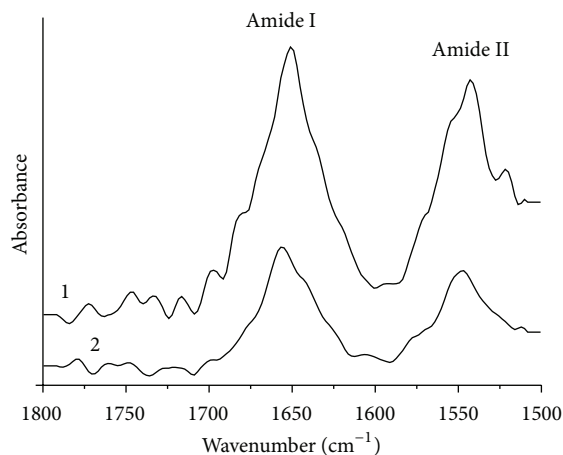


FIGURE 4: FTIR difference spectra of BSA in Tris-HCl buffer solution. (1) free BSA ( $C_{\text{BSA}} = 1.0 \times 10^{-4} \text{ mol L}^{-1}$ ); (2) bonded BSA ( $C_{\text{BSA}} = 1.0 \times 10^{-4} \text{ mol L}^{-1}$ ,  $C_{\text{TRES}} = 2.0 \times 10^{-4} \text{ mol L}^{-1}$ ). pH = 7.4.

interaction [17]. Thermodynamic parameters, free energy change ( $\Delta G$ ), enthalpy change ( $\Delta H$ ), and entropy change ( $\Delta S$ ) of interaction, are essential to interpret the binding mode of BSA-drugs complexes. When enthalpy change ( $\Delta H$ ) does not vary significantly in the temperature range studied, both enthalpy change ( $\Delta H$ ) and entropy change ( $\Delta S$ ) can be determined from van't Hoff equation (3). In (3),  $K$  corresponds to the binding constant at specific temperature and  $R$  is the gas constant.  $\Delta H$  and  $\Delta S$  can be calculated from the slope and intercept of the regression curve of  $\ln K$  versus  $1/T$ .  $\Delta G$  is consequently obtained according to (4). One has

$$\ln K = \frac{-\Delta H}{RT} + \frac{\Delta S}{R}, \quad (3)$$

$$\Delta G = \Delta H - T\Delta S. \quad (4)$$

The Values of  $\Delta H$ ,  $\Delta S$ , and  $\Delta G$  for the interaction of TRES with BSA are presented in Table 2. The negative value of  $\Delta G$  indicates the binding process is spontaneous. Positive value of  $\Delta S$  is evidence of hydrophobic interactions [18]. In addition, specific electrostatic interaction between ionic species in aqueous solution is also characterized by a positive  $\Delta S$  and a negative  $\Delta H$ . Generally,  $\Delta G$  mainly comes from the large contribution of  $\Delta S$  with little contribution from  $\Delta H$  for electrostatic interaction [19]. However, in this work,  $\Delta G$  mainly comes from the contribution of  $\Delta H$ . Therefore, we infer that hydrophobic interaction might play a major role in the interaction of TRES with BSA, and electrostatic force may also be involved in the binding process. Meanwhile, hydrogen bond can not be excluded as TRES is a polyphenolic compound.

**3.4. Identification of Binding Site.** Similar to HSA, the globular protein BSA consists of three distinct drug-binding sites [20]. Sudlow et al. have suggested that site I of serum albumin shows affinity for warfarin, phenylbutazone, and so forth and site II for ibuprofen, flufenamic acid, and so forth [21]. Later studies indicated that digitoxin binding is independent

TABLE 2: Binding constants and thermodynamic parameters of BSA-TRES interaction at different temperatures.

$T/K$	$K_b$ ( $\text{L mol}^{-1}$ )	$n$	$\Delta H$ ( $\text{kJ mol}^{-1}$ )	$\Delta S$ ( $\text{J mol}^{-1} \text{K}^{-1}$ )	$\Delta G$ ( $\text{kJ mol}^{-1}$ )
292	$10.22 \times 10^4$	1.03			-28.00
297	$8.71 \times 10^4$	1.03	-21.82	21.15	-28.10
302	$7.59 \times 10^4$	1.04			-28.21

TABLE 3: Binding constants of competitive experiments ( $T = 302 \text{ K}$ ,  $\lambda_{\text{ex}} = 280 \text{ nm}$ ).

Site marker	$K_b$ ( $\text{L mol}^{-1}$ )	$R$	$n$
Blank	$7.59 \times 10^4$	0.9973	1.03
phenylbutazone	$6.17 \times 10^4$	0.9860	1.01
flufenamic acid	$1.17 \times 10^4$	0.9794	0.85
digitoxin	$6.11 \times 10^4$	0.9899	0.98

of sites I and II and binds to site III [22]. To identify the binding site of TRES on BSA, competition experiments were carried out with phenylbutazone, flufenamic acid, and digitoxin as site probes for site I, II, and III, respectively [23, 24]. According to (2), the experiment data are analyzed and the binding constants of BSA-TRES system in the presence of different site markers are calculated in Table 3. Obviously, flufenamic acid could significantly influence the binding of TRES with BSA, whereas phenylbutazone or digitoxin has a lesser effect on the binding of TRES to BSA. Hence, it can be concluded that TRES is mainly bound to site II (subdomain IIIA) of BSA.

**3.5. Conformation Investigation.** To verify whether the conformation of BSA had changed or not in the absence and presence of TRES, FTIR measurements were performed. FTIR spectra of proteins exhibit a number of amide bands due to different vibrations of the peptide moiety. The amide I peak position occurs in the region  $1600\text{--}1700 \text{ cm}^{-1}$  (mainly C=O stretch) and amide II band in the region  $1500\text{--}1600 \text{ cm}^{-1}$  (C-N stretch coupled with N-H bending mode). They both have a relationship with the secondary structure of proteins, and amide I band is more sensitive to the change of proteins secondary structure than amide II [25]. The FTIR difference spectra of free BSA and bonded BSA (after binding with TRES) are shown in Figure 4. It is noticed that the peak position of amide I moves from  $1651$  to  $1655 \text{ cm}^{-1}$ , and that of amide II shifts from  $1541$  to  $1545 \text{ cm}^{-1}$  in the FTIR spectrum of BSA after addition of TRES. From the shift in peaks position we can confirm that the conformation of BSA has been affected by the addition of TRES.

According to the literature [26, 27], The spectral ranges  $1610\text{--}1640 \text{ cm}^{-1}$ ,  $1640\text{--}1650 \text{ cm}^{-1}$ ,  $1650\text{--}1659 \text{ cm}^{-1}$ , and  $1660\text{--}1700 \text{ cm}^{-1}$  in the amide I are assigned generally to  $\beta$ -sheet, random coil,  $\alpha$ -helical, and  $\beta$ -turn structure, respectively. To analyze quantitatively the protein secondary structure, the infrared self-deconvolution and second derivative resolution enhancement were applied to estimate the number, position,

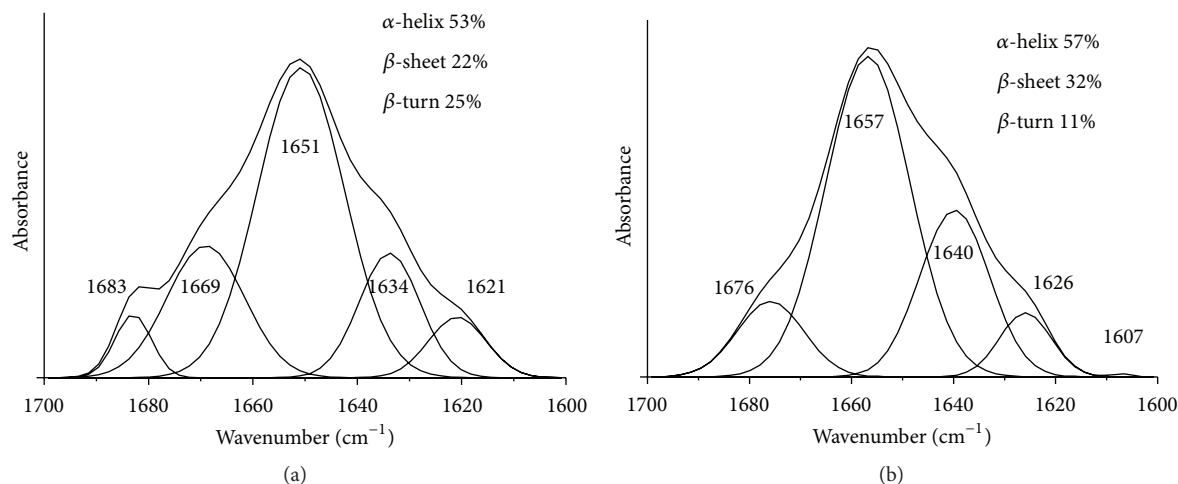


FIGURE 5: Curve-fitted amide I region for FTIR difference spectra of BSA. (a) Free BSA ( $C_{\text{BSA}} = 1.0 \times 10^{-4} \text{ mol L}^{-1}$ ); (b) bonded BSA ( $C_{\text{BSA}} = 1.0 \times 10^{-4} \text{ mol L}^{-1}$ ,  $C_{\text{TRES}} = 2.0 \times 10^{-4} \text{ mol L}^{-1}$ ). pH = 7.4.

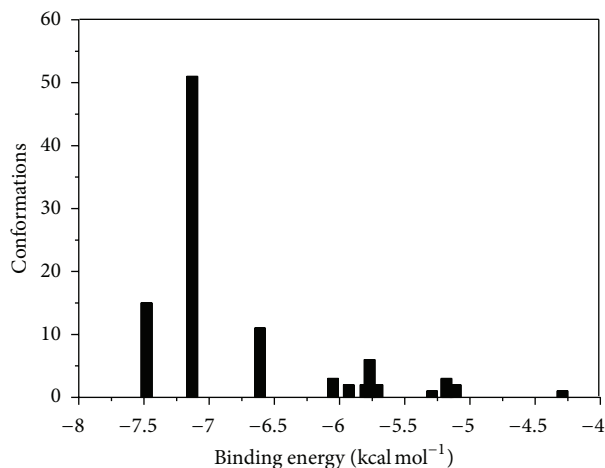


FIGURE 6: The clustering histogram at site II (RMSD: 2.0 Å).

and width of component bands in the region of 1700–1600 cm; then curve fitting procedures were used to get the best Gaussian-shaped curves that fit the original protein spectrum. The percentage of each secondary structure of BSA can be calculated based on the integrated areas of the component bands in amide I, and the results are shown in Figure 5. The results show that before and after the interaction with TRES, the protein major secondary structures had changed,  $\alpha$ -helical structure increased from 53% to 57%,  $\beta$ -sheet increased from 22% to 32%, and  $\beta$ -turn structures decreased from 25% to 11%, respectively.

**3.6. Molecular Modeling Study.** The fluorescence, UV-vis, and FTIR spectroscopic results were complemented with molecular modeling in which TRES was docked to BSA to determine the preferred binding site and the binding mode [28, 29]. In the initial exploration, the results predict that compared with site I and III, the TRES was mostly concentrated in site II with lower binding energy, so site II was selected as the probable



FIGURE 7: Best conformation for TRES docked to BSA. BSA is represented using cartoon ribbons and TRES is represented using ball.

binding region. Then the further exploration was carried out with a smaller grid map of  $86 \times 82 \times 72$  points centered at 39.148, 20.061, and 53.329 with a spacing of 0.375 Å at site II. The clustering histogram of further exploration at site II is shown in Figure 6. From Figure 6 we can see that the most populated cluster with 51 conformations has the second lower binding energy, so the lowest binding energy conformation of this cluster is selected and analyzed as the best binding mode. The best energy ranked results of the binding mode between TRES and BAS are shown in Figures 7 and 8. From Figure 7, it can be seen that TRES is located within the binding pocket of subdomain IIIA (site II, the flufenamic acid binding pocket) of the protein and the two rings are not coplanar. In Figure 8, TRES molecule is surrounded by 27 amino acid residues within 6 Å: 14 hydrophobic residues (Leu-387, Leu-407, Leu-453, Leu-430, Leu-457, Ile-388, Phe-403, Phe-488, Gly-431, Gly-434, Val-433, Pro-486, Ala-449,

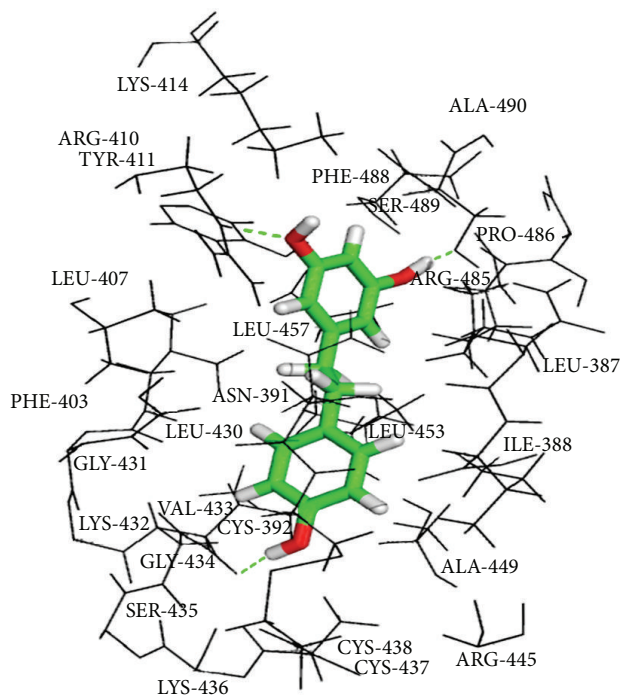


FIGURE 8: The amino acid residues around TRES within 6 Å. The residues of BAS are represented using line, TRES structure is represented using stick, and the hydrogen bonds are represented using green dashed line.

Ala-490), 7 hydrophilic residues (Asn-391, Cys-392, Cys-437, Cys-438, Tyr-411, Ser-435, Ser-489), and 6 ionic residues (Arg-410, Arg-445, Arg-485, Lys-414, Lys-432, Lys-436). It is important to note that the ring of TRES is adjacent to more hydrophobic residues, so hydrophobic forces may play major role in the binding. Furthermore there are three hydrogen bonds between the hydroxyl groups of TRES and the amino acid residues of BSA; they are 3-OH and Ser-489 with a bond length of 2.0 Å, 5-OH and Arg-410 with a bond length of 2.2 Å, and 4'-OH and Val-433 with a bond length of 2.0 Å. The formation of hydrogen bonds decreases the hydrophilicity and increases the hydrophobicity to stabilize the BSA-TRES system. In addition, electrostatic interactions may play a subordinate role in stabilizing the drug molecule due to the presence of the ionic and polar residues proximity to TRES. Therefore, it can be concluded that the interaction between TRES and BSA is dominated by hydrophobic forces, and there are also hydrogen bonds and electrostatic interactions, which is in good agreement with the results of binding mode study. The calculated binding Gibbs free energy change is  $-29.95 \text{ kJ mol}^{-1}$  (298 K), which is close to the experimental value ( $-28.10 \text{ kJ mol}^{-1}$ , 297 K) to a certain degree.

#### 4. Conclusions

Interaction mechanism of TRES with BSA has been investigated by fluorescence spectroscopic, UV-vis spectroscopic, FTIR spectroscopic methods and molecular modeling techniques. The results show that TRES interacts with BSA

through a combination of static quenching. The interaction is a spontaneous process and is driven by enthalpy and entropy together. The main interaction forces are hydrophobic forces accompanied by hydrogen bonds and electrostatic interactions. The secondary structure of BSA is changed after bonding with TRES. TRES can bind to BSA at site II in subdomain IIIA according to displacement experiments and molecular modeling.

#### Conflict of Interests

The authors declare that they have no conflict of interests with each other, and they also have no conflict of interests with Huamei Bioengineering Company, Xi'an Sino-Herb Biotechnology Company, ChemSkcteh, or GAMESS software.

#### Acknowledgments

The authors gratefully acknowledge the financial support of this study by the National Natural Science Foundation of China (Grant no. 20975081) and the special fund for basic scientific research of central colleges, Chang'an University (CHD2012JC093).

#### References

- [1] V. M. Rosenoer, M. Oratz, and M. A. Rothschild, *Albumin: Structure, Function, and Uses*, Pergamon Press, Oxford, UK, 1977.
- [2] X. Guo, X. Han, J. Tong et al., "The investigation of the interaction between piracetam and bovine serum albumin by spectroscopic methods," *Journal of Molecular Structure*, vol. 966, no. 1–3, pp. 129–135, 2010.
- [3] H. Larsericdotter, S. Oscarsson, and J. Buijs, "Structure, stability, and orientation of BSA adsorbed to silica," *Journal of Colloid and Interface Science*, vol. 289, no. 1, pp. 26–35, 2005.
- [4] M. Okawara, H. Katsuki, E. Kurimoto, H. Shibata, T. Kume, and A. Akaike, "Resveratrol protects dopaminergic neurons in midbrain slice culture from multiple insults," *Biochemical Pharmacology*, vol. 73, no. 4, pp. 550–560, 2007.
- [5] S. Pervaiz and A. L. Holme, "Resveratrol: its biologic targets and functional activity," *Antioxidants and Redox Signaling*, vol. 11, no. 11, pp. 2851–2897, 2009.
- [6] F. Z. Marques, M. A. Markus, and B. J. Morris, "Resveratrol: cellular actions of a potent natural chemical that confers a diversity of health benefits," *The International Journal of Biochemistry & Cell Biology*, vol. 41, no. 11, pp. 2125–2128, 2009.
- [7] L. Rivera, R. Morón, A. Zarzuelo, and M. Galisteo, "Long-term resveratrol administration reduces metabolic disturbances and lowers blood pressure in obese Zucker rats," *Biochemical Pharmacology*, vol. 77, no. 6, pp. 1053–1063, 2009.
- [8] B. Burstein, A. Maguy, R. Clément et al., "Effects of resveratrol (*trans*-3,5,4'-trihydroxystilbene) treatment on cardiac remodeling following myocardial infarction," *Journal of Pharmacology and Experimental Therapeutics*, vol. 323, no. 3, pp. 916–923, 2007.
- [9] X. Li, H. Li, M. Liu, G. Li, L. Li, and D. Sun, "From guest to ligand—a study on the competing interactions of antitumor drug resveratrol with  $\beta$ -cyclodextrin and bovine serum albumin," *Thermochimica Acta*, vol. 521, no. 1-2, pp. 74–79, 2011.

- [10] X. L. Wei, J. B. Xiao, Y. F. Wang, and Y. L. Bai, "Which model based on fluorescence quenching is suitable to study the interaction between *trans*-resveratrol and BSA?" *Spectrochimica Acta Part A*, vol. 75, pp. 299–304, 2010.
- [11] S. Cao, D. Wang, X. Tan, and J. Chen, "Interaction between *trans*-resveratrol and serum albumin in aqueous solution," *Journal of Solution Chemistry*, vol. 38, no. 9, pp. 1193–1202, 2009.
- [12] J. R. Lakowicz, *Principles of Fluorescence Spectroscopy*, Plenum, New York, NY, USA, 2nd edition, 1999.
- [13] T. G. Dewey, *Biophysical and Biochemical Aspects of Fluorescence Spectroscopy*, Plenum Press, New York, NY, USA, 1991.
- [14] S. M. T. Shaikh, J. Seetharamappa, P. B. Kandagal, and D. H. Manjunatha, "In vitro study on the binding of anti-coagulant vitamin to bovine serum albumin and the influence of toxic ions and common ions on binding," *International Journal of Biological Macromolecules*, vol. 41, no. 1, pp. 81–86, 2007.
- [15] B. H. M. Hussein, "Spectroscopic studies of 7, 8-dihydroxy-4-methylcoumarin and its interaction with bovine serum albumin," *Journal of Luminescence*, vol. 131, no. 5, pp. 900–908, 2011.
- [16] A. Belatik, S. Hotchandani, J. Bariyanga, and H. A. Tajmir-Riahi, "Binding sites of retinol and retinoic acid with serum albumins," *European Journal of Medicinal Chemistry*, vol. 48, pp. 114–123, 2012.
- [17] P. Bourassa, I. Hasni, and H. A. Tajmir-Riahi, "Folic acid complexes with human and bovine serum albumins," *Food Chemistry*, vol. 129, no. 3, pp. 1148–1155, 2011.
- [18] D. Leckband, "Measuring the forces that control protein interactions," *Annual Review of Biophysics and Biomolecular Structure*, vol. 29, pp. 1–26, 2000.
- [19] P. D. Ross and S. Subramanian, "Thermodynamics of protein association reactions: forces contributing to stability," *Biochemistry*, vol. 20, no. 11, pp. 3096–3102, 1981.
- [20] T. Kosa, T. Maruyama, and M. Otagiri, "Species differences of serum albumins: I. Drug binding sites," *Pharmaceutical Research*, vol. 14, no. 11, pp. 1607–1612, 1997.
- [21] G. Sudlow, D. J. Birkett, and D. N. Wade, "Further characterization of specific drug binding sites on human serum albumin," *Molecular Pharmacology*, vol. 12, no. 6, pp. 1052–1061, 1976.
- [22] I. Sjöholm, B. Ekman, A. Kober, I. L. Pahlman, B. Seiving, and T. Sjödin, "Binding of drugs to human serum albumin: XI. The specificity of three binding sites as studied with albumin immobilized in microparticles," *Molecular Pharmacology*, vol. 16, no. 3, pp. 767–777, 1979.
- [23] Q. L. Zhang, Y. N. Ni, and S. Kokot, "Molecular spectroscopic studies on the interaction between Ractopamine and bovine serum albumin," *Journal of Pharmaceutical and Biomedical Analysis*, vol. 52, no. 2, pp. 280–288, 2010.
- [24] J. Tian, J. Liu, X. Tian, Z. Hu, and X. Chen, "Study of the interaction of kaempferol with bovine serum albumin," *Journal of Molecular Structure*, vol. 691, no. 1–3, pp. 197–202, 2004.
- [25] J. W. Brauner, C. R. Flach, and R. Mendelsohn, "A quantitative reconstruction of the amide I contour in the IR spectra of globular proteins: from structure to spectrum," *Journal of the American Chemical Society*, vol. 127, no. 1, pp. 100–109, 2005.
- [26] P. Bourassa, S. Dubeau, G. M. Maharvi, A. H. Fauq, T. J. Thomas, and H. A. Tajmir-Riahi, "Locating the binding sites of anticancer tamoxifen and its metabolites 4-hydroxytamoxifen and endoxifen on bovine serum albumin," *European Journal of Medicinal Chemistry*, vol. 46, no. 9, pp. 4344–4353, 2011.
- [27] D. Roy, S. Dutta, S. S. Maity et al., "Spectroscopic and docking studies of the binding of two stereoisomeric antioxidant catechins to serum albumins," *Journal of Luminescence*, vol. 132, no. 6, pp. 1364–1375, 2012.
- [28] W. H. Gao, N. Li, Y. W. Chen et al., "Study of interaction between syringin and human serum albumin by multi-spectroscopic method and atomic force microscopy," *Journal of Molecular Structure*, vol. 983, no. 1–3, pp. 133–140, 2010.
- [29] K. Paal, A. Shkarupin, and L. Beckford, "Paclitaxel binding to human serum albumin—automated docking studies," *Bioorganic and Medicinal Chemistry*, vol. 15, no. 3, pp. 1323–1329, 2007.

## Research Article

# The Uptake Mechanism of the Cell-Penetrating pVEC Peptide

Ihsan Omur Akdag and Elif Ozkirimli

*Chemical Engineering Department, Bogazici University, Bebek, 34342 Istanbul, Turkey*

Correspondence should be addressed to Elif Ozkirimli; elif.ozkirimli@boun.edu.tr

Received 17 December 2012; Revised 8 March 2013; Accepted 10 March 2013

Academic Editor: Yifat Miller

Copyright © 2013 I. O. Akdag and E. Ozkirimli. This is an open access article distributed under the Creative Commons Attribution License, which permits unrestricted use, distribution, and reproduction in any medium, provided the original work is properly cited.

Peptide based drug design efforts have gained renewed interest with the discovery of cargo-carrying or cell-penetrating peptides. Understanding the translocation mechanism of these peptides and identifying the residues or elements that contribute to uptake can provide valuable clues toward the design of novel peptides. To this end, we have performed steered molecular dynamics (SMD) simulations on the pVEC peptide from murine vascular endothelial-cadherin protein and its two variants. Translocation was found to occur in three stages, adsorption via the cationic residues, inclusion of the whole peptide inside the membrane accompanied by formation of a water defect, and exit of both peptide and water molecules from the bilayer. Our simulation results suggest that the precise order in which the hydrophobic, cationic, and the polar regions are located in the amphipathic pVEC peptide contributes to its uptake mechanism. These results present new opportunities for the design of novel cell-penetrating and antimicrobial peptides.

## 1. Introduction

An ideal drug is only effective insofar as its ability to reach its target. Peptide drugs, with their high specificity and affinity to their targets, have emerged as promising drug leads [1, 2]. However, most peptides, as well as proteins and oligonucleotides, are mainly hydrophilic, hindering their cellular uptake and, hence, limiting their widespread use as therapeutics [3, 4]. Delivery of these compounds into the cell is an intense area of research, and microinjection [5], electroporation [6], liposomes [7], endocytosis [8], and viral vectors have been previously proposed as potential delivery methods [9]. However, these delivery methods are not efficient, and accordingly most of the peptides in the market target extracellular enzymes or receptors. The discovery of cargo-carrying or cell-penetrating peptides (CPPs) [10, 11] has spurred renewed interest in the use of peptide drugs against intracellular targets. These peptides are able to penetrate the cell membrane and carry cargo of different size and hydrophobicity into the cell. CPPs are cationic and amphipathic peptides of usually fewer than 30 amino acids [12, 13]. They do not share an obvious common sequence or structural motif [12]. Although the translocation mechanism is not the same for different CPP families, there are two major cellular uptake mechanisms, which are direct penetration

(energy-independent) and endocytotic pathways [14]. In an energy- and receptor-independent mechanism, they penetrate cell membranes either via electrostatic interactions or hydrogen bonding [9, 15–17]. The spontaneous penetration of CPPs may be by the carpet model, through transient pores, through the formation of inverted micelles, local electroporation, and direct insertion of the unfolded peptide into the membrane [10, 12, 13]. The uptake mechanism at an atomic level of detail is not known, and some questions of significance for peptide design remain. Which residues or structural elements contribute to uptake? Which interactions allow and/or facilitate transport of the peptide? Here, we examine the membrane translocation mechanism of one such peptide, pVEC, using steered molecular dynamics (SMD) simulations.

pVEC, an 18-amino-acid-long CPP, is derived from murine vascular endothelial-cadherin protein that functions in the physical contact between adjacent cells. With the sequence, LLILRRRIRKQAHASK, the N-terminus is hydrophobic, the middle part is charged, and the C-terminus is hydrophilic, making it an amphipathic molecule. Previous cargo-carrying experiments showed that pVEC was able to carry some proteins and oligomers [18]. pVEC was found to have a random coil structure in pure water and neutral phospholipids, but it forms a beta-sheet in the negatively

charged DOPG membrane [16]. Structure-activity relationship (SAR) experiments, in which each pVEC residue was mutated to L-alanine and the change in the cellular uptake of pVEC into human Bowes melanoma cells was examined, were performed in order to identify the contribution of each residue to uptake [18]. Substitution of the five N-terminal residues to L-alanine was shown to drop cellular uptake by 50% to 75% suggesting that the hydrophobic N-terminus of the peptide is important for cellular uptake. Furthermore, deletion of the three N-terminal hydrophobic residues completely abolished uptake, and when all five hydrophobic residues (LLIIL) were replaced by L-alanines in the N-terminus, the uptake of peptide was not detected at all.

The behavior of peptides in or near lipid bilayer environments has been previously investigated using molecular dynamics (MD) simulations. However, MD simulations are not sufficiently long to sample events, such as transport across the membrane, that take place on the microsecond or longer timescale, and nonequilibrium MD simulations provide an attractive alternative to obtain atomic level detail about such transitions. One of these nonequilibrium methods is steered molecular dynamics (SMD) [19–21], in which force is applied to one (or more) SMD atom to move the system from one state to another. This nonequilibrium method has been used with success in a variety of dynamic systems to study drug binding [22], transport across membrane proteins [23], and unfolding [24]. SMD simulations have also been used to examine peptide uptake through the lipid bilayer, as MD simulations on the cardiotoxin A3 peptide and POPC lipid bilayer system showed that the peptide would not spontaneously bind to the membrane [25]. SMD simulations showed that Tryptophan residue of the WL5, with the sequence WLLLLL, was found to contribute to peptide-membrane interactions, and penetration depth of the peptide into the membrane was found to be related to its hydrophobicity [26]. Similarly, the presence of hydrophobic tryptophan residues was found to result in deeper insertion of Indolicidin, an antimicrobial peptide, while positive charges were critical to the peptide’s adsorption [27].

Here, SMD simulations on wild type pVEC and its two variants were performed to move the peptide from one side of the bilayer to the other. The translocation mechanism was observed to occur in three distinct stages; the insertion of the N-terminus into the bilayer, the inclusion of the whole peptide inside the membrane, and the exit of the peptide from the bilayer. The presence of barriers at these stages was verified by the presence of plateaus followed by abrupt changes in the interaction energy profiles as well as sudden increases in force applied to the SMD atom. The structural elements that contribute to peptide—membrane association and subsequent uptake were identified.

## 2. Methods

**2.1. Simulation Systems.** The initial coordinates of the pVEC peptide were assigned as a beta-hairpin starting from the coordinates of a beta-hairpin loop of a beta-lactamase inhibitor protein using the psfgen module of visual molecular

TABLE 1: The pVEC sequences used in the simulations and the mutated residue for each sequence.

Name	Sequence
pVEC	LLIILRRRIRKQAHAAHSK
Retro-pVEC	KSHAAHQKRIRRRLLILL
Scramble-pVEC	IAARIKLRSRQHILRHL

dynamics (VMD) [28]. Using the modeled pVEC coordinates as a template, the sequence was altered to obtain the retro-pVEC and scramble-pVEC coordinates. The peptide pVEC (wild-type), retro-pVEC, which has the same sequence in reverse order, and scramble-pVEC, which has the same amino acid content in random order [29], were studied (Table 1).

**2.2. Equilibration of Peptide in Water Environment.** The pVEC peptide (or its variants) was solvated with the solvate module in VMD using 10 Å padding in each direction resulting in a water box size of 43 Å × 48 Å × 52 Å. Water molecules closer than 2.8 Å to the peptide were removed. The water-peptide system was minimized for 1000 steps and equilibrated for 2 ns with harmonic constraints ( $k = 1 \text{ kcal/mol/Å}^2$ ) on peptide atoms. Then, all atoms of the system were allowed to equilibrate for 2 ns without constraints.

**2.3. Preparation of Lipid-Water-Peptide System.** The membrane was created in 50 Å in  $x$ - and 50 Å in  $y$ -directions. The membrane lipid was chosen to be POPE in order to mimic the membrane of *E. coli* [30]. The membrane was solvated with TIP3P water molecules 80 Å in positive and negative  $z$ -directions. After solvation, the water-membrane system was equilibrated for 0.5 ns with harmonic constraints ( $k = 1 \text{ kcal/mol/Å}^2$ ) and for 0.5 ns without constraints. The previously equilibrated peptide was placed into the water layer above the membrane manually such that the minimum distance between the peptide atoms and the membrane phosphate atoms was more than 10 Å. Water molecules closer than 2.8 Å to the peptide were removed. Counterions were added to a concentration of 0.4 M.

**2.4. Steered Molecular Dynamics Simulations.** Steered molecular dynamics simulations [22] were performed by applying force on the N-terminal  $C_\alpha$  atom (SMD atom) of the peptide in the  $z$ -direction to move the peptide across the membrane. For these simulations, the phosphorous heads of the lipid bilayer were harmonically constrained in the  $z$ -direction with a force constant of  $1 \text{ kcal/mol/Å}^2$ , while they were free to move in  $x$ - and  $y$ -directions allowing the formation of the pore through which the peptide and/or water entered the bilayer. The spring constant in the SMD simulations was  $10 \text{ kcal/mol/Å}^2$ , and the velocity of pulling was  $0.0000050 \text{ Å/timestep}$  which corresponds to  $2.50 \text{ Å/ns}$  with  $\text{timestep} = 2.0 \text{ fs}$ . The peptide traveled 120 Å to completely traverse the membrane within about 50 ns simulation time.

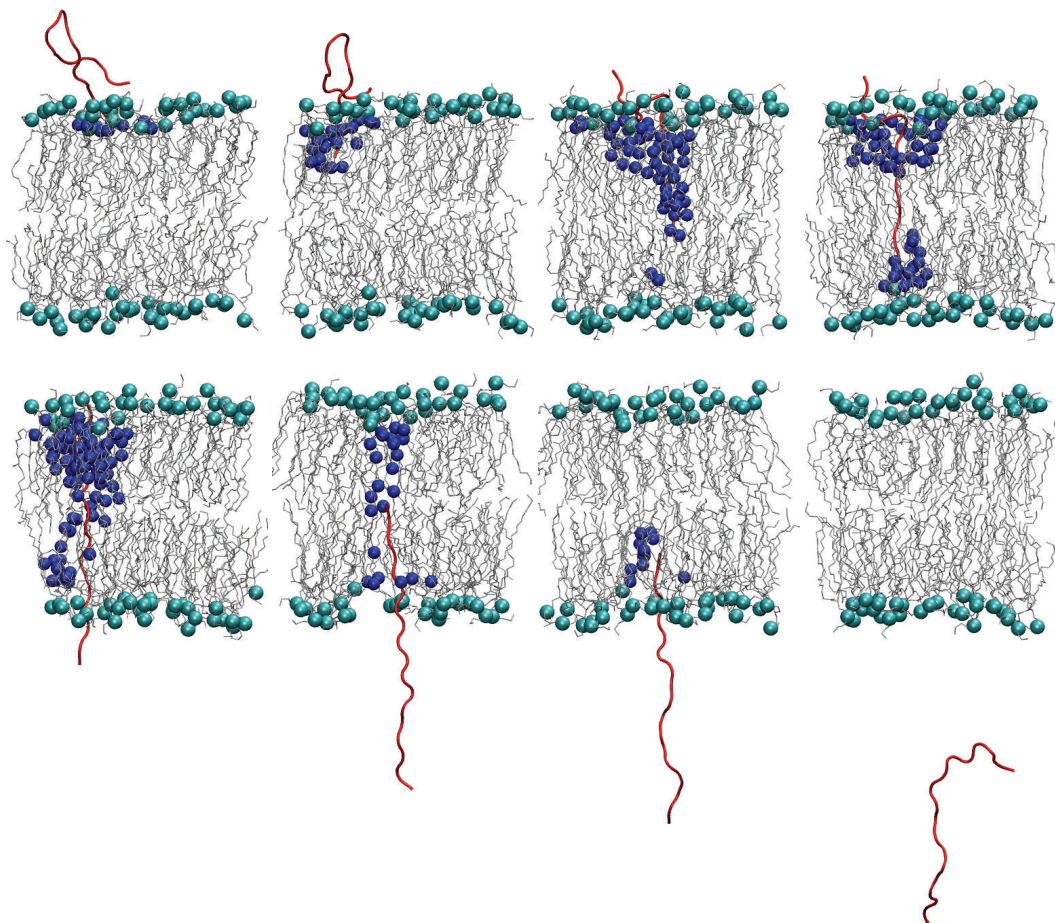


FIGURE 1: Snapshots for the SMD simulation on pVEC peptide as it moves across the bilayer. The peptide backbone is shown in red in cartoon representation, the phosphate heads are shown as cyan spheres, the lipid tails are shown in gray, and the water molecules are shown as blue spheres. Hydrogens in the lipids and water molecules are omitted for clarity.

TABLE 2: Summary of events in the SMD simulation on pVEC with SMD force applied on the N-terminal  $C_{\alpha}$  atom.

	$z$ (Å)	Peptide location	Interaction energy (kcal/mol)	Force (pN)	Number of waters in membrane
(i)	30	Before entry	0	0	0
(ii)	20	First contact with membrane	-300	-1000	0
(iii)	10	SMD atom through the P layer	-100	-1000	10
(iv)	0 to -20	Peptide moves through membrane, N-terminus reaches lower P layer	-500	-1000	20 to 5
(v)	-30 to -60	Peptide continues to move out	-300	-500	60 to 10

All simulations were calculated with the NAMD program [31] using the CHARMM27 potential energy function for the all atom model for proteins [32] and lipids [33] and TIP3P water parameters [34]. Periodic boundary conditions with particle mesh Ewald [35] method were used. Nonbonded interactions were truncated at a cutoff value of 12 Å and a switching distance of 10 Å. Nonbonded interactions were calculated at each step. SHAKE was applied on all hydrogen distances and a timestep of 2 fs was used. Constant pressure of 1 atm was imposed by the Langevin piston [36, 37] with a piston period of 200 fs. Langevin dynamics were used to keep

the system at constant temperature 300 K with a damping coefficient of 5/ps. The coordinate sets were saved every 2 ps for analysis. The SMD forces were output every 20 steps (40 fs).

**2.5. Trajectory Analysis.** Interaction energy between the peptide and the lipids was calculated using the NAMD Energy plugin of VMD. Force was calculated by NAMD at every SMD step. Work was calculated as the integral of force multiplied by pulling velocity over time. The number of water molecules within the membrane boundaries was monitored. Secondary

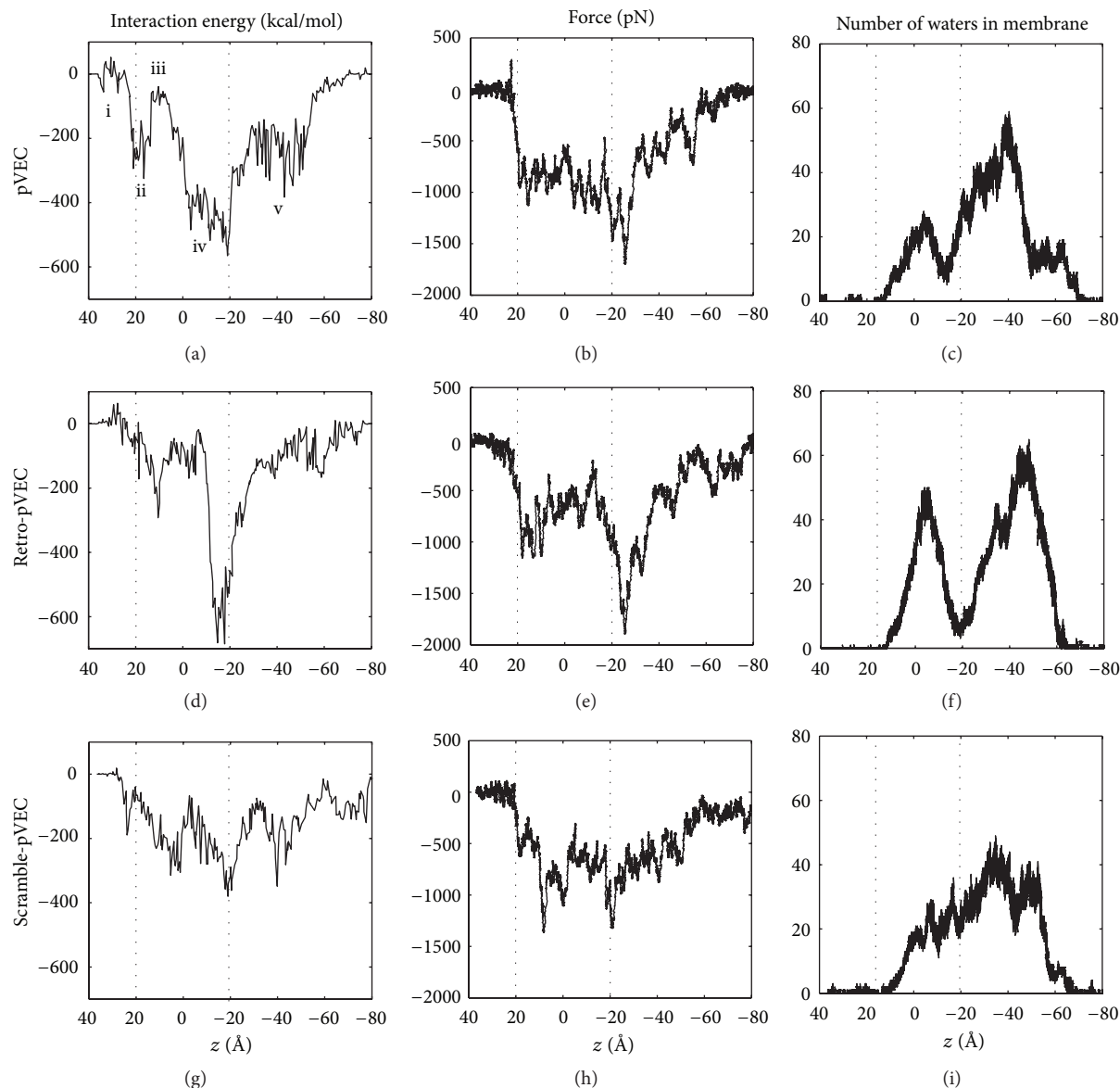


FIGURE 2: Interaction energy between the lipid and peptide atoms (left panel), force applied to the SMD atom (middle panel), and the number of water molecules in the membrane boundary (right panel) is shown as a function of the SMD atom  $z$ -coordinate for SMD simulations on the pVEC (top), retro-pVEC (middle), and scramble-pVEC (bottom) transport across the lipid bilayer. The membrane boundaries are indicated by the dashed lines at  $z = 20$  Å and  $-20$  Å. The regions in which the interaction energy between wild type pVEC and the membrane stays constant for more than 5 ns are indicated in panel (a).

structure of the peptide during the SMD simulations was monitored using the Timeline tool of VMD. Structure figures were prepared with VMD [28].

### 3. Results and Discussion

Steered molecular dynamics simulations on the wild-type pVEC, retro-pVEC, which has the pVEC sequence in reverse order, and scramble-pVEC, which has the same amino acid composition but a scrambled sequence (Table 1), were performed and analyzed to obtain atomic level information on

the translocation mechanism of pVEC. The retro-pVEC and scramble-pVEC were shown to have dramatically reduced uptake compared to pVEC as measured by the level of fluorescence in the cells after incubation with fluoresceinated peptide [29], and we aimed to elucidate the reasons for the drop in uptake values observed for these peptides using SMD simulations and comparing the results with those of pVEC simulations.

As a first step, SMD trajectories were analyzed visually to obtain information about the overall structural changes in peptide, membrane, or water. Some snapshots from the

TABLE 3: The maximum interaction energy, maximum force applied, and maximum work done values for the pVEC simulations.

Name	Maximum interaction energy (kcal/mol)	Maximum force applied in negative $z$ direction (pN)	Maximum work done (kcal/mol)
pVEC	-565	1653	916
Retro-pVEC	-685	1803	919
Scramble-pVEC	-380	1308	797

trajectory are shown in Figure 1. The first noteworthy change was in the peptide conformation. pVEC initial structure was assigned as a beta-hairpin. pVEC was reported to have a random coil structure in pure water and neutral phospholipids, and to form a beta-sheet in negatively charged DOPG membrane [16]. In the simulations, the SMD force was applied to the N-terminal  $C_{\alpha}$  atom to facilitate transport of the peptide in 50 ns, while the rest of the peptide was allowed to move freely and therefore could maintain its beta-sheet form. Examination of the change in secondary structure during the simulations (Supplementary Figure 2) showed that the peptide remained in the beta-sheet form until the SMD atom entered the bilayer, after which it gradually unfolded into a random coil and moved across the bilayer as a chain. Upon exit, the peptide started to become more compact, as shown by the decrease in the distance between the N- and C-terminal  $C_{\alpha}$  atoms (Supplementary Figure 2), even though the only force continued to be on the SMD atom. Our results suggest that the unfolding of the peptide, which is observed during peptide transport across the bilayer, is due to the interactions with membrane atoms, which were represented with an explicit model in this work. The second structural change was the formation of a water defect as the peptide travelled across the bilayer. Formation of the water defect may alter the membrane permeability, enhancing uptake. The mechanism by which the changes in the peptide and the membrane structure may contribute to uptake is examined in detail in the following sections.

**3.1. pVEC Travels across the Lipid Bilayer in Three Stages.** The uptake of the pVEC peptide across the POPE bilayer as the  $C_{\alpha}$  atom of the peptide N-terminal residue was pulled across the bilayer was monitored. The interaction energy between the peptide, and the lipid bilayer, the force applied to the peptide and the number of water molecules within the lipid bilayer were calculated and plotted as a function of the  $z$ -coordinate of the SMD atom (Figure 2).

The interaction energy profile for the wild-type pVEC simulation contains regions in which the energy stays constant for more than 5 ns (indicated as i through v in Figure 2(a)) followed by sudden increases or decreases. The “plateaus” in the interaction energy profile (Figure 2(a) and ii, iv, and v) may indicate regions of sustained interaction that must break for the transport to proceed, or, namely, energy barriers in the process. Similarly, the abrupt increases in the force profile observed at entrance and exit of SMD atom

into the bilayer (Figure 2(b);  $z \approx 20$  and  $-25$  Å) may point out the possible energy barriers that must be overcome by the application of increased force. These changes in energy and force suggest that pVEC transport occurs in three main stages, which are the adsorption of the peptide at the lipid-water interface ( $z \approx 20$  Å, ii), the inclusion of the whole peptide inside the membrane ( $z \approx 0$  to  $-20$  Å, iv), and the exit of the peptide N-terminus from the bilayer followed by exit of the whole peptide ( $z \approx -30$  to  $-60$  Å, v) with the main barriers to transport at the membrane-water boundaries on both sides. The steps are summarized in Table 2 and explained in some detail later.

Before contact with the bilayer ( $z \approx 30$  Å; Figure 2(a), i), the interaction energy, force, and number of waters in the membrane are all zero. When the peptide makes its first contact with the membrane, the interaction energy reaches its first maximum value at about  $-300$  kcal/mol as a result of the interaction of the positively charged residues and the positively charged amino terminus with the phosphate groups and the first barrier is observed (Figure 2(a) and ii). Even though the SMD force is applied to the N-terminal  $C_{\alpha}$  atom, the positively charged residues of the peptide midsection also make contact with the negatively charged phosphate layer. Once the N-terminus passes the P heads of the membrane ( $z \approx 10$  Å; Figure 2(a) and iii), the interaction energy decreases back to about  $-100$  kcal/mol and peptide insertion starts. Between  $z = 0$  and  $-20$  Å, the peptide moves through the bilayer (Figure 2(a) and iv). The second barrier is seen at this stage and the interaction energy reaches its overall maximum point at around  $-500$  kcal/mol. At  $z \approx -20$  Å, the N-terminus is in contact with the lower P heads while the C-terminus is in contact with the upper P heads. As the peptide moves out of the lipid bilayer ( $z \approx -30$  to  $-60$  Å; Figure 2(a) and v), interaction between the peptide and the membrane decreases back to about  $-300$  kcal/mol and oscillates around this value as the peptide tries to find its way out of the membrane. The interaction between the peptide and the membrane is maintained until the peptide completely leaves the membrane at  $z \approx -70$  Å and starts to become more compact (Supplementary Figure 2).

The electrostatic and van der Waals energies between the peptide and the membrane were also calculated to identify the contribution of each to the total interaction energy (Supplementary Figure 1). The electrostatic energy contribution to the interaction energy profile was found to be higher and the electrostatic energy profile resembles that of the total interaction energy, with maximum energy value attained when the peptide is completely immersed inside the membrane. At this point, the van der Waals energy also contributes 100 kcal/mol to total energy.

The SMD force applied to the wild-type pVEC in the negative  $z$ -direction during the simulations was calculated and plotted with respect to SMD atom  $z$ -coordinate (Figure 2(b)). At the beginning of the simulation, as the peptide moves through the water layer, the magnitude of the force applied is 0 pN. At  $z \approx 20$  Å, a sudden increase in the force is observed as the peptide contacts the membrane. The membrane resists penetration by the peptide, and to overcome this resistance, about 1000 pN of force is applied to the peptide as it moves

through the bilayer. The force value increases to  $-1500$  pN ( $z \approx -25$  Å) when the peptide is totally immersed in the membrane and the N-terminus starts to exit the membrane. After this checkpoint, the peptide starts to leave the membrane and a lower force of about  $-500$  pN is applied until the peptide is out of the membrane and moving through the water layer, at which point the magnitude of the force applied reduces back to  $0$  pN.

The number of water molecules that penetrate into the cell membrane was monitored (Figure 2(c)). At the beginning of the simulation, the peptide is embedded in the water layer above the membrane and the initial number of water molecules in the membrane is equal to zero until the peptide starts to penetrate into the membrane ( $z \approx 20$  Å). As peptide insertion starts, the cavity formed by the peptide is filled by about 20 water molecules causing the small peak observed at  $z \approx 0$  Å. As peptide insertion continues and the SMD atom approaches the lower layer of the membrane, some of the water molecules grouped around the first residues of the peptide leave the membrane and the number of water molecules drop ( $z \approx -13$  Å). When the SMD atom starts to leave the membrane, the C-terminal of the peptide is in contact with the upper layer of the membrane and the peptide is completely extended. As the peptide beta-hairpin structure unfolds and the peptide is immersed in the membrane, the number of water molecules in the membrane increases and reaches its maximum at around 70 at  $z \approx -40$  Å. The formation of the larger water defect is due to solvation of the cationic stretch (RRRIRK) in the midsection of pVEC. After this peak, a small shoulder is observed between  $z = -50$  and  $-70$  Å, and about 20 waters are retained in the membrane as the peptide continues its exit. The number of water molecules continues to decrease and finally becomes 0 when the last residue Lys18 leaves the membrane.

There is some debate in the literature about whether arginine residues can be present in their ionized states in hydrophobic environments such as membrane proteins [38], peptides [39], or even protein interiors [40]. It has recently been shown by Tieleman and coworkers, who used molecular dynamics simulations to decipher the partitioning of amino acids between the water and lipid phase, that Arg can remain ionized even in the middle of the membrane due to formation of a water defect around the residue [41]. Furthermore, it has been suggested that additional arginines may take advantage of the existing water defect in a "piggyback" mechanism [42, 43]. In the pVEC peptide, the cationic stretch of residues comprises a series of arginine residues. Mutation of these arginines to alanine (one at a time) has been shown to cause no drop in pVEC uptake potential [29]. However, the presence of the other arginines might be sufficient to form the initial contact, hence, promoting adsorption at the water-lipid interface, and then formation of the water defect, which may facilitate pore formation and transport.

### 3.2. The Peptide Sequence Governs the Uptake Mechanism.

In an effort to understand how the pVEC peptide sequence, specifically the N-terminal hydrophobic stretch and the positively charged region in the middle, contributes to the

uptake mechanism, the SMD simulations were repeated using retro-pVEC and scramble-pVEC. These two pVEC variants were shown to have lower uptake values as measured by accumulation of fluorescence [29]. The interaction energy, force, and number of water molecules in the membrane are shown in Figure 2 middle panel for retro-pVEC, and in Figure 2 bottom panel for scramble-pVEC and the maximum interaction energy values, the maximum force applied to the peptides, and the work values attained in the simulations are listed in Table 3 for each simulation.

The simulations on retro-pVEC were performed in order to compare how reversing the order in which residues enter the membrane would affect uptake. In the SMD simulation on pVEC, the SMD force is applied to the N-terminal  $C_\alpha$  atom, and therefore the hydrophobic stretch enters first, then the cationic stretch, and lastly the polar stretch of residues travel through the membrane. In retro-pVEC, this order is opposite because even though the SMD force is applied on the N-terminal  $C_\alpha$  atom again, the peptide sequence is in reverse order. It is not known which end moves across the bilayer first and comparison of the pVEC and retro-pVEC simulation results provide information about the consistently observed energy barriers for the two reaction coordinates. To further analyze entry at the polar C-terminus, the simulations on wild type pVEC were repeated by applying force on the C-terminal  $C_\alpha$  atom. The interaction energy, force, and number of waters were plotted as a function of the  $z$ -coordinate of the SMD atom in Supplementary Figure 3. Visual comparison of the trajectory as well as a comparison of the profiles for energy, force, and water defect size with the pVEC and retro-pVEC simulations showed that the three stages of the transition are also present in this simulation. A detailed comparison between the pVEC and retro-pVEC simulations, in both of which the SMD atom was the N-terminal  $C_\alpha$  atom, is given later.

In the retro-pVEC simulations, the interaction energy has one pronounced peak at  $z \approx -10$  Å and  $-650$  kcal/mol and two small plateaus at  $z \approx 10$  Å and  $-50$  Å and (Figure 2(d)). The initial drop in energy as well as two peaks (ii and v) observed in the pVEC simulations are missing in the retro-pVEC interaction energy profiles. The force profile also has a peak at  $z \approx -10$  Å and  $1750$  pN and two small plateaus at  $z = 20$  to  $-20$  Å and  $-40$  to  $-60$  Å, consistent with the interaction energy profile (Figure 2(e)). The maximum interaction energy and the maximum force applied are higher in retro-pVEC than in pVEC simulations (Table 3).

When the number of water molecules in the membrane is monitored during peptide transport in the pVEC simulation, three maxima ( $z \approx 0$ ,  $-40$ , and  $-60$  Å) are observed (Figure 2(c)). On the other hand, in the retro-pVEC simulation, the first maximum ( $z \approx 0$  Å) is much higher at 50 water molecules (Figure 2(f)). The number of water molecules decreases at  $z \approx -20$  Å and then increases again to 60 at  $z \approx -40$  Å. The initial abrupt increase observed in retro-pVEC is due to the uptake of water with the polar patch of residues that enters the membrane first, while in pVEC only the N-terminus is positively charged, resulting in the low maximum followed by the high peak due to entrance of the positively charged midsection.

It should be noted that three plateaus (albeit with different heights) are observed in the interaction energy profiles of pVEC and retro-pVEC simulations. Furthermore, the work values at the end of the simulations are similar at around 920 kcal/mol. The similarity in overall properties may be due to the presence of the same structural elements in both peptides, albeit in reverse order. The details of the interaction energy and force profiles as well as the formation of the water defect are different between pVEC and retro-pVEC simulations. In the pVEC simulation, the hydrophobic stretch is pulled through the membrane first, while in retro-pVEC simulations the polar patch is pulled through first. It has previously been suggested that hydrophobic groups contribute to deeper insertion of the peptide into the membrane [44]. Ile and Leu were shown by MacCallum et al. to be the most hydrophobic residues, preferring to be in the membrane bilayer rather than the interface [42]. Mutation of the LLIL residues in pVEC one by one to alanine results in a decrease in uptake potential, while deletion of the initial three residues or replacing the first five residues by L-alanine abolishes uptake [29]. These results suggest that the presence of the hydrophobic stretch composed of three Leu and two Ile residues, which are known to be highly hydrophobic, can contribute to penetration of pVEC into the bilayer. In our simulation results, when the hydrophobic stretch enters first in pVEC simulations, the interaction energy between the peptide and the membrane (Figure 2(a)) is lower than when the polar region enters first (Figure 2(d) and Supplementary Figure 3, left panel). The higher interaction energy between the polar stretch of residues and the membrane lower boundary may constitute a barrier to transition. Previous reports suggest that the hydrophobic stretch contributes to deeper penetration into the bilayer and facilitates transport. Furthermore, a large water defect that surrounds the C-terminal polar patch needs to form in the retro-pVEC simulations (and in C-terminus first pVEC simulations, Supplementary Figure 3), while the water defect is smaller and grows in size as the peptide enters and the arginine rich cationic midsection moves through the bilayer. Therefore, peptide entry at its hydrophobic N-terminus, which “guides” the peptide into the hydrophobic membrane, may be a more facile process.

pVEC has three distinct regions that can be classified as hydrophobic, cationic, and polar, while scramble-pVEC has a completely random order, possibly altering the amphipathic character of the peptide. As a result, the energy, force, and water defect size profiles lack distinguishable regions observed in the previous simulations. The interaction energy profile has several distributed maxima (Figure 2(g)), mirrored by the force profile (Figure 2(h)). The two maxima observed at  $z \approx 10 \text{ \AA}$  and  $-20 \text{ \AA}$  in the force profile are due to interaction of the positively charged residues with the phosphate groups in the two leaflets. The maximum interaction energy value reached is lower than the two other simulations at  $-380 \text{ kcal/mol}$ . The maximum force applied is also lower at 1300 pN. The flatter force profile as well as the low values of the maxima result in a low work value at 800 kcal/mol.

In scramble-pVEC simulations, about 40 water molecules enter the bilayer with the peptide, the number of water

molecules fluctuates between 20 and 40 with no pronounced peaks or troughs, and as the peptide leaves, the number drops gradually to 0 (Figure 2(i)). The absence of a well-defined structure in the number of water molecules that enter the membrane with the peptide is consistent with the relative absence of peaks in the interaction energy and force profiles.

## 4. Conclusions

In this study, steered molecular dynamics simulations on the pVEC peptide, retro-pVEC, and scramble-pVEC (Table 1) were performed in an effort to describe the mechanism whereby pVEC peptide is translocated across the cell membrane and to verify the significance of certain residues and structural elements in the translocation mechanism

Visual analysis of the trajectories showed that the peptide made its initial contact with the bilayer via its positively charged residues, and it unfolded from a beta-hairpin form to a random coil as it moved through the bilayer and that a water defect that surrounded the cationic or polar residues formed during peptide transport. The translocation mechanism was observed to occur in three main stages: (1) the insertion of the N-terminus into the bilayer, which is facilitated by the interaction of positively charged residues with the phosphate layer, (2) the inclusion of the peptide inside the membrane and formation of the water defect around the cationic stretch of residues, and (3) the exit of the peptide and water molecules from the bilayer.

The retro-pVEC uptake also has three stages represented as three maxima in the interaction energy profile, and similar amounts of work are applied in the pVEC and retro-pVEC simulations. The overall similarity in the two simulations correlate well with the presence of three distinct regions (hydrophobic-cationic-polar) in the two peptides. It is not known in which direction (N-terminus first or C-terminus first) the peptide enters the lipid bilayer. However, the stronger interactions as well as the formation of a larger water defect observed in retro-pVEC simulations (and in SMD simulations with force applied on the C-terminus of pVEC) may suggest that polar C-terminal entry, rather than the hydrophobic N-terminal entry, is a difficult mechanism. The hydrophobic residues, which would prefer to be in the membrane as suggested by MacCallum and coworkers [42], may “pull” the rest of the peptide along the bilayer. It is important to note that nonequilibrium MD simulations sample a reaction coordinate above the free energy landscape, and therefore a comparison of the energy, force, or work numerical values, especially for single trajectories, may not provide accurate information about the free energy landscape of the transition [21, 45]. Multiple simulations are required to obtain more accurate estimates of free energy [46–48]. However, the consistently observed features in the transition pathways may be helpful in identifying energy barriers. Our major contribution is the observation that the presence of three distinct regions in pVEC or retro-pVEC is related to the three distinct stages of the transition and that the water-membrane boundaries are the main barriers to transition.

On the other hand, the energy and force profiles of simulations on scramble-pVEC, which has no discernible sequence regions, do not have distinct peaks and are relatively more flat. The work that required to move the peptide across the membrane is also lower. This result would suggest relatively lower resistance to penetration; however, experiments have shown that this peptide has low uptake potential compared to pVEC [29]. It should be noted that, in pVEC and retro-pVEC simulations, an abrupt increase in force coincides with an increase in the interaction energy. Stronger interactions may create energy barriers that must be overcome, but the high interaction energy, especially between the cationic stretch and the top layer and later with the bottom layer, may also drive the peptide forward in the SMD direction. However, a continuously low force is applied in scramble-pVEC calculations, and no strong interactions form between the peptide and the membrane. Additionally, the water defect that forms is smaller in scramble-pVEC possibly due to the absence of an arginine rich cationic stretch of residues. There is no hydrophobic stretch of residues to move the peptide toward the membrane interior either. The absence of these two regions may cause the lower uptake observed for scramble-pVEC. We propose that it is either the residue composition nor the overall charge nor the overall hydrophobicity of the peptide but the presence of three distinct regions that contribute to the uptake of pVEC.

Our results provide evidence for unfolding of the peptide during direct penetration through bacterial membranes represented here by the explicit atoms of the POPE bilayer. The initial beta-hairpin form of the peptide is maintained in the water layer, but the peptide moves as a single chain during passage through the membrane. The membrane atoms act as a barrier in which the peptide and the surrounding water defect form a pore. Active participation of the membrane during uptake has been recognized [13], and our simulations also lend support to the use of explicit membrane models in the study of peptide transport.

## Abbreviations

MD: Molecular dynamics  
 SMD: Steered molecular dynamics  
 POPE, CPP: Cell-penetrating peptide.

## Acknowledgments

This work was supported by TUBITAK Research Grant 109M229 (E. Ozkirimli) and Bogazici University Research Grant 09HA504P (E. Ozkirimli). The authors thank Begum Alaybeyoglu for her help in figure preparation.

## References

[1] P. Vanhee, A. M. van der Sloot, E. Verschuere, L. Serrano, F. Rousseau, and J. Schymkowitz, "Computational design of peptide ligands," *Trends in Biotechnology*, vol. 29, no. 5, pp. 231–239, 2011.

- [2] E. O. Olmez and B. S. Akbulut, "Protein-peptide interactions revolutionize drug development," in *Binding Protein*, K. Abdelmohsen, Ed., chapter 3, InTech, 2012.
- [3] A. M. Gewirtz, D. L. Sokol, and M. Z. Ratajczak, "Nucleic acid therapeutics: state of the art and future prospects," *Blood*, vol. 92, no. 3, pp. 712–736, 1998.
- [4] R. L. Juliano, S. Alahari, H. Yoo, R. Kole, and M. Cho, "Antisense pharmacodynamics: critical issues in the transport and delivery of antisense oligonucleotides," *Pharmaceutical Research*, vol. 16, no. 4, pp. 494–502, 1999.
- [5] H. Arnheiter and O. Haller, "Antiviral state against influenza virus neutralized by microinjection of antibodies to interferon-induced Mx proteins," *EMBO Journal*, vol. 7, no. 5, pp. 1315–1320, 1988.
- [6] R. Chakrabarti, D. E. Wylie, and S. M. Schuster, "Transfer of monoclonal antibodies into mammalian cells by electroporation," *Journal of Biological Chemistry*, vol. 264, no. 26, pp. 15494–15500, 1989.
- [7] R. M. Straubinger, N. Duzgunes, and D. Papahadjopoulos, "pH-sensitive liposomes mediate cytoplasmic delivery of encapsulated macromolecules," *FEBS Letters*, vol. 179, no. 1, pp. 148–154, 1985.
- [8] C. M. Varga, T. J. Wickham, and D. A. Lauffenburger, "Receptor-mediated targeting of gene delivery vectors: insights from molecular mechanisms for improved vehicle design," *Biotechnology and Bioengineering*, vol. 70, no. 6, pp. 593–605, 2000.
- [9] B. Gupta, T. S. Levchenko, and V. P. Torchilin, "Intracellular delivery of large molecules and small particles by cell-penetrating proteins and peptides," *Advanced Drug Delivery Reviews*, vol. 57, no. 4, pp. 637–651, 2005.
- [10] M. Magzoub and A. Gräslund, "Cell-penetrating peptides: small from inception to application," *Quarterly Reviews of Biophysics*, vol. 37, no. 2, pp. 147–195, 2004.
- [11] F. Heitz, M. C. Morris, and G. Divita, "Twenty years of cell-penetrating peptides: from molecular mechanisms to therapeutics," *British Journal of Pharmacology*, vol. 157, no. 2, pp. 195–206, 2009.
- [12] S. Yesylevskyy, S.-J. Marrink, and A. E. Mark, "Alternative mechanisms for the interaction of the cell-penetrating peptides penetratin and the TAT peptide with lipid bilayers," *Biophysical Journal*, vol. 97, no. 1, pp. 40–49, 2009.
- [13] H. D. Herce and A. E. Garcia, "Molecular dynamics simulations suggest a mechanism for translocation of the HIV-1 TAT peptide across lipid membranes," *Proceedings of the National Academy of Sciences of the United States of America*, vol. 104, no. 52, pp. 20805–20810, 2007.
- [14] F. Madani, S. Lindberg, Ü. Langel, S. Futaki, and A. Graeslund, "Mechanisms of cellular uptake of cell-penetrating peptides," *Journal of Biophysics*, vol. 2011, Article ID 414729, 10 pages, 2011.
- [15] M. C. Morris, S. Deshayes, F. Heitz, and G. Divita, "Cell-penetrating peptides: from molecular mechanisms to therapeutics," *Biology of the Cell*, vol. 100, no. 4, pp. 201–217, 2008.
- [16] E. Eiríksdóttir, K. Konate, Ü. Langel, G. Divita, and S. Deshayes, "Secondary structure of cell-penetrating peptides controls membrane interaction and insertion," *Biochimica et Biophysica Acta*, vol. 1798, no. 6, pp. 1119–1128, 2010.
- [17] L. Liu, Y. Fang, Q. Huang, and J. Wu, "A rigidity-enhanced antimicrobial activity: a case for linear cationic  $\alpha$ -helical peptide HP(2-20) and its four analogues," *PLoS One*, vol. 6, no. 1, Article ID e16441, 2011.

- [18] A. Elmquist, M. Hansen, and Ü. Langel, "Structure-activity relationship study of the cell-penetrating peptide pVEC," *Biochimica et Biophysica Acta*, vol. 1758, no. 6, pp. 721–729, 2006.
- [19] S. S. Izrailev, S. Isralewitz B, D. Kosztin et al., "Steered molecular dynamics," in *Computational Molecular Dynamics: Challenges, Methods, Ideas*, P. H. Deuffhard, B. Leimkuhler, A. E. Mark, S. Reich, and R. D. Skeel, Eds., pp. 39–65, Springer, Berlin, Germany, 1998.
- [20] A. C. Lorenzo and P. M. Bisch, "Analyzing different parameters of steered molecular dynamics for small membrane interacting molecules," *Journal of Molecular Graphics and Modelling*, vol. 24, no. 1, pp. 59–71, 2005.
- [21] H. Huang, E. Ozkirimli, and C. B. Post, "Comparison of three perturbation molecular dynamics methods for modeling conformational transitions," *Journal of Chemical Theory and Computation*, vol. 5, no. 5, pp. 1304–1314, 2009.
- [22] S. Izrailev, S. Stepaniants, and K. Schulten, "Applications of steered molecular dynamics to protein-ligand/membrane binding," *Biophysical Journal*, vol. 74, no. 2, pp. A177–A177, 1998.
- [23] M. Ø. Jensen, Y. Yin, E. Tajkhorshid, and K. Schulten, "Sugar transport across lactose permease probed by steered molecular dynamics," *Biophysical Journal*, vol. 93, no. 1, pp. 92–102, 2007.
- [24] H. Lu, B. Isralewitz, A. Krammer, V. Vogel, and K. Schulten, "Unfolding of titin immunoglobulin domains by steered molecular dynamics simulation," *Biophysical Journal*, vol. 75, no. 2, pp. 662–671, 1998.
- [25] O. V. Levstova, M. Y. Antonov, D. Y. Mordvintsev, Y. N. Utkin, K. V. Shaitan, and M. P. Kirpichnikov, "Steered molecular dynamics simulations of cobra cytotoxin interaction with zwitterionic lipid bilayer: no penetration of loop tips into membranes," *Computational Biology and Chemistry*, vol. 33, no. 1, pp. 29–32, 2009.
- [26] A. Babakhani, A. A. Gorfe, J. Gullingsrud, J. E. Kim, and J. A. McCammon, "Peptide insertion, positioning, and stabilization in a membrane: insight from an all-atom molecular dynamics simulation," *Biopolymers*, vol. 85, no. 5–6, pp. 490–497, 2007.
- [27] C.-W. Tsai, N. Y. Hsu, C. H. Wang et al., "Coupling molecular dynamics simulations with experiments for the rational design of indolicidin-analogous antimicrobial peptides," *Journal of Molecular Biology*, vol. 392, no. 3, pp. 837–854, 2009.
- [28] W. Humphrey, A. Dalke, and K. Schulten, "VMD: visual molecular dynamics," *Journal of Molecular Graphics*, vol. 14, no. 1, pp. 33–38, 1996.
- [29] A. Elmquist, M. Hansen, and Ü. Langel, "Structure-activity relationship study of the cell-penetrating peptide pVEC," *Biochimica et Biophysica Acta*, vol. 1758, no. 6, pp. 721–729, 2006.
- [30] P. Joanne, C. Galanth, N. Goasdoué et al., "Lipid reorganization induced by membrane-active peptides probed using differential scanning calorimetry," *Biochimica et Biophysica Acta*, vol. 1788, no. 9, pp. 1772–1781, 2009.
- [31] J. C. Phillips, R. Braun, W. Wang et al., "Scalable molecular dynamics with NAMD," *Journal of Computational Chemistry*, vol. 26, no. 16, pp. 1781–1802, 2005.
- [32] A. D. MacKerell, D. Bashford, M. Bellott et al., "All-atom empirical potential for molecular modeling and dynamics studies of proteins," *Journal of Physical Chemistry B*, vol. 102, no. 18, pp. 3586–3616, 1998.
- [33] S. E. Feller and A. D. MacKerell, "An improved empirical potential energy function for molecular simulations of phospholipids," *Journal of Physical Chemistry B*, vol. 104, no. 31, pp. 7510–7515, 2000.
- [34] W. L. Jorgensen, "Transferable intermolecular potential functions for water, alcohols, and ethers. Application to liquid water," *Journal of the American Chemical Society*, vol. 103, no. 2, pp. 335–340, 1981.
- [35] T. Darden, D. York, and L. Pedersen, "Particle mesh Ewald: an N-log(N) method for Ewald sums in large systems," *The Journal of Chemical Physics*, vol. 98, no. 12, pp. 10089–10092, 1993.
- [36] G. J. Martyna, D. J. Tobias, and M. L. Klein, "Constant pressure molecular dynamics algorithms," *The Journal of Chemical Physics*, vol. 101, no. 5, pp. 4177–4189, 1994.
- [37] S. E. Feller, Y. Zhang, R. W. Pastor, and B. R. Brooks, "Constant pressure molecular dynamics simulation: the Langevin piston method," *The Journal of Chemical Physics*, vol. 103, no. 11, pp. 4613–4621, 1995.
- [38] I. Vorobyov, L. Li, and T. W. Allen, "Assessing atomistic and coarse-grained force fields for protein-lipid interactions: the formidable challenge of an ionizable side chain in a membrane," *Journal of Physical Chemistry B*, vol. 112, no. 32, pp. 9588–9602, 2008.
- [39] H. D. Herce, A. E. Garcia, J. Litt et al., "Arginine-rich peptides destabilize the plasma membrane, consistent with a pore formation translocation mechanism of cell-penetrating peptides," *Biophysical Journal*, vol. 97, no. 7, pp. 1917–1925, 2009.
- [40] M. J. Harms, J. L. Schlessman, G. R. Sue, and B. Garci'a-Moreno, "Arginine residues at internal positions in a protein are always charged," *Proceedings of the National Academy of Sciences of the United States of America*, vol. 108, no. 47, pp. 18954–18959, 2011.
- [41] J. L. MacCallum, W. F. D. Bennett, and D. P. Tieleman, "Partitioning of amino acid side chains into lipid bilayers: results from computer simulations and comparison to experiment," *Journal of General Physiology*, vol. 129, no. 5, pp. 371–377, 2007.
- [42] J. L. MacCallum, W. F. D. Bennett, and D. P. Tieleman, "Distribution of amino acids in a lipid bilayer from computer simulations," *Biophysical Journal*, vol. 94, no. 9, pp. 3393–3404, 2008.
- [43] J. L. MacCallum, W. F. Bennett, and D. P. Tieleman, "Transfer of arginine into lipid bilayers is nonadditive," *Biophysical Journal*, vol. 101, no. 1, pp. 110–117, 2011.
- [44] C. W. Tsai, N. Y. Hsu, C. H. Wang et al., "Coupling molecular dynamics simulations with experiments for the rational design of indolicidin-analogous antimicrobial peptides," *Journal of Molecular Biology*, vol. 392, no. 3, pp. 837–854, 2009.
- [45] Z. Bryant, V. S. Pande, and D. S. Rokhsar, "Mechanical unfolding of a  $\beta$ -hairpin using molecular dynamics," *Biophysical Journal*, vol. 78, no. 2, pp. 584–589, 2000.
- [46] C. Jarzynski, "Nonequilibrium equality for free energy differences," *Physical Review Letters*, vol. 78, no. 14, pp. 2690–2693, 1997.
- [47] J. Liphardt, S. Dumont, S. B. Smith, I. Tinoco, and C. Bustamante, "Equilibrium information from nonequilibrium measurements in an experimental test of Jarzynski's equality," *Science*, vol. 296, no. 5574, pp. 1832–1835, 2002.
- [48] S. Park and K. Schulten, "Calculating potentials of mean force from steered molecular dynamics simulations," *Journal of Chemical Physics*, vol. 120, no. 13, pp. 5946–5961, 2004.

## Research Article

# Toward Structure Prediction for Short Peptides Using the Improved SAAP Force Field Parameters

Kenichi Dedachi,<sup>1</sup> Taku Shimosato,<sup>1</sup> Toshiya Minezaki,<sup>2</sup> and Michio Iwaoka<sup>1</sup>

<sup>1</sup> Department of Chemistry, School of Science, Tokai University, Kitakaname, Hiratsuka-shi, Kanagawa 259-1292, Japan

<sup>2</sup> Laboratory of General Education for Science and Technology, School of Science, Tokai University, Kitakaname, Hiratsuka-shi, Kanagawa 259-1292, Japan

Correspondence should be addressed to Michio Iwaoka; [miwaoka@keyaki.cc.u-tokai.ac.jp](mailto:miwaoka@keyaki.cc.u-tokai.ac.jp)

Received 9 November 2012; Revised 5 January 2013; Accepted 9 January 2013

Academic Editor: Yifat Miller

Copyright © 2013 Kenichi Dedachi et al. This is an open access article distributed under the Creative Commons Attribution License, which permits unrestricted use, distribution, and reproduction in any medium, provided the original work is properly cited.

Based on the observation that Ramachandran-type potential energy surfaces of single amino acid units in water are in good agreement with statistical structures of the corresponding amino acid residues in proteins, we recently developed a new all-atom force field called SAAP, in which the total energy function for a polypeptide is expressed basically as a sum of single amino acid potentials ( $E^{\text{SAAP}}$ ) and electrostatic ( $E^{\text{ES}}$ ) and Lennard-Jones ( $E^{\text{LJ}}$ ) potentials between the amino acid units. In this study, the SAAP force field (SAAPFF) parameters were improved, and classical canonical Monte Carlo (MC) simulation was carried out for short peptide models, that is, Met-enkephalin and chignolin, at 300 K in an implicit water model. Diverse structures were reasonably obtained for Met-enkephalin, while three folded structures, one of which corresponds to a native-like structure with three native hydrogen bonds, were obtained for chignolin. The results suggested that the SAAP-MC method is useful for conformational sampling for the short peptides. A protocol of SAAP-MC simulation followed by structural clustering and examination of the obtained structures by *ab initio* calculation or simply by the number of the hydrogen bonds (or the hardness) was demonstrated to be an effective strategy toward structure prediction for short peptide molecules.

## 1. Introduction

In conformational analysis of short peptides, Monte Carlo (MC) and molecular dynamics (MD) simulation techniques have been widely applied [1, 2], in which a set of potential energy functions (a so-called force field), such as ECEPP [3, 4], AMBER [5–8], CHARMM [9], OPLS [10, 11], and GROMOS [12], is employed to define the relation between the structure and the potential energy. However, it is still not practical to search for the possible conformers comprehensively within a limited computing time without using advanced sampling methods, such as multicanonical [13, 14] and replica-exchange [15–17] methods, which have been developed to overcome the sampling problem. In recent years, various types of coarse-grained force fields, such as AMBER-UA [18], UNRES [19–23], and MARTINI [24, 25], have also been developed in order to reduce time to compute the potential energy. For instance, the UNRES force field

successfully simulated the aggregation process and stable structure of  $\beta$ -amyloid protein oligomers that are regarded as pathologic factors of Alzheimer's disease [26].

On the other hand, we recently discovered the interesting feature of protein structures that Ramachandran-type potential energy surfaces of single amino acid units in water obtained by *ab initio* molecular orbital calculation are almost identical with statistical distributions of the Ramachandran plots obtained from protein databank (PDB) [27, 28]. In other words, the amino acid residues in proteins seem to statistically follow Boltzmann distributions on the single amino acid potential (SAAP) surfaces in water. Although physicochemical implications of this unexpected similarity are not yet clear, the finding strongly suggests prominent importance of SAAP as a determinant of protein structures. This point would also be supported by the previous experimental result by Dobson and coworkers [29, 30] that  $\varphi$  and  $\psi$  dihedral angle distributions of individual amino acid residues

of a polypeptide in a random-coil state can be expressed by use of the Ramachandran plots, as well as by the theoretical approaches by Sakae and Okamoto [31] and Kamiya et al. [32] to the optimization of conventional all-atom force field parameters by using the Ramachandran plots.

A discovery of the similarity between the SAAP in water and the statistical structure of the amino acid residues in folded proteins has prompted us to develop a new force field called SAAP for polypeptide molecules [33, 34]. The SAAP force field (SAAPFF) is entirely different from conventional force fields in that a polypeptide is divided to the amino acid units, not to the atomic units, solvent effects are implicitly included in the parameters, and the atomic charges are not constant but variable depending on the conformation of the amino acid units. In the SAAPFF, the total potential energy ( $E^{\text{TOTAL}}$ ) for a polypeptide is expressed by (1) as the following:

$$E^{\text{TOTAL}} = E^{\text{SAAP}} + E^{\text{ES}} + E^{\text{LJ}} + E^{\text{OTHERS}}, \quad (1)$$

where  $E^{\text{SAAP}}$  is a sum of potential energies (SAAP) for the individual amino acid units,  $E^{\text{ES}}$  and  $E^{\text{LJ}}$  are electrostatic and Lennard-Jones potentials between the amino acid units, and  $E^{\text{OTHERS}}$  is the other correlation term, which is ignored in a current version of SAAPFF. Detailed description of these terms and the simulation program was given previously (see also Supplementary Material available online at <http://dx.doi.org/10.1155/2013/407862>) [33, 34]. Canonical MC simulation using the SAAPFF reasonably reproduced randomly fluctuating conformation of Met-enkephalin. However, for chignolin the SAAP-MC simulation did not afford the native  $\beta$ -hairpin structure when the simulation was started from the extended structure [34]. Thus, the previous SAAPFF parameters were a little too rough to be applied for structure prediction of the short peptide. In this study, the SAAPFF parameters have been improved in several points, and accuracy of the improved SAAP simulation suite to search for possible conformers of short peptides has been evaluated by performing the molecular simulation for Met-enkephalin and chignolin. The results were then compared with those obtained by the conventional AMBER-MD simulation method using the amber99sb force field [1] combined with the generalized Born solvent model [35–37]. A protocol of SAAP-MC simulation followed by structural clustering is suggested to be an effective strategy toward structure prediction for short peptide molecules.

## 2. Method of Calculations

**2.1. Model Peptides.** Met-enkephalin and chignolin without N- and C-terminal protecting groups were employed as model short peptides. Met-enkephalin is a short peptide, which consists of five residues (Tyr–Gly–Gly–Phe–Met) as shown in Figure 1. According to previous experimental [38] and theoretical [39–50] studies, the structure of this short peptide randomly fluctuates in water, while the presence of some characteristic conformations with intramolecular hydrogen bonds was indicated *in vacuo* [51–53]. Met-enkephalin is a peptide widely used for testing performance of developed molecular simulation methodologies.

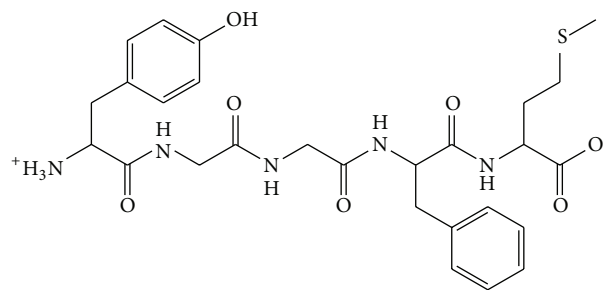


FIGURE 1: Structure of Met-enkephalin.

Chignolin has a unique folded  $\beta$ -hairpin structure in water, although it is a short peptide consisting of ten amino acid residues (Gly–Tyr–Asp–Pro–Glu–Thr–Gly–Thr–Trp–Gly) [54]. Molecular simulation for this miniprotein has been performed actively by using AMBER and OPLS force fields [55–64]. As shown in Figure 2, chignolin folds around Pro4–Glu5–Thr6 to form a  $\beta$ -hairpin structure, which is stabilized by three intramolecular hydrogen bonds, Gly7(N)···Asp3(O) (H-bond I), Thr8(N)···Asp3(O) (H-bond II), and Asp3(N)···Thr8(O) (H-bond III), and a hydrophobic interaction between the aromatic rings of Tyr2 and Trp9.

**2.2. Improvement of the SAAPFF Parameters.** The SAAPFF parameters are comprised of a potential energy, atomic coordinates, atomic charges, and Lennard-Jones potential parameters for all possible conformations of the single amino acid unit (HCO–Xaa–NH<sub>2</sub>). The conformations are defined by dihedral angles,  $\phi$ ,  $\psi$ ,  $\chi_1$ ,  $\chi_2$ , and so forth, each with an interval of 15 degrees. In this study, the SAAPFF parameters previously developed [33, 34] were improved in the following points.

First, the parameters for main-chain, Pro, and Val in water, which were obtained in the previous version [34] by single-point calculation with the IEFPCM [65–67] solvent model using the structures optimized *in vacuo*, were replaced with those obtained by geometry optimization in water at the HF/6-31+G(d) level using the IEFPCM model in a Gaussian03 program (rev. E.01) [68]. The similar calculation level has been widely applied for small biomolecules [69, 70]. Relaxation of the potential surfaces in the implicit water model should improve accuracy of the SAAPFF.

Second, atomic charges of the SAAPFF parameters, which are variables as a function of the structure of an amino acid unit, were switched for all amino acids from Mulliken charges to electrostatic potential (ESP) charges [71] that were obtained at the recommended higher MP2/6-31G(d,p) level [72] using the IEFPCM solvent model. The ESP charges are defined to reproduce the electrostatic potential surface and are used in conventional force fields as reliable atomic charges. Therefore, the use of ESP charges would reproduce electrostatic interactions, that is, the  $E^{\text{ES}}$  term, more appropriately than the Mulliken charges.

Third, the parameters of potential energies for the main-chain unit were further improved as follows. The SAAPFF

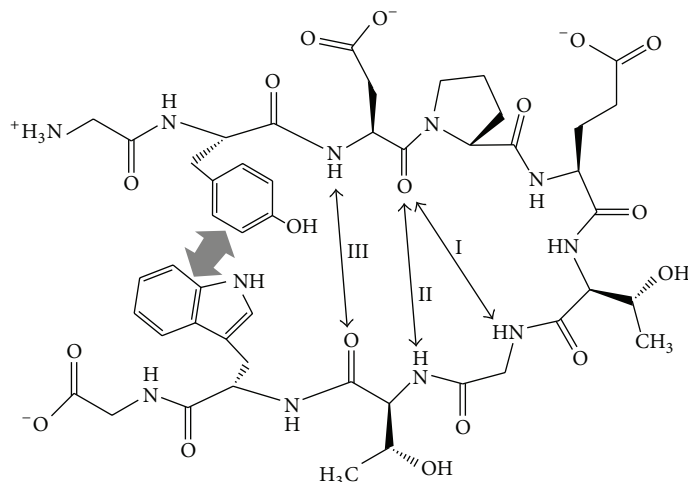


FIGURE 2: Structure of chignolin. Three native hydrogen bonds (H-bonds I, II, and III) and a hydrophobic interaction between Tyr2 and Trp9 are indicated by arrows [58].

parameters for most amino acids, except for Gly, Ala, Pro, and Val, are divided into the main-chain and side-chain units according to the side-chain separation approximation method [34]. In this approximation, the main-chain unit was capped with a *tert*-butyl group, which was fixed eclipsed to the main-chain part during geometry optimization to obtain the SAAPFF parameters. However, this method brought a statistical error that the SAAP energies thus obtained are slightly larger than those obtained without the approximation, due probably to distortion of the bond angles derived from the fixed geometry. Indeed, such a statistical error was evident for the case of Val [34]. Therefore, the energies were replaced with those calculated for the relaxed structures, which were obtained by geometry optimization with the *tert*-butyl group relaxed in water, while for structural parameters (i.e., atomic coordinates and atomic charges) the geometry with the *tert*-butyl group fixed eclipsed was still employed in order to avoid abnormally short atomic contacts between the main-chain and side-chain units after the connection.

**2.3. Simulation Conditions.** Conformational properties of Met-enkephalin and chignolin in water were studied by SAAP-MC and AMBER-MD [73] simulations. The SAAP-MC simulation was carried out at 300 K in water by using the improved SAAPFF parameters, in which solvation effects were implemented implicitly. The conventional Metropolis method [74, 75] and the Mersenne Twister random number generator [76] were employed for the MC simulation. At each MC step, one dihedral angle, randomly chosen from all dihedral angles including main-chain and side-chain dihedral angles, was changed randomly with a maximum displacement angle of  $\pm 32$  degree. The new structure was constructed by the interpolation of the SAAPFF parameters and subsequent connection of the single amino acid units, and the potential energy was calculated by (1). The potential energy thus obtained was then compared with the previous

one. Ten trajectories with total MC steps of 100 million were obtained for Met-enkephalin, while twenty trajectories with total MC steps of 2 billion were obtained for chignolin. As an initial structure of Met-enkephalin for the SAAP-MC simulation, the extended structure from PDB (PDB ID: 1PLW) [77] was employed. On the other hand, extended (defined by all main-chain  $\phi$  and  $\psi$  dihedral angles of  $-180$  degree) and native folded (PDB ID: 1UAO) [54] structures were selected for chignolin as the initial structures. An Intel Xeon W3550 3.06 GHz processor with 12 GB memory was employed as a platform for calculation. The computing time of SAAP-MC simulation for Met-enkephalin was about 6 hours and for chignolin was about 11 days.

For comparison, ten trajectories of AMBER-MD [73] simulation were also calculated for Met-enkephalin and chignolin, respectively, in water at 300 K. The simulation time was  $1\ \mu\text{s}$  with a time step of 2 fs, and a cut-off distance of nonbonded interactions was 12 Å. Solvation effects were implicitly considered by using the generalized Born model ( $\text{igb} = 1$ ) [35–37] with a dielectric constant of 78.5, following the recent study by Götz et al. [78]. The AMBER10 program [73] with the amber99sb force field [1] was used. The computing time of the AMBER-MD simulation to obtain one trajectory was about 165 hours for Met-enkephalin, and that for chignolin was about 18 days, on the same calculation platform used for the SAAP-MC simulation.

**2.4. Data Analysis.** The 10,000 structures of Met-enkephalin that were extracted in every 10,000 step from the SAAP-MC simulation trajectory were classified to twenty structural clusters by using a clustering algorithm called the *k*-means method [79] based on the RMSD for the main-chain C, O, and N atoms or all heavy atoms except for the hydrogen atoms. Similarly, ten structural clusters were obtained for chignolin from the 20,000 structures extracted in every 100,000 step from the SAAP-MC simulation trajectories. On the other

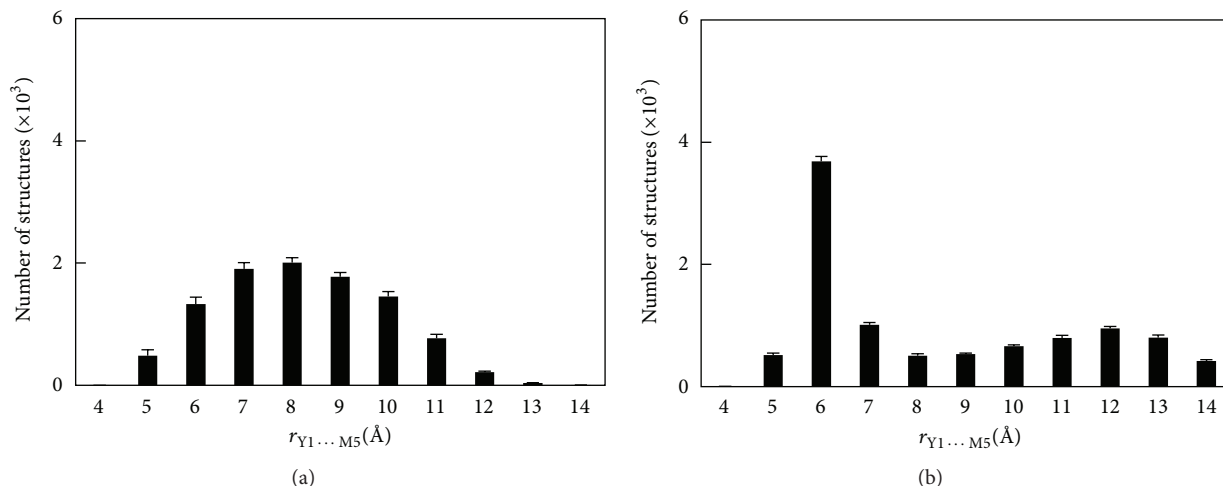


FIGURE 3: Histograms of the distance between  $C\alpha$  atoms of Tyr1 and Met5 for 10,000 structures of Met-enkephalin obtained by the SAAP-MC (a) and AMBER-MD (b) simulations at 300 K in water. The results from ten trajectories were averaged. See the text for details of simulation conditions.

hand, 10,000 structures were extracted in every 100 ps from the AMBER-MD trajectories for both Met-enkephalin and chignolin. The obtained structures were classified to ten or twenty clusters by application of the  $k$ -means method under the same conditions to those applied for the SAAP-MC simulation results.

For chignolin, the RMSD values with respect to the native structure were also calculated for the structures extracted from the SAAP-MC and AMBER-MD trajectories by using the amber-ptraj program [7, 8] based on the main-chain atoms or all heavy atoms. The free-energy surfaces of chignolin were further analyzed by using all trajectories obtained from the SAAP-MC simulation according to (2):

$$\Delta F = -RT \ln \left( \frac{P}{P_{\min}} \right), \quad (2)$$

where  $P$  is a probability of the structures with the corresponding structural parameters,  $P_{\min}$  is the probability of the structure that had the lowest energy,  $\Delta F$  is a difference in the free energy,  $R$  is a gas constant, and  $T$  is an absolute temperature. Ramachandran-type  $\varphi$ - $\psi$  free-energy surfaces were obtained for each amino acid residue by dividing the surface into  $10 \times 10$  degree units, while main-chain RMSD versus hydrogen bond or hydrogen bond versus hydrogen bond free-energy surfaces were obtained by dividing the surface into  $0.1 \times 0.1$  Å units.

**2.5. Ab Initio Calculation.** Relative energies of the representative structures obtained for chignolin by the SAAP-MC simulation were calculated in water by the *ab initio* molecular orbital method. The calculation was performed at the HF/IEFPCM/6-31+G(d,p) level by using a Gaussian03 program [68]. The polarizable continuum model using the integral equation formalism variant (IEFPCM), which is equipped as the default self-consistent reaction field method, was employed for the calculation in water.

### 3. Results

**3.1. Met-Enkephalin by SAAP-MC and AMBER-MD.** Energetic trajectories of SAAP-MC and AMBER-MD simulations for Met-enkephalin were obtained in an implicit water model at 300 K (see Figure S1). In SAAPFF, the total energy  $E^{\text{TOTAL}}$  is basically expressed as a sum of  $E^{\text{SAAP}}$ ,  $E^{\text{ES}}$ , and  $E^{\text{LJ}}$ . The values of these energetic terms were maintained stable during the SAAP-MC simulation with large fluctuation for  $E^{\text{SAAP}}$  and  $E^{\text{LJ}}$ , while the value of  $E^{\text{ES}}$  was almost zero, as observed previously [34]: the large dielectric constant of water would make the electrostatic interaction between the amino acid residues ignorable. Similarly, the total energy was maintained stable for the AMBER-MD simulation. However, the distribution of the distance between the terminal  $C\alpha$  atoms ( $r_{Y1...M5}$ ) was significantly different for the two simulation methods. The value of  $r_{Y1...M5}$  dispersed in a range from 5 to 12 Å in the SAAP-MC simulation, while those converged at around 6 Å in the AMBER-MD simulation (Figure 3). The results suggested that the structures obtained from the SAAP-MC simulation contain diverse conformations and are more extended than those obtained from the AMBER-MD simulation on the average. Indeed, when the structures were classified into twenty clusters based on the RMSD values for the main-chain atoms, various types of structures were obtained from the SAAP-MC trajectory. The representative examples are shown in Figure 4. The structures are different from each other with a diverse  $r_{Y1...M5}$  value, and there is no hydrogen bond in the three representative structures. In contrast, the structures of Met-enkephalin obtained from the AMBER-MD trajectory seemed to be trapped in local energy minimums during the simulation (see Figure S2).

**3.2. Chignolin by SAAP-MC and AMBER-MD.** Twenty trajectories were obtained for chignolin by SAAP-MC simulation. The structures in each trajectory were classified to

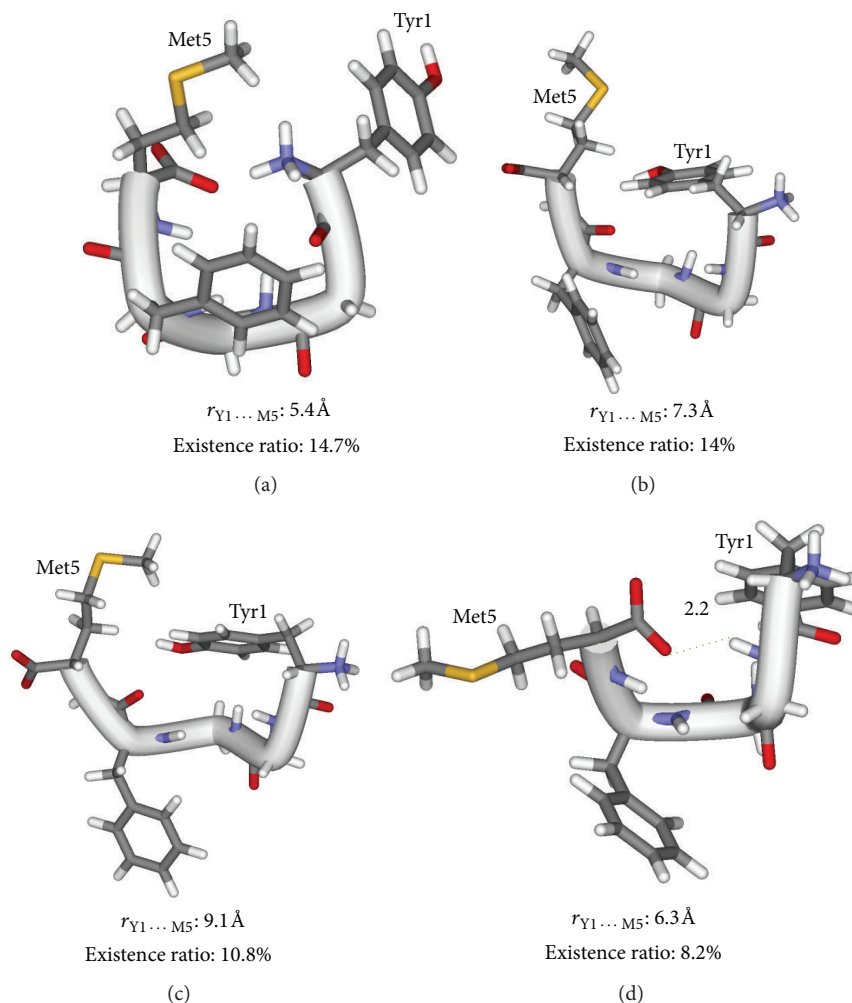


FIGURE 4: Representative structures of Met-enkephalin obtained by the SAAP-MC simulation at 300 K in water (trajectory 1). The obtained 10,000 structures were analyzed by a structural clustering algorithm using the  $k$ -means method based on the main-chain RMSD. A distance of the hydrogen bond is given in a unit of Å.

ten clusters based on the main-chain RMSD by using the  $k$ -means method. According to the main-chain folds, that is, combination of the  $\varphi$ - $\psi$  dihedral angles for the amino acid residues, the obtained clusters were further classified to three representative structures, which are called here A, B, and C (Figure 5). Populations of the three structures are summarized in Table 1. Structure A has a native-like main-chain fold stabilized by three hydrogen bonds, which are the same as those observed in the native structure (i.e., H-bonds I–III). However, the hydrophobic interaction between the aromatic side chains of Tyr2 and Trp9 is not present. Structures B and C have nonnative conformation with a common type II  $\beta$ -turn around Thr6 and Gly7. A weak hydrogen bond exists between Glu5(O) and Thr8(N) with a distance about 4.0 Å. However, the conformations of the C-terminals are different from each other. Other minor structures have various local and global conformations, such as a type I  $\beta$ -turn, a helical conformation, and other conformations.

In the trajectories from 1 to 12, the existence ratio of structure A was high (31.2 to 58.5%), whereas the ratio was much lower than that of the misfolded structure B in the remaining trajectories. The mean ratio for structure A averaged for all trajectories was 29.2%. On the other hand, when the clustering analysis was performed based on all-atom RMSD, the native-like structure ( $A'$ ) was obtained from 0 to 19.5% (Table 1). The existence ratio of structure  $A'$  averaged over all trajectories was 6.7%. Structure  $A'$  maintains three native H-bonds as well as a hydrophobic interaction between Tyr2 and Trp9 (Figure 5). The all-atom and main-chain RMSD values of structure  $A'$  from the native structure were 2.6 and 2.0 Å, respectively, suggesting that structure  $A'$  keeps the native fold. The trace of the main-chain RMSD with respect to the native structure is shown in Figure 6(a) for the case of trajectory 10, where structures A and B are involved in almost equal amounts. The RMSD values fluctuated between 1 and 6 Å, and repeats of the structural transitions were observed.

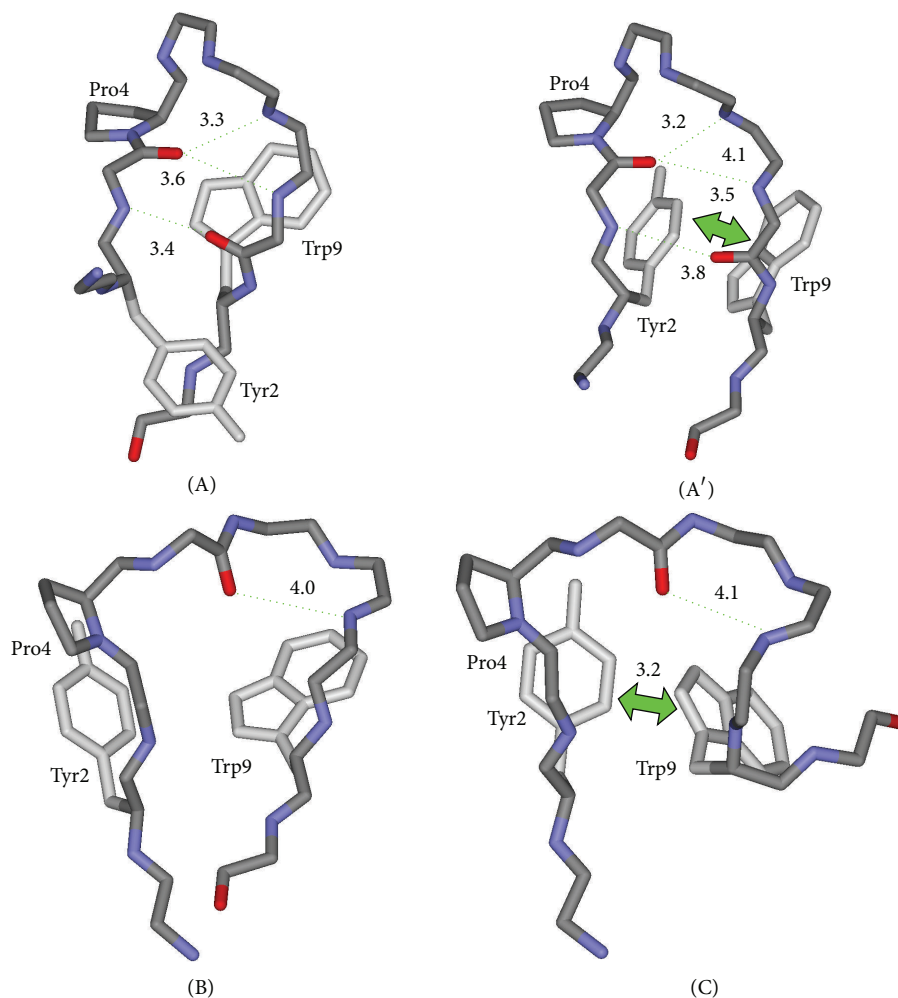


FIGURE 5: Representative structures of chignolin obtained by the SAAP-MC simulation at 300 K in water. The obtained 20,000 structures were analyzed by a structural clustering algorithm using the  $k$ -means method. Structures (A), (B), and (C) were obtained based on the main-chain RMSD. Structure (A') was obtained based on the all-atom RMSD. Distances of the hydrogen bonds and the hydrophobic interaction are given in a unit of Å.

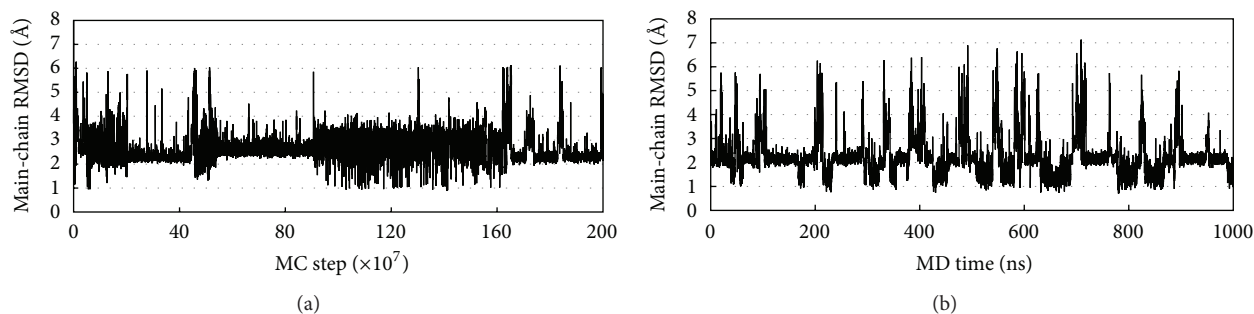


FIGURE 6: Traces of the main-chain RMSD obtained for chignolin by the SAAP-MC (trajectory 10) (a) and AMBER-MD (trajectory 1) (b) simulations at 300 K in water. The RMSD values were calculated with respect to the native structure.

Similarly, in the AMBER-MD simulation, the main-chain RMSD value fluctuated between 1 and 6 Å (Figure 6(b)). The structural clustering analysis showed that the native structure with three native hydrogen bonds was involved about 30% (Figure S5).

The convergence of the SAAP-MC simulation is not clear from Table 1. However, the similar relative populations were obtained for structures A (~30% including 6% of A') and B (~60%) when the simulation was started from the native structure. Moreover, in our preliminary results of

TABLE 1: Existence ratios (%) of representative structures of chignolin obtained by the SAAP-MC simulation at 300 K in water.

Trajectory number	A (A')	B	C	Other
1	58.5 (11.2)	25.9	2.3	13.3
2	54.7 (11.3)	26.6	6.6	12.1
3	50.4 (8.4)	42.4	3.8	3.4
4	49.3 (11.4)	30.7	2.9	17.1
5	45.4 (10.6)	37.8	6.1	10.7
6	44.3 (8.9)	47.9	0.0	7.8
7	37.9 (19.5)	40.2	2.4	19.5
8	37.6 (8.5)	27.9	0.0	34.5
9	36.5 (11.2)	30.7	6.2	26.6
10	34.7 (6.6)	27.3	4.2	33.8
11	32.1 (8.0)	32.9	5.5	29.5
12	31.2 (9.7)	23.5	0.0	45.3
13	19.8 (3.5)	43.7	5.3	31.2
14	14.2 (2.5)	31.8	0.0	54.0
15	13.6 (0.0)	56.8	6.3	23.3
16	12.8 (2.6)	60.0	7.9	19.3
17	10.5 (0.0)	59.3	0.0	30.2
18	1.1 (0.0)	65.1	0.0	33.8
19	0.0 (0.0)	70.4	5.5	24.1
20	0.0 (0.0)	83.2	10.2	6.6
Average	29.2 (6.7)	43.2	3.8	23.8

TABLE 2: Relative energies of structures A–C determined by *ab initio* calculation at the HF/IEFPCM/6-31+G(d,p) level in water.

Structures	SCF energy (a.u.)	Relative energy (kcal/mol)
A	-3800.42798	5.52
A'	-3800.43678	0.00
B	-3800.39878	23.85
C	-3800.43002	4.42

the SAAP-MC simulation using ten trajectories, almost the same mean populations were obtained for the representative structures (data not shown). Based on these observations, we employed the twenty trajectories shown in Table 2 for further analysis.

The structure with the smallest all-atom RMSD (1.3 Å) obtained from the twenty trajectories is superimposed on the native structure in Figure 7. The main-chain and C $\alpha$  atom RMSD values of this structure with respect to the native structure were 0.9 and 0.5 Å, respectively, confirming that the structure is almost identical to the native structure.

The Ramachandran-type free-energy surfaces obtained for Tyr2–Trp9 residues from all trajectories of the SAAP-MC simulation are shown in Figure 8. The profiles for Tyr2, Pro4, Glu5, and Thr6 fit well to the native structures, while the free-energy minimums for Asp3, Gly7, and Thr8 are slightly moved from the positions of the native structures. For Trp9, the stable areas corresponding to  $\alpha$  and  $\beta$  regions tend to

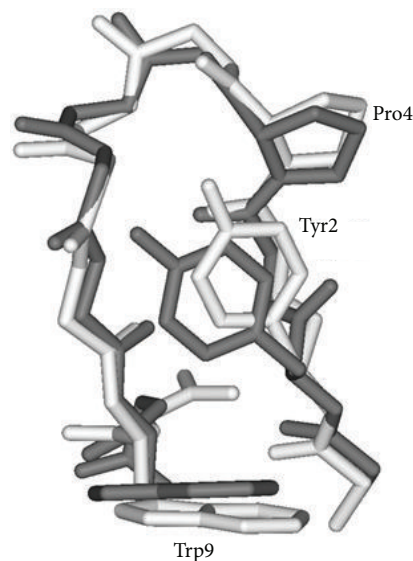


FIGURE 7: The structure of chignolin with the smallest all-atom RMSD (1.3 Å) obtained by the SAAP-MC simulation at 300 K in water (white) superimposed on the reference native structure (gray).

merge. This is roughly consistent with diversity in the C-terminal conformation of the native structure. The dihedral angles for structures A and A' are located around the energy minimum points on the free-energy surfaces. In contrast, structure B has different geometry from structures A and A' for Glu5 and Thr6: the  $\psi$  angles are ca. +110 ~ 130 degree. Structure C has the geometry with  $\psi$  angles of Glu5, Thr6, Thr8, and Trp9 different from those of structures A and A'. During the SAAP-MC simulation, mismatch of the main-chain dihedral angles for Glu5, Thr6, and Gly7 to the native structure occurred at high ratios.

The free-energy surface of chignolin projected on H-bonds I versus III plane and that projected on the main-chain RMSD versus H-bond II plane obtained from all trajectories are shown in Figure 9. In Figure 9(a), the most stable area was found at  $r_{(\text{H-bond I})} \sim 6.5 \text{ \AA}$  and  $r_{(\text{H-bond III})} \sim 4.5 \text{ \AA}$ . This energy minimum corresponds to the misfolded structure B. Another potential energy minimum was found at  $r_{(\text{H-bond I})} \sim 3.5 \text{ \AA}$  and  $r_{(\text{H-bond III})} \sim 3.5 \text{ \AA}$ , corresponding to structures A and A'. Similarly, two stable minimums were located in Figure 9(b);  $r_{(\text{H-bond II})} \sim 6.0 \text{ \AA}$  and RMSD  $\sim 2.3 \text{ \AA}$ , corresponding to structure B, and  $r_{(\text{H-bond II})} \sim 3.7 \text{ \AA}$  and RMSD  $\sim 3 \text{ \AA}$ , corresponding to structure A. The free-energy surfaces showed that structure A maintains three native hydrogen bonds, but it has larger main-chain RMSD from the native structure than misfolded and the most stable structure B. This conflict is ascribed to the N- and C-terminals of structure A, which are significantly apart due to the absence of a hydrophobic interaction between Tyr2 and Trp9 side chains. It should be noted that structure A' is separated from structure A in Figure 9(b).

3.3. Evaluation of the Relative Energies of Structures A–C by *Ab Initio* Calculation. To evaluate relative stabilities of structures

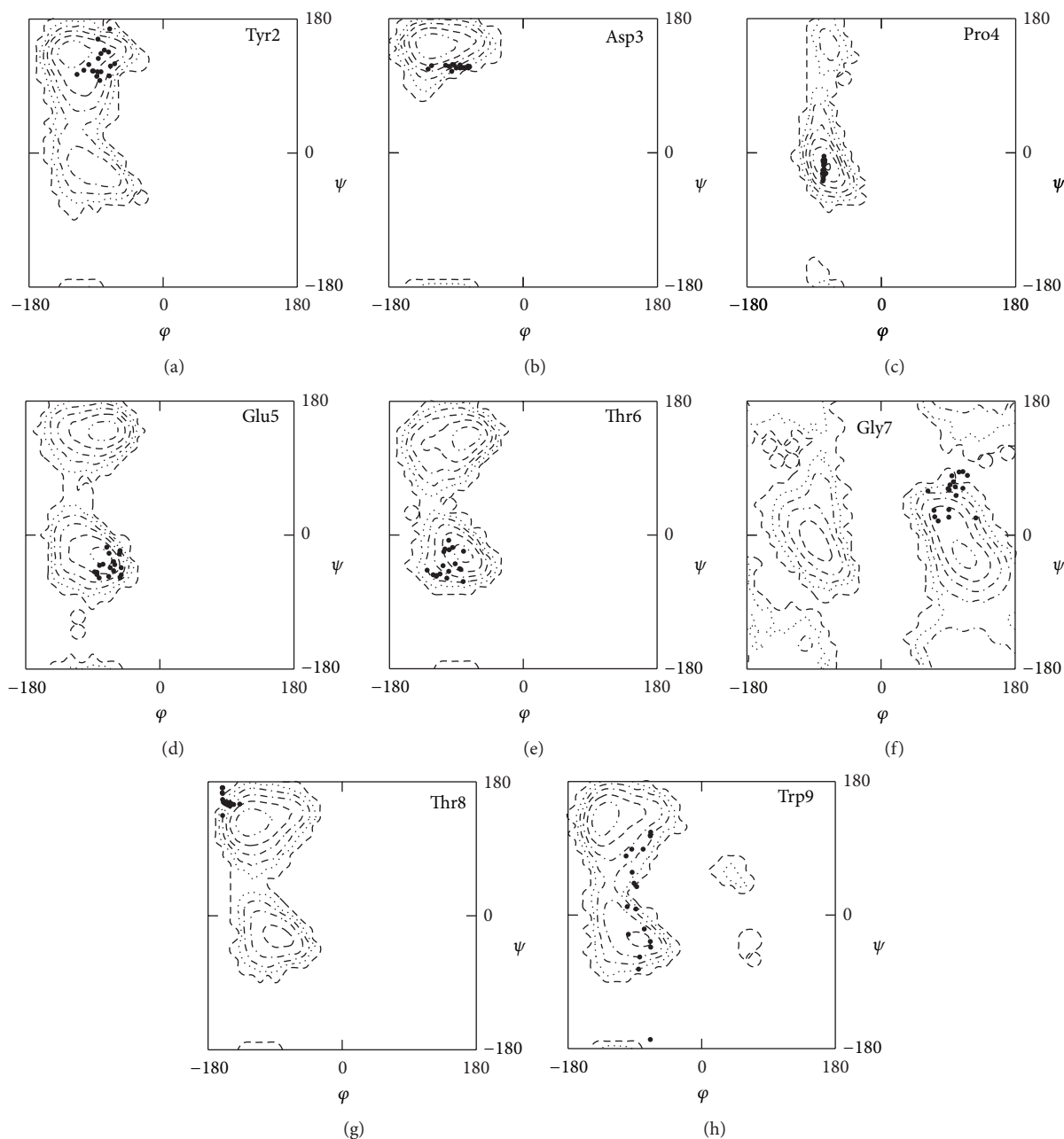


FIGURE 8: Ramachandran-type free-energy surfaces for Tyr2–Trp9 residues of chignolin obtained from all trajectories of the SAAP-MC simulation at 300 K in water along with the plots of the native structures determined by NMR [58]. Contour lines are drawn in an interval of 1 kcal/mol.

A, A', B, and C more accurately, single-point *ab initio* calculation was carried out. Table 2 lists the SCF and relative energies calculated in the IEFPCM solvent model. Although structure B was most populated in the SAAP-MC simulation, it is significantly unstable compared to the other structures, suggesting that structure B would not be populated in practical solutions. On the other hand, structure A' with a native fold was found to be the most stable. According to the *ab initio* calculation results, it is likely that the structures having more hydrogen bonds and/or a hydrophobic interaction between the aromatic rings are more stable.

## 4. Discussion

**4.1. Improvement of SAAPFF Parameters.** In this study, we have modified the SAAPFF parameters in the following points. (1) The main-chain, Pro, and Val parameters in water were replaced with those obtained by geometry optimization in water. (2) The atomic charges were replaced from Mulliken to ESP charges. (3) The energies of the main-chain unit were replaced with those obtained for the geometry with the *tert*-butyl cap being relaxed during the optimization. The effects of these modifications were found to be significant as the

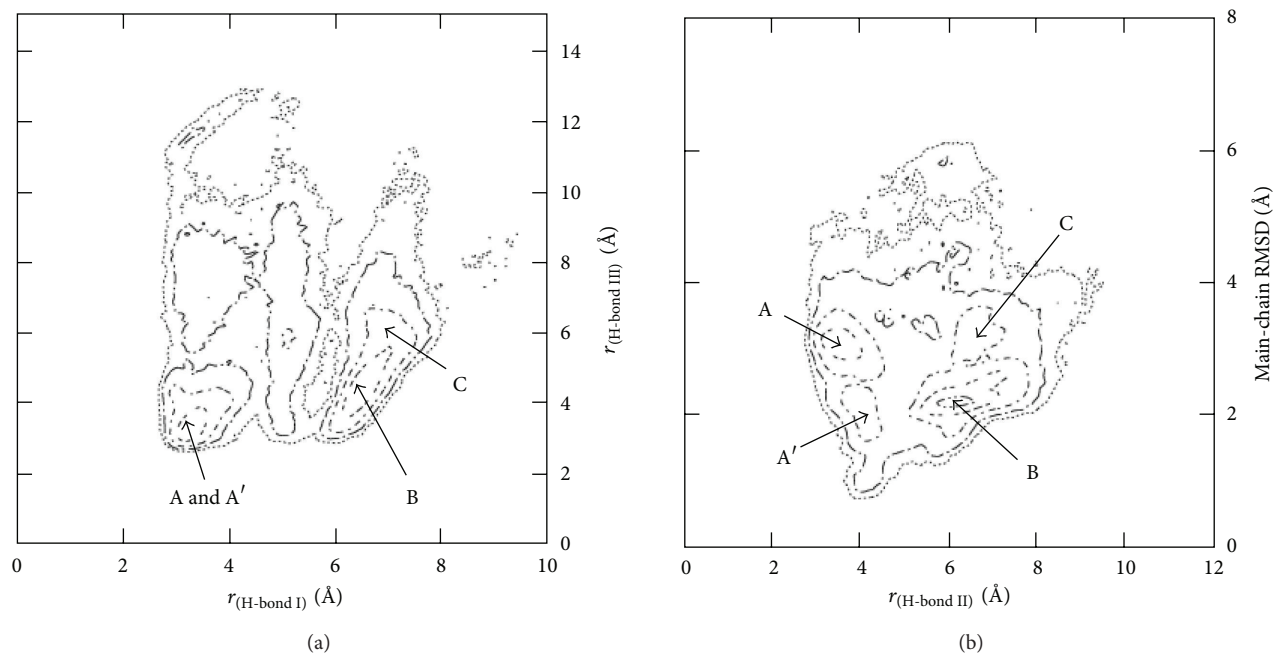


FIGURE 9: Free-energy surfaces of chignolin projected on the hydrogen bonds I versus III plane (a) and on the hydrogen bond II versus main-chain RMSD plane (b) obtained from all trajectories of the SAAP-MC simulation at 300 K in water. Contour lines are drawn in an interval of 1 kcal/mol.

SAAP-MC simulation using the new parameters reproduced the native structure of chignolin (structure A'), while it was not obtained when the simulation was performed by using the previous parameters [34].

The clustering of the structures obtained for chignolin by SAAP-MC simulation using the improved parameters showed that structures A and B are dominant in the implicit water model as shown in Table I. Structure A (29.2%) maintains three native hydrogen bonds, indicating the native main-chain fold, while nonnative structure B (43.2%) is stabilized by a type II  $\beta$ -turn. In addition, the structural clustering based on all-atom RMSD demonstrated that native structure A', which maintains not only the three native hydrogen bonds but also a hydrophobic interaction between the aromatic side chains of Tyr2 and Trp9, is involved in 6.7% of the total structures. The free-energy analysis clearly indicated that the main-chain dihedral angles of the each amino acid residue and the distances of H-bonds I-III for structures A and A' are consistent with the native structure (see Figures 8 and 9), although their populations were less than that of the misfolded structure B (*vide infra*).

In the meantime, randomly fluctuating structure was obtained for Met-enkephalin by using both the previous [34] and improved SAAPFF parameters (see Figures 3 and 4). This would be due to the two Gly residues, whose SAAP parameters have been modified only for the atomic charges in this study, being involved in the mid of the amino acid sequence.

There are a number of reports in the literature on the molecular simulation for chignolin by using conventional force fields to obtain the native structure from the

unfolded state [55–64]. In these studies, various state-of-the-art techniques of molecular simulation have been employed, including a multicanonical MD method [55, 56], a replica exchange MD method [57–60], a long-term conventional MD method by using a high-speed computer system [62], and originally developed MHOP and MSES methods [63, 64]. The values of all-atom RMSD for the obtained native structure were in a range from 1.3 to 1.8 Å with respect to the experimentally determined structure, which is smaller than that of structure A obtained as a major native-like structure by the SAAP-MC simulation in this study. Moreover, the AMBER-MD simulation carried out in this study showed that the native structure of chignolin is a little more frequently obtained by using the amber99sb force field than SAAPFF. Thus, it is obvious that further improvement of the SAAPFF parameters is required in future works.

**4.2. Efficiency of SAAP-MC Simulation for Conformational Sampling.** Previous studies applying an explicit water molecule model [43] or a generalized-ensemble method with RISM theory [39–42] have shown that Met-enkephalin has extended conformations in water. This feature was reasonably reproduced in this study by application of SAAPFF as shown in Figures 3 and 4. Clustering of the structures obtained from the SAAP-MC simulation indicated diverse conformations of Met-enkephalin in water. On the other hand, the AMBER-MD simulation for Met-enkephalin carried out in this study produced rather uniform folded conformations with intramolecular hydrogen bonds (see Figure S2), probably due to insufficient computing time. Thus, the SAAP-MC method would be useful for sampling possible conformations for

short peptide molecules in an implicit water model, although the accuracy is not satisfactory in terms of the reproducibility of the relative energies.

The efficiency for conformational sampling arises probably from a less number of variables used in the SAAPFF than that in the conventional force fields. In SAAPFF, the structure of peptides is defined only by the dihedral angles of the each amino acid unit, not by the cartesian coordinates of each atom. Acceleration of conformational sampling by reducing the number of structural parameters is a common strategy of coarse-grained force fields, such as united-atom force fields [18–26, 80, 81]. Efficiency of the SAAP-MC simulation for conformational sampling can also be explained by the fact that the solvent effects are implicitly included in the parameters of SAAPFF. This enables the SAAP-MC simulation in an implicit water model to be performed in the same computing time as that *in vacuo*.

**4.3. Prediction of Native Structures.** Although the accuracy of SAAPFF is not yet satisfied, the efficiency for conformational sampling would be advantageous for prediction of the stable structures of peptides in water. Therefore, we subsequently explored the application of the SAAP-MC method to predict the native structure of chignolin.

Indeed, it was found by single-point *ab initio* calculation in water at the HF/IEFPCM/6-31+G(d,p) level that structure A' is the most stable one in water among the structures shown in Figure 5 (see Table 2). The procedure should involve a large error in the energy because the structure is not optimized. However, the tendency of the relative energies would be reliable to some extent as previously demonstrated for HCO-Ala<sub>2</sub>-NH<sub>2</sub> *in vacuo* [33]. Thus, a protocol of SAAP-MC simulation followed by structure clustering and examination of the obtained structures by *ab initio* calculation would be a useful strategy toward the prediction of the native structure for short peptides. The relative energies obtained by *ab initio* calculation also suggested the possibility that structure B can be produced as an artifact of the force field because the relative energy was quite large (>20 kcal/mol).

As for prediction of the native structure, another simpler method would be possible based on the hardness (i.e., the number of interamino acid interactions or the depth of the potential hole on the free-energy surfaces) of the structures. As seen in Figure 5, structure B of chignolin maintains only one hydrogen bond, while structures A and A' hold three hydrogen bonds. In terms of the number of hydrogen bonds, it can be assumed that structures A and A' are more native-like than structure B, although the population of structure B was larger than those of structures A and A'. Indeed, the areas around the free-energy minimums corresponding to structures A and A' in Figures 9(a) and 9(b) are slightly narrower than those corresponding to structures B and C. Such robust structures on the conformational surface would be predicted to be more native-like than the structures with more conformational flexibility. Thus, we suggest that a protocol of SAAP-MC simulation followed by structural clustering and examination of the obtained structures by the number of hydrogen bonds (or the hardness) may be another simple strategy toward structure prediction for short peptide molecules.

## 5. Conclusions

The parameters of SAAPFF, which was previously developed to analyze the structures and folding of polypeptides, have been improved in several points in this study. (1) The main-chain, Pro, and Val parameters in water were replaced with those obtained by geometry optimization in the IEFPCM solvent model. (2) The atomic charges were replaced from Mulliken to ESP charges. (3) The energies of the main-chain unit were replaced with those obtained for the geometry with the *tert*-butyl cap being relaxed during the optimization. To investigate the accuracy of the improved SAAPFF parameters, the SAAP-MC simulation was carried out for Met-enkephalin and chignolin as model peptides. Analysis of the obtained structures revealed that the SAAP-MC simulation reasonably reproduced randomly fluctuating conformation for Met-enkephalin, while three folded structures, one of which corresponds to a native-like structure with three native hydrogen bonds, were obtained for chignolin. The latter result supported that the accuracy of the SAAPFF parameters has been remarkably improved from the previous ones, although the native structure of chignolin could not be assigned to the most stable structure in the conformational space defined by SAAPFF.

In the meantime, efficiency of SAAP-MC simulation for conformational sampling was demonstrated for Met-enkephalin as the SAAP-MC simulation afforded diverse structures. The feature, combined with the structural clustering analysis, was subsequently applied to the structure prediction of chignolin. Among the representative structures obtained by the clustering, structure A' with a native fold was assigned to the most stable structure according to *ab initio* calculation. Thus, a protocol of SAAP-MC simulation followed by structural clustering and examination of the obtained structures by *ab initio* calculation would be a useful strategy toward prediction of the native structure for short peptides. Alternatively, the structure with a maximum number of hydrogen bonds or with the hardest conformation on the potential surface may be considered to be the most native-like among the clustered structures. Applications of this method to structure prediction of other peptide molecules as well as further improvement of the SAAPFF parameters are being conducted by our group.

## Acknowledgment

This work was supported by Grant-in-Aid for Scientific Research on Innovative Areas (no. 2120005) from the Ministry of Education, Culture, Sports, Science and Technology. The SAAP force field parameters are available for download at <http://saap.sc.u-tokai.ac.jp/>.

## References

- [1] V. Hornak, R. Abel, A. Okur, B. Strockbine, A. Roitberg, and C. Simmerling, "Comparison of multiple amber force fields and development of improved protein backbone parameters," *Proteins: Structure, Function and Genetics*, vol. 65, no. 3, pp. 712–725, 2006.

- [2] J. W. Ponder and D. A. Case, "Force fields for protein simulations," *Advances in Protein Chemistry*, vol. 66, pp. 27–85, 2003.
- [3] F. A. Momany, R. F. McGuire, A. W. Burgess, and H. A. Scheraga, "Energy parameters in polypeptides. VII. Geometric parameters, partial atomic charges, nonbonded interactions, hydrogen bond interactions, and intrinsic torsional potentials for the naturally occurring amino acids," *Journal of Physical Chemistry*, vol. 79, no. 22, pp. 2361–2381, 1975.
- [4] G. Némethy, K. D. Gibson, K. A. Palmer et al., "Energy parameters in polypeptides. 10. Improved geometrical parameters and nonbonded interactions for use in the ECEPP/3 algorithm, with application to proline-containing peptides," *Journal of Physical Chemistry*, vol. 96, no. 15, pp. 6472–6484, 1992.
- [5] S. J. Weiner, P. A. Kollman, D. A. Case et al., "A new force field for molecular mechanical simulation of nucleic acids and proteins," *Journal of the American Chemical Society*, vol. 106, no. 3, pp. 765–784, 1984.
- [6] S. J. Weiner, P. A. Kollman, D. T. Nguyen, and D. A. Case, "An all atom force field for simulations of proteins and nucleic acids," *Journal of Computational Chemistry*, vol. 7, no. 2, pp. 230–252, 1986.
- [7] D. A. Pearlman, D. A. Case, J. W. Caldwell et al., "AMBER, a package of computer programs for applying molecular mechanics, normal mode analysis, molecular dynamics and free energy calculations to simulate the structural and energetic properties of molecules," *Computer Physics Communications*, vol. 91, no. 1–3, pp. 1–41, 1995.
- [8] D. A. Case, T. E. Cheatham III, T. Darden et al., "The Amber biomolecular simulation programs," *Journal of Computational Chemistry*, vol. 26, no. 16, pp. 1668–1688, 2005.
- [9] B. R. Brooks, R. E. Bruccoleri, B. D. Olafson, D. J. States, S. Swaminathan, and M. Karplus, "CHARMM: a program for macromolecular energy, minimization, and dynamics calculations," *Journal of Computational Chemistry*, vol. 4, no. 2, pp. 187–217, 1983.
- [10] W. L. Jorgensen and J. Tirado-Rives, "The OPLS potential functions for proteins. Energy minimizations for crystals of cyclic peptides and crambin," *Journal of the American Chemical Society*, vol. 110, no. 6, pp. 1657–1666, 1988.
- [11] W. L. Jorgensen and J. Tirado-Rives, "Potential energy functions for atomic-level simulations of water and organic and biomolecular systems," *Proceedings of the National Academy of Sciences of the United States of America*, vol. 102, no. 19, pp. 6665–6670, 2005.
- [12] W. R. P. Scott, P. H. Hünenberger, I. G. Tironi et al., "The GROMOS biomolecular simulation program package," *Journal of Physical Chemistry A*, vol. 103, no. 19, pp. 3596–3607, 1999.
- [13] U. H. E. Hansmann, Y. Okamoto, and F. Eisenmenger, "Molecular dynamics, langevin and hybrid Monte Carlo simulations in a multicanonical ensemble," *Chemical Physics Letters*, vol. 259, no. 3–4, pp. 321–330, 1996.
- [14] N. Nakajima, H. Nakamura, and A. Kidera, "Multicanonical ensemble generated by molecular dynamics simulation for enhanced conformational sampling of peptides," *Journal of Physical Chemistry B*, vol. 101, no. 5, pp. 817–824, 1997.
- [15] K. Hukushima and K. Nemoto, "Exchange monte carlo method and application to spin glass simulations," *Journal of the Physical Society of Japan*, vol. 65, no. 6, pp. 1604–1608, 1996.
- [16] Y. Sugita and Y. Okamoto, "Replica-exchange molecular dynamics method for protein folding," *Chemical Physics Letters*, vol. 314, no. 1–2, pp. 141–151, 1999.
- [17] Y. Okamoto, "Generalized-ensemble algorithms: enhanced sampling techniques for Monte Carlo and molecular dynamics simulations," *Journal of Molecular Graphics and Modelling*, vol. 22, no. 5, pp. 425–439, 2004.
- [18] L. Yang, C. Tan, M.-J. Hsieh et al., "New-generation amber united-atom force field," *The Journal of Physical Chemistry B*, vol. 110, no. 26, pp. 13166–13176, 2006.
- [19] A. Liwo, S. Oldziej, M. R. Pincus, R. J. Wawak, S. Rackovsky, and H. A. Scheraga, "A united-residue force field for off-lattice protein-structure simulations. I. Functional forms and parameters of long-range side-chain interaction potentials from protein crystal data," *Journal of Computational Chemistry*, vol. 18, no. 7, pp. 849–873, 1997.
- [20] A. Liwo, M. R. Pincus, R. J. Wawak, S. Rackovsky, S. Oldziej, and H. A. Scheraga, "A united-residue force field for off-lattice protein-structure simulations. II. Parameterization of short-range interactions and determination of weights of energy terms by Z-score optimization," *Journal of Computational Chemistry*, vol. 18, no. 7, pp. 874–887, 1997.
- [21] A. Liwo, R. Kazmierkiewicz, C. Czaplowski et al., "United-residue force field for off-lattice protein-structure simulations: III. Origin of backbone hydrogen-bonding cooperativity in united-residue potentials," *Journal of Computational Chemistry*, vol. 19, no. 3, pp. 259–276, 1998.
- [22] A. Liwo, C. Czaplowski, J. Pillardy, and H. A. Scheraga, "Cumulant-based expressions for the multibody terms for the correlation between local and electrostatic interactions in the united-residue force field," *Journal of Chemical Physics*, vol. 115, no. 5, pp. 2323–2347, 2001.
- [23] A. V. Rojas, A. Liwo, and H. A. Scheraga, "Molecular dynamics with the united-residue force field: Ab initio folding simulations of multichain proteins," *Journal of Physical Chemistry B*, vol. 111, no. 1, pp. 293–309, 2007.
- [24] S. J. Marrink, H. J. Risselada, S. Yefimov, D. P. Tieleman, and A. H. De Vries, "The MARTINI force field: coarse grained model for biomolecular simulations," *Journal of Physical Chemistry B*, vol. 111, no. 27, pp. 7812–7824, 2007.
- [25] L. Monticelli, S. K. Kandasamy, X. Periole, R. G. Larson, D. P. Tieleman, and S. Marrink, "The MARTINI coarse-grained force field: extension to proteins," *Journal of Chemical Theory and Computation*, vol. 4, no. 5, pp. 819–834, 2008.
- [26] A. Rojas, A. Liwo, D. Browne, and H. A. Scheraga, "Mechanism of fiber assembly: treatment of A $\beta$  peptide aggregation with a coarse-grained united-residue force field," *Journal of Molecular Biology*, vol. 404, no. 3, pp. 537–552, 2010.
- [27] M. Iwaoka, D. Yosida, and N. Kimura, "Importance of the single amino acid potential in water for secondary and tertiary structures of proteins," *Journal of Physical Chemistry B*, vol. 110, no. 29, pp. 14475–14482, 2006.
- [28] M. Iwaoka, M. Okada, and S. Tomoda, "Solvent effects on the  $\varphi$ - $\psi$  potential surfaces of glycine and alanine dipeptides studied by PCM and I-PCM methods," *Journal of Molecular Structure: THEOCHEM*, vol. 586, pp. 111–124, 2002.
- [29] L. J. Smith, K. M. Fiebig, H. Schwalbe, and C. M. Dobson, "The concept of a random coil : residual structure in peptides and denatured proteins," *Folding and Design*, vol. 1, no. 5, pp. R95–R106, 1996.
- [30] K. M. Fiebig, H. Schwalbe, M. Buck, L. J. Smith, and C. M. Dobson, "Toward a description of the conformations of denatured states of proteins. Comparison of a random coil model with NMR measurements," *Journal of Physical Chemistry*, vol. 100, no. 7, pp. 2661–2666, 1996.

- [31] Y. Sakae and Y. Okamoto, "Optimization of protein force-field parameters with the Protein Data Bank," *Chemical Physics Letters*, vol. 382, no. 5-6, pp. 626-636, 2003.
- [32] N. Kamiya, Y. S. Watanabe, S. Ono, and J. Higo, "AMBER-based hybrid force field for conformational sampling of polypeptides," *Chemical Physics Letters*, vol. 401, no. 1-3, pp. 312-317, 2005.
- [33] M. Iwaoka and S. Tomoda, "The SAAP force field. A simple approach to a new all-atom protein force field by using Single Amino Acid Potential (SAAP) functions in various solvents," *Journal of Computational Chemistry*, vol. 24, no. 10, pp. 1192-1200, 2003.
- [34] M. Iwaoka, N. Kimura, D. Yosida, and T. Minezaki, "The SAAP force field: development of the single amino acid potentials for 20 proteinogenic amino acids and monte carlo molecular simulation for short peptides," *Journal of Computational Chemistry*, vol. 30, no. 13, pp. 2039-2055, 2009.
- [35] G. D. Hawkins, C. J. Cramer, and D. G. Truhlar, "Parametrized models of aqueous free energies of solvation based on pairwise descreening of solute atomic charges from a dielectric medium," *Journal of Physical Chemistry*, vol. 100, no. 51, pp. 19824-19839, 1996.
- [36] G. D. Hawkins, C. J. Cramer, and D. G. Truhlar, "Pairwise solute descreening of solute charges from a dielectric medium," *Chemical Physics Letters*, vol. 246, no. 1-2, pp. 122-129, 1995.
- [37] V. Tsui and D. A. Case, "Theory and applications of the generalized Born solvation model in macromolecular simulations," *Biopolymers*, vol. 56, no. 4, pp. 275-291, 2001.
- [38] W. H. Graham, E. S. Carter II., and R. P. Hicks, "Conformational analysis of Met-enkephalin in both aqueous solution and in the presence of sodium dodecyl sulfate micelles using multidimensional NMR and molecular modeling," *Biopolymers*, vol. 32, no. 12, pp. 1755-1764, 1992.
- [39] A. Mitsutake, M. Kinoshita, Y. Okamoto, and F. Hirata, "Combination of the replica-exchange Monte Carlo method and the reference interaction site model theory for simulating a peptide molecule in aqueous solution," *Journal of Physical Chemistry B*, vol. 108, no. 49, pp. 19002-19012, 2004.
- [40] A. Mitsutake, M. Kinoshita, Y. Okamoto, and F. Hirata, "Multicanonical algorithm combined with the RISM theory for simulating peptides in aqueous solution," *Chemical Physics Letters*, vol. 329, no. 3-4, pp. 295-303, 2000.
- [41] M. Kinoshita, Y. Okamoto, and F. Hirata, "First-principle determination of peptide conformations in solvents: combination of Monte Carlo simulated annealing and RISM theory," *Journal of the American Chemical Society*, vol. 120, no. 8, pp. 1855-1863, 1998.
- [42] M. Kinoshita, Y. Okamoto, and F. Hirata, "Solvation structure and stability of peptides in aqueous solutions analyzed by the reference interaction site model theory," *Journal of Chemical Physics*, vol. 107, no. 5, pp. 1586-1599, 1997.
- [43] L. Ramya and N. Gautham, "Effects of hydration on the conformational energy landscape of the pentapeptide Met-enkephalin," *Journal of Chemical Theory and Computation*, vol. 5, no. 8, pp. 2180-2190, 2009.
- [44] K. Y. Sanbonmatsu and A. E. García, "Structure of Met-enkephalin in explicit aqueous solution using replica exchange molecular dynamics," *Proteins: Structure, Function and Genetics*, vol. 46, no. 2, pp. 225-234, 2002.
- [45] D. Van Der Spoel and H. J. C. Berendsen, "Molecular dynamics simulations of leu-enkephalin in water and DMSO," *Biophysical Journal*, vol. 72, no. 5, pp. 2032-2041, 1997.
- [46] L. Zhan, J. Z. Y. Chen, and W. Liu, "Comparison of predicted native structures of met-enkephalin based on various accessible-surface-area solvent models," *Journal of Computational Chemistry*, vol. 30, no. 7, pp. 1051-1058, 2009.
- [47] L. Su and R. I. Cukier, "Hamiltonian and distance replica exchange method studies of met-enkephalin," *Journal of Physical Chemistry B*, vol. 111, no. 42, pp. 12310-12321, 2007.
- [48] D. A. Evans and D. J. Wales, "The free energy landscape and dynamics of met-enkephalin," *Journal of Chemical Physics*, vol. 119, no. 18, pp. 9947-9955, 2003.
- [49] M. M. Palian, Boguslavsky, D. F. O'Brien, and R. Polt, "Glycopeptide-membrane interactions: glycosyl enkephalin analogues adopt turn conformations by NMR and CD in amphipathic media," *Journal of the American Chemical Society*, vol. 125, no. 19, pp. 5823-5831, 2003.
- [50] B. A. Berg and H. Hsu, "Metropolis simulations of Met-Enkephalin with solvent-accessible area parametrizations," *Physical Review E*, vol. 69, no. 2, Article ID 026703, 9 pages, 2004.
- [51] K. Vengadesan and N. Gautham, "Energy landscape of Met-enkephalin and Leu-enkephalin drawn using mutually orthogonal Latin squares sampling," *Journal of Physical Chemistry B*, vol. 108, no. 30, pp. 11196-11205, 2004.
- [52] S. G. Itoh and Y. Okamoto, "Effective sampling in the configurational space of a small peptide by the multicanonical-multioverlap algorithm," *Physical Review E*, vol. 76, no. 2, Article ID 026705, 2007.
- [53] A. Mitsutake, U. H. E. Hansmann, and Y. Okamoto, "Temperature dependence of distributions of conformations of a small peptide," *Journal of Molecular Graphics and Modelling*, vol. 16, no. 4-6, pp. 226-238, 1998.
- [54] S. Honda, K. Yamasaki, Y. Sawada, and H. Morii, "10 Residue folded peptide designed by segment statistics," *Structure*, vol. 12, no. 8, pp. 1507-1518, 2004.
- [55] D. Satoh, K. Shimizu, S. Nakamura, and T. Terada, "Folding free-energy landscape of a 10-residue mini-protein, chignolin," *FEBS Letters*, vol. 580, no. 14, pp. 3422-3426, 2006.
- [56] T. Terada, D. Satoh, T. Mikawa, Y. Ito, and K. Shimizu, "Understanding the roles of amino acid residues in tertiary structure formation of chignolin by using molecular dynamics simulation," *Proteins: Structure, Function and Genetics*, vol. 73, no. 3, pp. 621-631, 2008.
- [57] D. Van Der Spoel and M. M. Seibert, "Protein folding kinetics and thermodynamics from atomistic simulations," *Physical Review Letters*, vol. 96, no. 23, Article ID 238102, 2006.
- [58] M. M. Seibert, A. Patriksson, B. Hess, and D. Van Der Spoel, "Reproducible polypeptide folding and structure prediction using molecular dynamics simulations," *Journal of Molecular Biology*, vol. 354, no. 1, pp. 173-183, 2005.
- [59] W. Xu, T. Lai, Y. Yang, and Y. Mu, "Reversible folding simulation by hybrid Hamiltonian replica exchange," *Journal of Chemical Physics*, vol. 128, no. 17, Article ID 175105, 2008.
- [60] S. Kannan and M. Zacharias, "Enhanced sampling of peptide and protein conformations using replica exchange simulations with a peptide backbone biasing-potential," *Proteins: Structure, Function and Genetics*, vol. 66, no. 3, pp. 697-706, 2007.
- [61] X. Dou and J. Wang, "Folding free energy landscape of the decapeptide chignolin," *Modern Physics Letters B*, vol. 22, no. 31, pp. 3087-3098, 2008.
- [62] A. Suenaga, T. Narumi, N. Futatsugi et al., "Folding dynamics of 10-residue beta-hairpin peptide chignolin," *Chemistry*, vol. 2, no. 5, pp. 591-598, 2007.

- [63] S. Roy, S. Goedecker, M. J. Field, and E. Penev, "A minima hopping study of all-atom protein folding and structure prediction," *Journal of Physical Chemistry B*, vol. 113, no. 20, pp. 7315–7321, 2009.
- [64] K. Moritsugu, T. Terada, and A. Kidera, "Scalable free energy calculation of proteins via multiscale essential sampling," *Journal of Chemical Physics*, vol. 133, no. 22, Article ID 224105, 2010.
- [65] B. Mennucci, E. Cancès, and J. Tomasi, "Evaluation of solvent effects in isotropic and anisotropic dielectrics and in ionic solutions with a unified integral equation method: theoretical bases, computational implementation, and numerical applications," *Journal of Physical Chemistry B*, vol. 101, no. 49, pp. 10506–10517, 1997.
- [66] E. Cancès, B. Mennucci, and J. Tomasi, "A new integral equation formalism for the polarizable continuum model: theoretical background and applications to isotropic and anisotropic dielectrics," *Journal of Chemical Physics*, vol. 107, no. 8, pp. 3032–3041, 1997.
- [67] G. Scalmani and M. J. Frisch, "Continuous surface charge polarizable continuum models of solvation. I. General formalism," *Journal of Chemical Physics*, vol. 132, no. 11, Article ID 114110, 2010.
- [68] M. J. Frisch, G. W. Trucks, H. B. Schlegel et al., *Gaussian 03, Revision C.02*, Gaussian, Wallingford, UK, 2004.
- [69] Y. K. Kang, "Ab initio and DFT conformational study of proline dipeptide," *Journal of Molecular Structure: THEOCHEM*, vol. 675, no. 1–3, pp. 37–45, 2004.
- [70] M. Makowski, J. Makowska, and L. Chmurzyński, "Ab initio study of the energetics of protonation, deprotonation and homocomplexed cations and anions formation in systems modeling side chains of biomolecules," *Journal of Molecular Structure: THEOCHEM*, vol. 674, no. 1–3, pp. 61–67, 2004.
- [71] B. H. Besler, K. M. Merz Jr., and P. A. Kollman, "Atomic charges derived from semiempirical methods," *Journal of Computational Chemistry*, vol. 11, no. 4, pp. 431–439, 1990.
- [72] V. V. Kostjukov, N. M. Khomytova, A. A. H. Santiago, R. L. Ibarra, D. B. Davies, and M. P. Evstigneev, "Calculation of the electrostatic charges and energies for intercalation of aromatic drug molecules with DNA," *International Journal of Quantum Chemistry*, vol. 111, no. 3, pp. 711–721, 2011.
- [73] D. A. Case, T. A. Darden, T. E. Cheatham III et al., *AMBER 10*, University of California, San Francisco, Calif, USA, 2008.
- [74] N. Metropolis, A. W. Rosenbluth, M. N. Rosenbluth, A. H. Teller, and E. Teller, "Equation of state calculations by fast computing machines," *The Journal of Chemical Physics*, vol. 21, no. 6, pp. 1087–1092, 1953.
- [75] K. Binder, "Applications of Monte Carlo methods to statistical physics," *Reports on Progress in Physics*, vol. 60, no. 5, pp. 487–559, 1997.
- [76] M. Matsumoto and T. Nishimura, "Mersenne Twister: a 623-dimensionally equidistributed uniform pseudo-random number generator," *ACM Transactions on Modeling and Computer Simulation*, vol. 8, no. 1, pp. 3–30, 1998.
- [77] I. Marcotte, F. Separovic, M. Auger, and S. M. Gagné, "A multidimensional  $^1\text{H}$  NMR investigation of the conformation of methionine-enkephalin in fast-tumbling bicelles," *Biophysical Journal*, vol. 86, no. 3, pp. 1587–1600, 2004.
- [78] A. W. Götz, M. J. Williamson, D. Xu, D. Poole, S. La Grand, and R. C. Walker, "Routine microsecond molecular dynamics simulations with AMBER on GPUs. 1. Generalized Born," *Journal of Chemical Theory and Computation*, vol. 8, no. 5, pp. 1542–1555, 2012.
- [79] J. Shao, S. W. Tanner, N. Thompson, and T. E. Cheatham III., "Clustering molecular dynamics trajectories: I. Characterizing the performance of different clustering algorithms," *Journal of Chemical Theory and Computation*, vol. 3, no. 6, pp. 2312–2334, 2007.
- [80] H. A. Scheraga, M. Khalili, and A. Liwo, "Protein-folding dynamics: overview of molecular simulation techniques," *Annual Review of Physical Chemistry*, vol. 58, pp. 57–83, 2007.
- [81] Y. Sakae and Y. Okamoto, "Optimisation of OPLS-UA force-field parameters for protein systems using protein data bank," *Molecular Simulation*, vol. 36, no. 14, pp. 1148–1156, 2010.

## Research Article

# Influence of Pyrazine Ring Doping on the $^{15}\text{N}$ and $^{11}\text{B}$ NMR and Electronic Structure Parameters in Zigzag Boron Nitride Nanotube: A DFT Study

Sattar Arshadi, Ameneh Asghari, Hojatollah Raheimi, and Saboora Abedini

Department of Chemistry, Payame Noor University, P.O. Box 19395-4697, Iran

Correspondence should be addressed to Sattar Arshadi; [chemistry\\_arshadi@yahoo.com](mailto:chemistry_arshadi@yahoo.com)

Received 24 June 2012; Accepted 18 November 2012

Academic Editor: André Silva Pimentel

Copyright © 2013 Sattar Arshadi et al. This is an open access article distributed under the Creative Commons Attribution License, which permits unrestricted use, distribution, and reproduction in any medium, provided the original work is properly cited.

Density functional theory (DFT) calculations have been performed to investigate the properties of the electronic structures of pyrazine-doped boron nitride nanotubes (PD-BNNTs). The structural forms were firstly optimized and then nuclear magnetic resonance (NMR) parameters have been calculated on the optimized structures. The chemical shielding isotropic ( $CS^I$ ) and chemical shielding anisotropic ( $CS^A$ ) parameters were calculated at the sites of  $^{11}\text{B}$  and  $^{15}\text{N}$  nuclei in structural forms of BNNT including the perfect (a) model and PD-BNNTs (b), (c), and (d) models. The results indicated that the changes are most significant for those nuclei placed in the nearest neighborhood of the pyrazine-doped ring. The changes of the electronic sites of the N atoms are also more significant than those of the B atoms. The difference of LUMO-HOMO gap for the perfect model was larger than the PD-BNNTs models. Also the atomic charge distribution of N and B atoms has been determined in nanotubes by natural bond orbital (NBO) analysis. All calculations were performed by the B3LYP method and 6-311G\*\* basis set using Gaussian 98 package of program.

## 1. Introduction

The existence of tubular forms of matter with nanoscale diameters has opened an exciting field of research in science. Since the discovery of carbon fullerene  $C_{60}$  by Smalley et al. in 1985 and carbon nanotubes by Iijima in 1991, electronic and mechanical properties of carbon and noncarbon nanotubes have been investigated by various groups [1–4].

Boron nitride (BN) is the first candidate to replace carbon, because hexagonal-BN structure is quite similar to that of graphite. Boron nitride nanotubes (BNNTs) have attracted an enormous amount of attention [5–13] as a typical representative of III–V compound tubes, partially because they have the morphology of honeycomb analogous to carbon nanotubes (CNTs). It has been shown that BNNTs exhibit many interesting properties such as significant resistance to oxidation at high temperatures when compared to the carbon nanotubes [14–19].

Unlike CNTs, all BN nanotubes exhibit semiconducting behavior with a wide band gap which is almost independent

of tubular diameter, chirality, and number of walls [6, 20]. Furthermore, in contrast to the nonpolar CNTs, slight positive charge of boron atom (B) and slight negative charge of nitrogen atom (N) increase the polarity and the ionicity of the BNNTs. Therefore, the BNNTs have been proposed as more proper materials than the CNTs for applications in the specific electronic and mechanical devices.

The structure of BNNTs was firstly predicted by theoretical calculations [7, 21]. In 1995, Chopra et al. [5] reported the production of multiwalled BNNTs using arc-discharge techniques. The other synthesis methods are laser-assisted technique [22, 23] using pyrolytically grown CNTs as templates to prepare BNNTs, using chemical vapor deposition (CVD) by Lourie et al. [24]. In 2001, Bengu and Marks proposed a new method to synthesize the single-walled BN nanotubes [25]. This new synthesis technique has made it possible to bring BN nanotubes into the nanotechnology applications.

Previous studies have indicated that the properties of the electronic structure of the BNNTs are influenced by

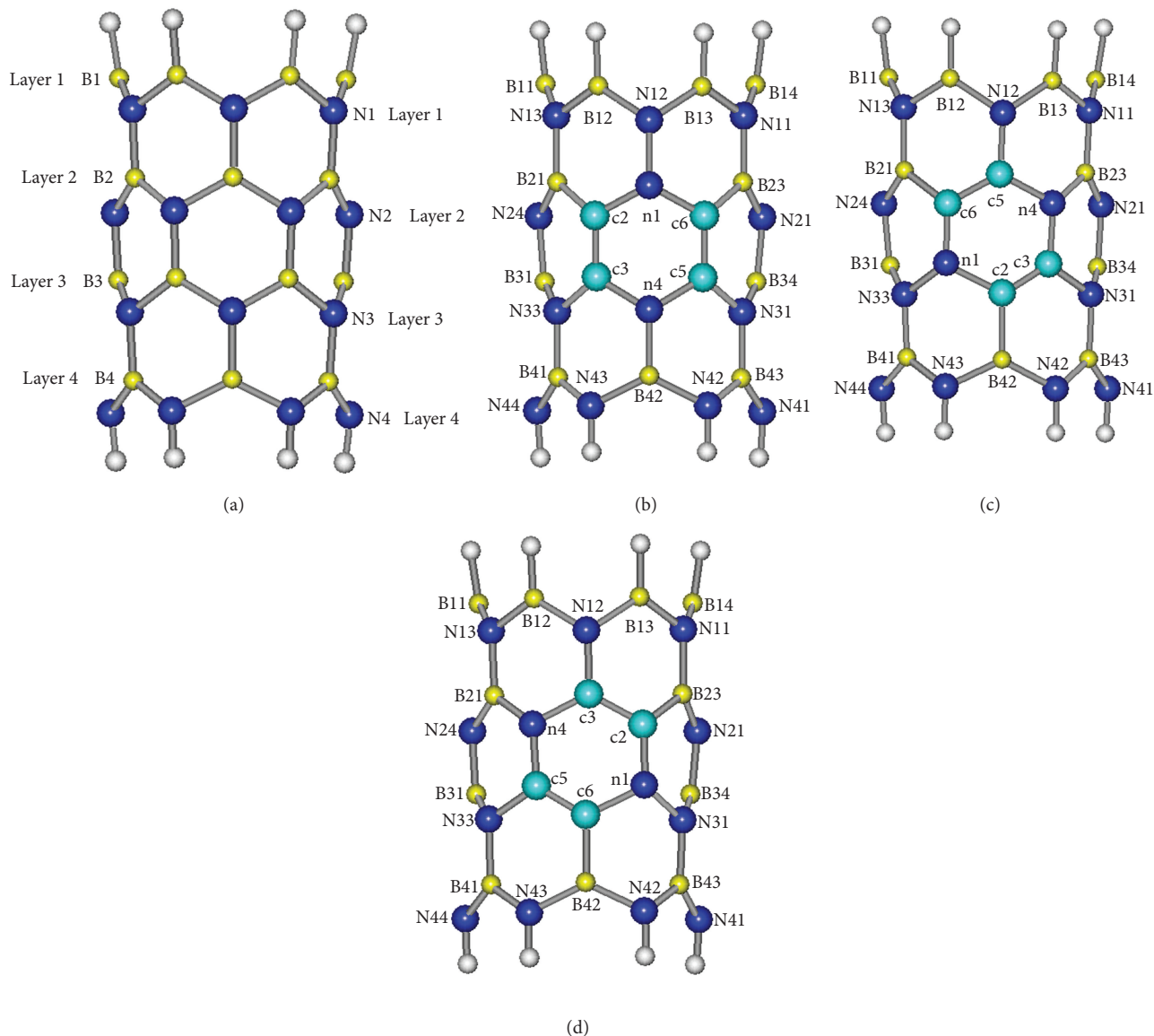


FIGURE 1: The front side view of perfect BNNTs model (a) and pyrazine-doped BNNTs models ((b)–(d)).

the doping atoms and impurities. Thus, uniformly doped BNNTs obtained through chemical modification could be very effective for tailoring the electronic properties, and the related mechanism and behavior are valuable to be explored in theory [26, 27].

Within present research, we have investigated the electronic structures and NMR parameters at the sites of  $^{11}\text{B}$  and  $^{15}\text{N}$  nuclei of perfect and pyrazine-doped models of BNNTs by density functional theory (DFT) calculations. Furthermore, we have investigated atomic charge distribution in nanotubes by natural bond orbital (NBO) [28] analysis.

## 2. Models and Computational Methods

Conveniently, BN nanotube could be presented by a  $(n, m)$  pair of numbers, where the  $(n, 0)$  and  $(n, n)$  BN nanotubes

designate the zigzag and armchair types, respectively. For the zigzag type BN nanotube,  $n$  denotes the number of triazines in the circumference of the tube and the translation axis is the tubular length.

We have considered four models: a perfect and three pyrazine-doped models in Figures 1(a)–1(d) of the representative (6,0) zigzag single-walled BNNTs in present study. Figure 1(a) shows the perfect model, which consists of 24 boron (B) atoms and 24 nitrogen (N) atoms where the two tips of the nanotube are saturated by 12 hydrogen (H) atoms. In the perfect zigzag BNNTs, three B and three N atoms in the center of nanotube have been replaced by four carbon atoms ( $\text{sp}^2$ -hybridized) and two N atoms to create the pyrazine-doped BNNTs (pyrazine-BNNTs). Figures 1(b)–1(d) show three doped models which have different position for pyrazine ring in corresponding models.

TABLE 1: Structural energies,  $E_{\text{LUMO}}$ ,  $E_{\text{HOMO}}$ , LUMO-HOMO gap, dipole moments and electronegativity for the perfect model (a) and PD-BNNT models ((b), (c), and (d)) at B3LYP/6-311G\*\* level.

Models	Energy (keV)	$E_{\text{LUMO}}$ (eV)	$E_{\text{HOMO}}$ (eV)	$\Delta_{(\text{LUMO-HOMO})}$ (eV)	Dipole moment (Debye)	Electronegativity ( $\chi$ )
Perfect (a)	-52.22	-1.99	-6.85	4.86	7.47	4.42
(b)	-52.85	-1.86	-4.89	3.03	8.27	3.37
(c)	-52.85	-2.13	-4.70	2.57	6.93	3.41
(d)	-52.85	-2.13	-4.70	2.57	6.93	3.41

In the first step, the structures have been allowed to relax by all atomic geometrical optimization at the DFT level with B3LYP exchange-functional method and 6-311G\*\* basis set. Furthermore NBO analysis was carried out on the B3LYP/6-311G\*\* wave functions using version 3.1 of NBO package [29] included in Gaussian 98 program package [30].

Also we investigated electronegativity ( $\chi$ ) in the optimized structures. As we already know, electronegativities may be considered as the power of an atom in a given molecule to attract electrons to itself [31]. For an N-electron system with potential acting on an electron at  $r$  due to the nuclear attraction plus such other external forces as may be present (external potential)  $v(r)$  and total energy  $E$ , electronegativity ( $\chi$ ) [32] is defined as the following:

$$\chi = -\left(\frac{\partial E}{\partial N}\right)_{v(r),T}. \quad (1)$$

The electronegativity is defined as the half part of the difference between the HOMO and the LUMO energies as follows:

$$\chi = \frac{-(E_{\text{HOMO}} + E_{\text{LUMO}})}{2}. \quad (2)$$

The CS tensors are calculated for optimized nanotubes at the DFT level employing the B3LYP method and 6-311G\*\* basis set based on the gauge independent atomic orbital (GIAO) approach [33]. The calculated CS tensors at the sites of  $^{11}\text{B}$  and  $^{15}\text{N}$  are yielded in the principal axes system (PAS)  $\sigma_{33} > \sigma_{22} > \sigma_{11}$  [34]. Thereafter, they are converted to isotropic chemical shielding ( $\text{CS}^{\text{I}}$ ) and anisotropic chemical shielding ( $\text{CS}^{\text{A}}$ ) parameters using (3) [35] and are showed in Tables 5, 6, and 7:

$$\begin{aligned} \text{CS}^{\text{I}} \text{ (ppm)} &= \frac{(\sigma_{11} + \sigma_{22} + \sigma_{33})}{3}, \\ \text{CS}^{\text{A}} \text{ (ppm)} &= \frac{\sigma_{33} - (\sigma_{11} + \sigma_{22})}{2}. \end{aligned} \quad (3)$$

The DFT calculations have been performed by the Gaussian 98 package.

### 3. Results and Discussion

**3.1. The Optimized Parameters.** At the first step of this task, structural optimization was successfully carried out for the perfect ((a) model) and doped models ((b), (c), and (d) models) of the single-wall (6, 0) BNNT at the level of B3LYP, DFT method and 6-311G\*\* basis set.

Subsequently, frequency calculations (keyword: FREQ = NORAMAN) were carried out by standard techniques on the optimized structures. For minimum state species, only real frequency values (with a positive sign) are accepted.

Table 1 presents the results for structural energies, the highest occupied molecular orbital (HOMO), the lowest unoccupied molecular orbital (LUMO), LUMO-HOMO gaps, dipole moments, and electronegativity ( $\chi$ ) obtained by the DFT calculations.

Our results indicated that the values of LUMO-HOMO gaps of the PD-BNNTs models are smaller than the perfect model. Also among the values of the LUMO-HOMO gaps of the pyrazine-doped models, the most significant changes were observed for the c and d models.

As we know, the band gap for the BN nanotube is higher in energy than the CNTs [6]. On the other hand, pyrazine-doped BN nanotube has similarities to CNTs in view of the presence of carbons in the nanotube wall. Therefore the band gap in pyrazine-doped BN nanotube is similar to CNTs to some extent. This is proved by the calculated energies which are shown in Table 1.

The LUMO-HOMO gap is 4.86 eV for perfect model, 3.03 eV for (b) model, and 2.57 eV for (c) and (d) models, respectively (Table 1).

Also the densities of states (DOSs) of perfect and pyrazine-doped BNNT are shown in Figure 2 for better understanding the effect of pyrazine ring doping on the electronic structure of BNNT. It is clear that, after doping of pyrazine ring, the HOMO-LUMO energy gap of tube has significant change. On the other hand, the doping of pyrazine ring decreases the HOMO-LUMO energy gaps of the perfect BNNT.

The HOMO and LUMO in the perfect and pyrazine-doped models are plotted in Figure 3. For the perfect model, the HOMO is located on the nitrogen atoms of the (6, 0) zigzag BNNT model and corresponds to the lone pair of electron on nitrogen atoms. In contrast, the LUMO is uniformly distributed throughout the B-N bonds. For the pyrazine-doped models, the majority of the HOMO and LUMO are located at the pyrazine-doped regions.

The circumferences of the armchair BNNTs include both N and B atoms in both ends. In contrast to armchair models, circumferences of the zigzag BNNTs consist of one-type atoms, either N or B atoms; if one of the ends is formed by N atoms, the other end is formed by B atoms. The B atoms are slightly positive and the N atoms are slightly negative; therefore, the zigzag BNNT is a polar material that could be better seen by the value of dipole moment. Comparing the values of the dipole moments for the four models indicates

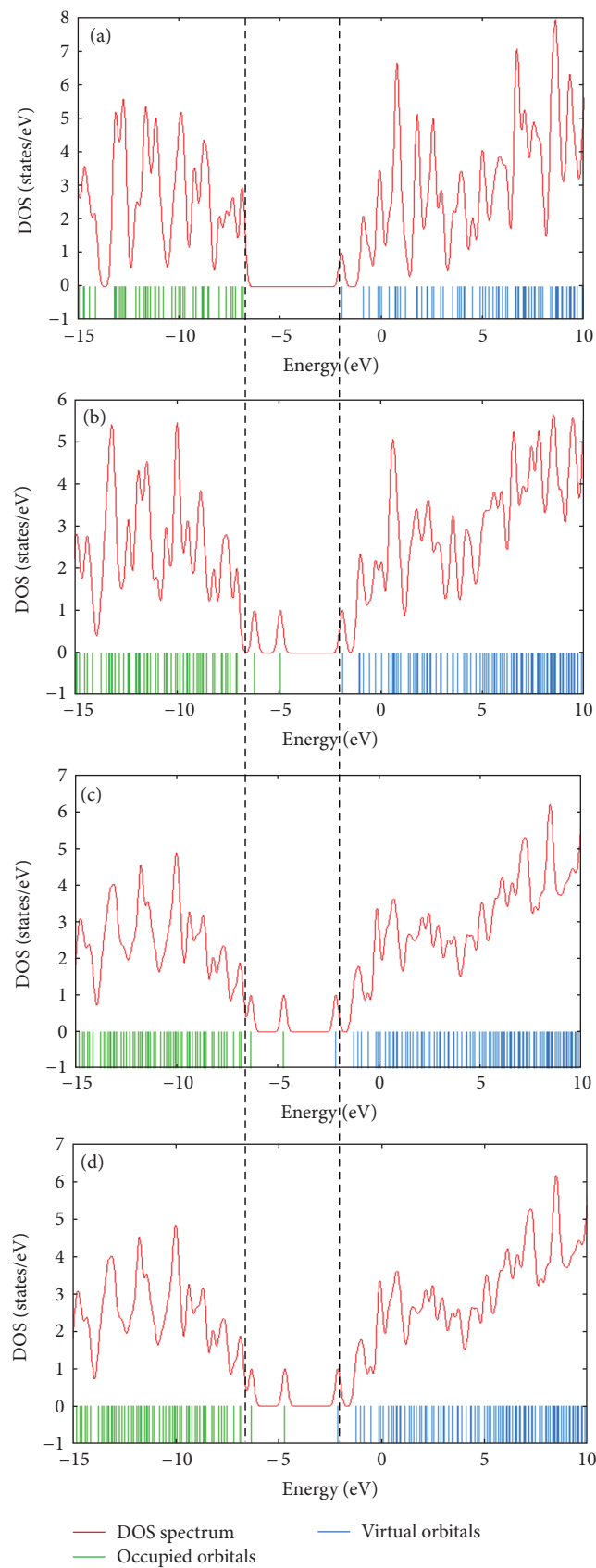


FIGURE 2: The density of states (DOS) of (a) the perfect model and (b), (c), and (d) pyrazine-doped models.

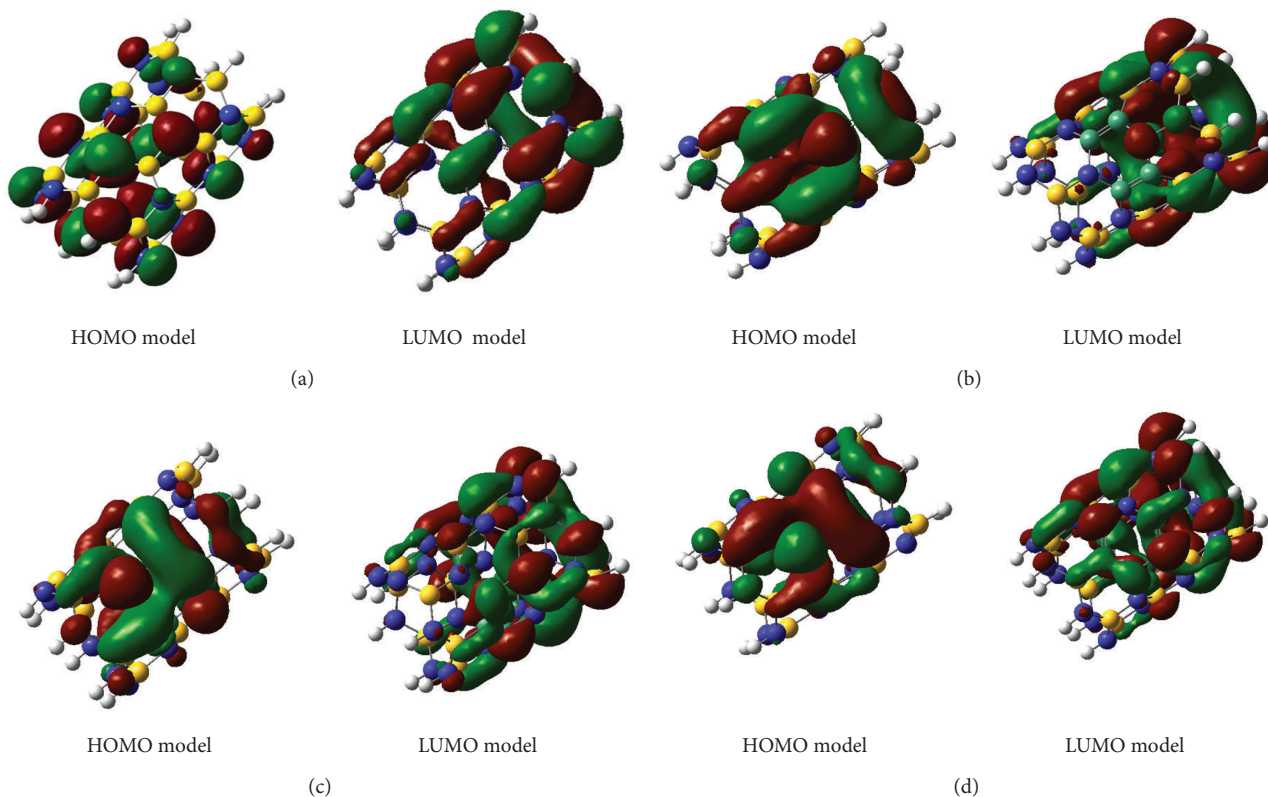


FIGURE 3: HOMO and LUMO orbitals for different models of the BNNTs: (a) perfect model, (b), (c), and (d) pyrazine-doped models.

TABLE 2: Optimized bond lengths (Å) and bond angles (°) for the perfect (in bracket) and PD-BNNT models (b) at B3LYP/6-311G\*\* level.

Bonds	Length (Å)	Bonds	Length (Å)	Bonds	Length (Å)	Bonds	Angle (°)	Bonds	Angle (°)
B41-N44	1.45 [1.45]	B42-n4	1.44 [1.45]	B43-N41	1.45 [1.45]	c2-n1-c6	113 [118]	B23-c6-c5	119 [118]
B41-N33	1.45 [1.45]	B42-N42	1.45 [1.45]	c5-N31	1.42 [1.46]	c3-c2-n1	117 [118]	c5-N31-B43	119 [118]
B41-N43	1.45 [1.45]	c3-n4	1.43 [1.46]	B34-N31	1.46 [1.46]	c2-c3-n4	120 [120]	c3-n4-B42	119 [118]
B31-N33	1.46 [1.46]	c5-n4	1.43 [1.46]	c5-c6	1.35 [1.45]	c3-n4-c5	109 [111]	c5-n4-B42	119 [118]
c3-N33	1.42 [1.46]	c2-c3	1.35 [1.45]	c6-B23	1.54 [1.46]	n4-c5-c6	120 [120]	B41-N33-c3	119 [118]
B31-N24	1.44 [1.46]	c2-n1	1.44 [1.46]	B23-N11	1.43 [1.45]	c5-c6-n1	117 [118]	c3-N33-B31	115 [111]
B21-N24	1.45 [1.45]	n1-N12	1.42 [1.45]	B23-N21	1.45 [1.45]	B23-c6-n1	116 [110]	c5-N31-B34	115 [111]
B21-N13	1.43 [1.45]	C6-n1	1.44 [1.46]	B13-N11	1.46 [1.46]	B21-c2-n1	116 [110]	N24-B21-c2	117 [118]
c2-B21	1.54 [1.45]	B12-N12	1.46 [1.46]	B14-N11	1.46 [1.46]	B21-c2-c3	119 [118]	c6-B23-N21	117 [118]
B11-N13	1.46 [1.46]	B13-N12	1.46 [1.46]	B34-N21	1.44 [1.46]	n4-c5-N31	116 [118]	c6-B23-N11	119 [120]
B12-N13	1.46 [1.46]	B43-N42	1.45 [1.45]	B14-N16	1.46 [1.46]	N33-c3-n4	116 [118]	c2-B21-N13	119 [120]
B42-N43	1.45 [1.45]	B43-N31	1.45 [1.45]	B15-N16	1.46 [1.46]	c6-c5-N31	121 [120]	c2-c3-N33	121 [120]

that the value for the (b) model is significantly increased ( $D = 8.27$  Debye) whereas those for the (c) and (d) models are significantly reduced ( $D = 6.93$  Debye) compared with the perfect (a) model ( $D = 7.47$  Debye), which means that the strengths of the charge points are balanced in the two latter models (Table 1).

The calculated structural energies in Table 1 also indicate no difference between the three models of the PD-BNNTs ( $-52.85$  keV). On the other hand, the (c) and (d) models are structural isomers of the (b) model.

Tables 2, 3, and 4 present the optimized parameters including the bond lengths and bond angle for four models of the investigated (6, 0) BNNT (Figures 1(a)–1(d)).

In the perfect BNNT (Figure 1(a)), the average B–N bond length was 1.45–1.46 Å, but this value also was changed by the pyrazine-doping in the PD-BNNT due to existence of B–C, C–N, N–N, and C=C bonds in addition to B–N one.

However, the effects of this deformation were significant just at the geometrical properties of the nearest atoms to the pyrazine-doped ring whereas those of other atoms almost

TABLE 3: Optimized bond lengths (Å) and bond angles (°) for the perfect (in bracket) and PD-BNNT models (c) at B3LYP/6-311G\*\* level.

Bonds	Length (Å)	Bonds	Length (Å)	Bonds	Length (Å)	Bonds	Angle (°)	Bonds	Angle (°)
B41-N44	1.46 [1.45]	c2-B42	1.52 [1.45]	B43-N41	1.46 [1.45]	c6-c5-n4	121 [118]	B23-n4-c3	119 [118]
B41-N33	1.44 [1.45]	B42-N42	1.45 [1.45]	c3-N31	1.42 [1.46]	n1-c6-c5	121 [118]	c3-N31-B43	118 [118]
B41-N43	1.46 [1.45]	n1-c2	1.47 [1.46]	B34-N31	1.48 [1.46]	c6-n1-c2	115 [120]	n1-c2-B42	117 [118]
B31-N33	1.46 [1.46]	c2-c3	1.36 [1.46]	c3-n4	1.40 [1.45]	n1-c2-c3	120 [111]	c3-c2-B42	121 [118]
n1-N33	1.49 [1.46]	c6-n1	1.40 [1.45]	n4-B23	1.46 [1.46]	c2-c3-n4	122 [120]	B41-N33-n1	115 [118]
B31-N24	1.44 [1.46]	c5-c6	1.38 [1.46]	B23-N11	1.43 [1.45]	c3-n4-c5	115 [118]	n1-N33-B31	117 [111]
B21-N24	1.46 [1.45]	c5-N12	1.41 [1.45]	B23-N21	1.44 [1.45]	B23-n4-c5	114 [110]	c3-N31-B34	110 [111]
B21-N13	1.45 [1.45]	c5-n4	1.44 [1.46]	B13-N11	1.45 [1.46]	B21-c6-c5	107 [110]	N24-B21-c6	115 [118]
c6-B21	1.53 [1.45]	B12-N12	1.47 [1.46]	B14-N11	1.46 [1.46]	B21-c6-n1	123 [118]	n4-B23-N21	108 [118]
B11-N13	1.46 [1.46]	B13-N12	1.45 [1.46]	B34-N21	1.44 [1.46]	c2-c3-N31	120 [118]	n4-B23-N11	119 [120]
B12-N13	1.44 [1.46]	B43-N42	1.44 [1.45]	B14-N16	1.45 [1.46]	N33-n1-c2	106 [118]	c6-B21-N13	120 [120]
B42-N43	1.45 [1.45]	B43-N31	1.47 [1.45]	B15-N16	1.46 [1.46]	n4-c3-N31	118 [120]	c6-n1-N33	114 [120]

TABLE 4: Optimized bond lengths (Å) and bond angles (°) for the perfect (in bracket) and PD-BNNT models (d) at B3LYP/6-311G\*\* level.

Bonds	Length (Å)	Bonds	Length (Å)	Bonds	Length (Å)	Bonds	Angle (°)	Bonds	Angle (°)
B41-N44	1.46 [1.45]	c6-B42	1.52 [1.45]	B43-N41	1.46 [1.45]	n4-c3-c2	121 [118]	B23-c2-n1	123 [118]
B41-N33	1.47 [1.45]	B42-N42	1.45 [1.45]	n1-N31	1.49 [1.46]	c5-n4-c3	115 [118]	n1-N31-B43	115 [118]
B41-N43	1.44 [1.45]	c5-C6	1.36 [1.46]	B34-N31	1.46 [1.46]	n4-c5-c6	122 [120]	c5-c6-B42	121 [118]
B31-N33	1.48 [1.46]	c6-N1	1.47 [1.46]	n1-c6	1.47 [1.45]	c5-c6-n1	120 [111]	n1-c6-B42	117 [118]
c5-N33	1.42 [1.46]	c5-n4	1.40 [1.45]	c2-B23	1.53 [1.46]	c6-n1-c2	115 [120]	B41-N33-c5	117 [118]
B31-N24	1.44 [1.46]	c3-n4	1.44 [1.46]	B23-N11	1.45 [1.45]	n1-c2-c3	121 [118]	c5-N33-B31	110 [111]
B21-N24	1.44 [1.45]	c3-N12	1.41 [1.45]	B23-N21	1.46 [1.45]	B23-c2-c3	107 [110]	n1-N31-B34	117 [111]
B21-N13	1.43 [1.45]	c2-c3	1.38 [1.46]	B13-N11	1.44 [1.46]	B21-n4-c3	114 [110]	N24-B21-n4	118 [118]
n4-B21	1.46 [1.45]	B12-N12	1.45 [1.46]	B14-N11	1.46 [1.46]	B21-n4-c5	119 [118]	c2-B23-N21	115 [118]
B11-N13	1.46 [1.46]	B13-N12	1.47 [1.46]	B34-N21	1.44 [1.46]	c6-n1-N31	106 [118]	c2-B23-N11	120 [120]
B12-N13	1.45 [1.46]	B43-N42	1.46 [1.45]	B14-N16	1.46 [1.46]	N33-c5-c6	120 [118]	n4-B21-N13	119 [120]
B42-N43	1.45 [1.45]	B43-N31	1.44 [1.45]	B15-N16	1.45 [1.46]	c2-n1-N31	114 [120]	n4-c5-N33	118 [120]

remained unchanged. Furthermore, the changes of the bond angles were more than those of the bond lengths in the zigzag PD-BNNT.

Among theoretical methods, natural bond orbital (NBO) analysis is a unique approach to the evaluation of the atomic charges. It is clear that the charges of N and B atoms in these structures are negative and positive, respectively. The charges of N and B atoms at the end of tubes are smaller than those of other ones. Moreover, the results of NBO analysis indicated that the atomic charge distribution in the pyrazine-doped models is different from the perfect model.

**3.2. NMR Parameters.** In this computational work, the CS tensors ( $CS^I$  and  $CS^A$ ) for various  $^{11}B$  and  $^{15}N$  atoms are calculated to study the influence of pyrazine ring doping on the electronic structure properties of the (6, 0) BNNT.

In the following text, the calculated  $^{11}B$  and  $^{15}N$  NMR parameters for the perfect and the pyrazine-doped models of BNNT are discussed, respectively.

**3.2.1. The Perfect Model.** Tables 5, 6, and 7 present the calculated NMR parameters for various  $^{11}B$  and  $^{15}N$  nuclei in the perfect model of BNNT. This model includes 24 B and 24 N atoms, where the edges are saturated by 12 H atoms (Figure 1(a)).

A quick look at the results reveals that various  $^{11}B$  and  $^{15}N$  nuclei are divided into four layers along the nanotube length. The layers have equivalent calculated  $CS^I$  and  $CS^A$  parameters, which means that the nuclei in each layer have equivalent electrostatic properties around similar nuclei.

The nature of the valence shells of the N atoms, which have lone pair of electrons, and the B atoms, which have a lack of electrons, is different; therefore, different behavior of the CS properties is expected and is also observed for these atoms.

The values of NMR properties for the  $^{11}B$  and  $^{15}N$  nuclei of the perfect model indicate that the B-mouth (B1) has the smallest value of  $CS^I$  ( $^{11}B$ ), 64 ppm, and the N-mouth (N4) has the largest value of  $CS^I$  ( $^{15}N$ ), 148 ppm, among the other layers of nuclei.

TABLE 5: The B3LYP/6-311G\*\* calculated NMR parameters of the perfect model and model (b) of PD-BNNT.

Nuclei	CS <sup>I</sup> (ppm)		CS <sup>A</sup> (ppm)		Nuclei	CS <sup>I</sup> (ppm)		CS <sup>A</sup> (ppm)	
	Perfect	Doped	Perfect	Doped		Perfect	Doped	Perfect	Doped
Layer 1					Layer 1				
B1	64	—	60	—	N1	75	—	242	—
B11	—	65	—	59	N11	—	89	—	257
B12	—	74	—	54	N12	—	28	—	194
B13	—	74	—	54	N13	—	89	—	257
B14	—	65	—	59	N14	—	73	—	244
B15	—	64	—	60	N15	—	73	—	238
B16	—	64	—	60	N16	—	73	—	244
Layer 2					Layer 2				
B2	69	—	43	—	N2	111	—	195	—
B21	—	69	—	55	N21	—	105	—	209
B22	—	—	—	—	N22	—	—	—	—
B23	—	69	—	55	N23	—	—	—	—
B24	—	70	—	44	N24	—	105	—	209
B25	—	69	—	44	N25	—	110	—	195
B26	—	70	—	44	N26	—	110	—	195
Layer 3					Layer 3				
B3	69	—	39	—	N3	115	—	187	—
B31	—	68	—	40	N31	—	115	—	124
B32	—	—	—	—	N32	—	101	—	92
B33	—	—	—	—	N33	—	115	—	124
B34	—	68	—	40	N34	—	115	—	188
B35	—	70	—	38	N35	—	113	—	187
B36	—	70	—	38	N36	—	115	—	188
Layer 4					Layer 4				
B4	70	—	46	—	N4	148	—	94	—
B41	—	74	—	39	N41	—	153	—	86
B42	—	77	—	44	N42	—	163	—	74
B43	—	74	—	39	N43	—	163	—	74
B44	—	71	—	44	N44	—	153	—	86
B45	—	69	—	46	N45	—	147	—	98
B46	—	71	—	44	N46	—	147	—	98

In contrast, the opposite behavior is observed for the values of CS<sup>A</sup>: the B-mouth has the largest value of CS<sup>A</sup> (<sup>11</sup>B), 60 ppm, whereas the N-mouth has the smallest value of CS<sup>A</sup> (<sup>15</sup>N), 94 ppm, among the other layers of nuclei.

**3.2.2. The PD-BNNT Models.** In the doped models, three B and three N atoms are doped by four carbon atoms (sp<sup>2</sup>-hybridized) and two N atoms to construct PD- BNNTs ((b), (c) and (d)) models of Figure 1.

Due to this doping, the CS tensors at the sites of <sup>11</sup>B and <sup>15</sup>N nuclei which are directly bonded to the pyrazine ring undergo significant changes among the other nuclei in comparison with the perfect model. Furthermore, the magnitude of changes of the CS tensors is more significant at the sites of <sup>15</sup>N nuclei than at those of <sup>11</sup>B nuclei.

Although the other not directly bonded B and N layers are influenced by the pyrazine-doped ring, due to the sensitivity of the CS tensors, they also undergo some minor changes in the doped model. Moreover, the CS tensors at the sites of those nuclei shown in Figures 1(b)–1(d) (front side) change while those at the other side (back side) do not undergo any significant changes and their NMR parameters remain unchanged as those of the perfect model.

For example, in the (b) model (Figure 1(b)), NMR parameters of B42 (directly bonded) and B41, B43 (indirectly) were influenced by the pyrazine-doping whereas those of B44, B45, and B46 undergo some minor changes.

The evaluated NMR parameters at the sites of <sup>11</sup>B and <sup>15</sup>N nuclei in the perfect and doped models are presented in Tables 5, 6, and 7. In the (b) model of the zigzag PD-BNNT (Figure 1(b)), B32, B33, N22, and N23 atoms are

TABLE 6: The B3LYP/6-311G\*\* calculated NMR parameters of the perfect model and model (c) of PD-BNNT.

Nuclei	CS <sup>I</sup> (ppm)		CS <sup>A</sup> (ppm)		Nuclei	CS <sup>I</sup> (ppm)		CS <sup>A</sup> (ppm)	
	Perfect	Doped	Perfect	Doped		Perfect	Doped	Perfect	Doped
Layer 1					Layer 1				
B1	64	—	60	—	N1	75	—	242	—
B11	—	66	—	57	N11	—	88	—	241
B12	—	73	—	54	N12	—	59	—	224
B13	—	70	—	54	N13	—	76	—	263
B14	—	65	—	58	N14	—	75	—	245
B15	—	64	—	59	N15	—	74	—	243
B16	—	64	—	58	N16	—	74	—	242
Layer 2					Layer 2				
B2	69	—	43	—	N2	111	—	195	—
B21	—	75	—	49	N21	—	115	—	195
B22	—	—	—	—	N22	—	112	—	137
B23	—	74	—	42	N23	—	—	—	—
B24	—	68	—	45	N24	—	119	—	199
B25	—	69	—	43	N25	—	110	—	198
B26	—	70	—	44	N26	—	110	—	194
Layer 3					Layer 3				
B3	69	—	39	—	N3	115	—	187	—
B31	—	70	—	42	N31	—	114	—	136
B32	—	—	—	—	N32	—	—	—	—
B33	—	—	—	—	N33	—	64	—	97
B34	—	68	—	42	N34	—	113	—	182
B35	—	68	—	41	N35	—	115	—	188
B36	—	69	—	41	N36	—	113	—	184
Layer 4					Layer 4				
B4	70	—	46	—	N4	148	—	94	—
B41	—	74	—	44	N41	—	151	—	92
B42	—	70	—	57	N42	—	141	—	119
B43	—	70	—	47	N43	—	152	—	94
B44	—	70	—	45	N44	—	155	—	77
B45	—	70	—	45	N45	—	149	—	94
B46	—	70	—	45	N46	—	148	—	95

doped by the C atoms and B22 and N32 atoms are doped by the N atoms which yield B–C, C–N, N–N, and C=C bonds. The results indicated that the changes are most significant for those nuclei placed in the nearest neighborhood of the pyrazine-doped ring.

In the first layer, N12 has the smallest CS<sup>I</sup> and CS<sup>A</sup> values (28 and 194 ppm, resp.) among the remaining N atoms in this layer. Also the calculated results show that those N atoms (N41, N42, N43, and N44) have the largest CS<sup>I</sup> values (153, 163, 163, and 153 ppm) but the smallest CS<sup>A</sup> values (86, 74, 74, and 86 ppm) among all N atoms.

The changes in the values of the CS parameters for B12, B13, B41, B42, and B43 atoms are also notable (Table 5).

The doping of B22, B33, N23, and N32 atoms by the C atoms and the doping of B32 and N22 atoms by the N

atoms take place in the (c) model of the zigzag PD-BNNT (Figure 1(c)) which yield B–C, C–N, N–N, and C=C bonds.

Among the B atoms of the (c) model, B21, B23, and B42 are directly bonded to the pyrazine ring; hence, their NMR parameters (CS<sup>I</sup> or CS<sup>A</sup>) detect some changes due to the pyrazine-doping. Moreover, the NMR parameters of atoms further away show minor changes.

The CS<sup>I</sup> and CS<sup>A</sup> values for the N nuclei in the (c) model are different from those values in the (b) model. However notable changes in the CS tensors are observed for all of the N atoms due to the direct and indirect effect of the pyrazine-doped ring (Table 6).

In the (d) model (Figure 1(d)), B22, B32, N22, and N32 atoms are doped by the C atoms and B33 and N23 atoms are doped by the N atoms.

TABLE 7: The B3LYP/6-311G\*\* calculated NMR parameters of the perfect model and model (d) of PD-BNNT.

Nuclei	CS <sup>I</sup> (PPm)		CS <sup>A</sup> (PPm)		Nuclei	CS <sup>I</sup> (PPm)		CS <sup>A</sup> (PPm)	
	Perfect	Doped	Perfect	Doped		Perfect	Doped	Perfect	Doped
Layer 1					Layer 1				
B1	64	—	60	—	N1	75	—	242	—
B11	—	65	—	58	N11	—	76	—	263
B12	—	70	—	54	N12	—	59	—	224
B13	—	73	—	54	N13	—	88	—	241
B14	—	66	—	57	N14	—	74	—	242
B15	—	64	—	58	N15	—	74	—	243
B16	—	64	—	59	N16	—	75	—	245
Layer 2					Layer 2				
B2	69	—	43	—	N2	111	—	195	—
B21	—	74	—	42	N21	—	119	—	199
B22	—	—	—	—	N22	—	—	—	—
B23	—	75	—	49	N23	—	112	—	137
B24	—	70	—	44	N24	—	115	—	195
B25	—	69	—	43	N25	—	110	—	194
B26	—	68	—	45	N26	—	110	—	198
Layer 3					Layer 3				
B3	69	—	39	—	N3	115	—	187	—
B31	—	68	—	42	N31	—	64	—	97
B32	—	—	—	—	N32	—	—	—	—
B33	—	—	—	—	N33	—	114	—	136
B34	—	70	—	42	N34	—	113	—	184
B35	—	69	—	41	N35	—	115	—	188
B36	—	68	—	41	N36	—	113	—	182
Layer 4					Layer 4				
B4	70	—	46	—	N4	148	—	94	—
B41	—	70	—	47	N41	—	155	—	77
B42	—	70	—	57	N42	—	152	—	94
B43	—	74	—	44	N43	—	141	—	119
B44	—	70	—	45	N44	—	151	—	92
B45	—	70	—	45	N45	—	148	—	95
B46	—	70	—	45	N46	—	149	—	94

The NMR parameters at the sites of <sup>11</sup>B, <sup>15</sup>N nuclei in (d) model are quite similar with the (c) model (Tables 6 and 7).

#### 4. Conclusion

We have investigated the properties of the electronic structure of the pyrazine-doping in the BNNTs by performing the DFT calculations. The geometries were optimized at the B3LYP/6-311G\*\* level of theory. The structural energies, LUMO-HOMO gaps, dipole moments, and electronegativity ( $\chi$ ) for perfect model and doped models have been calculated. The results of the perfect and doped models reveal some remarkable trends.

First, the optimization process reveals that BN nanotube surface is not smooth like CNTs but the N nuclei were

relaxed outward and the B nuclei were relaxed inward of the nanotubes surface. Second, the values of dipole moments and band gaps are changed in the pyrazine-doped models. Third, the average B–N bond length in the (6,0) perfect BNNT was 1.45–1.46 Å, but this value was changed in the PD-BNNTs. Fourth, in the perfect model, the NMR parameters can divide BNNT structure into equivalent layers in which the B-mouth (B1) has the smallest CS<sup>I</sup> but the N-mouth (N4) has the largest CS<sup>I</sup> among the B and N layers, respectively.

Fifth, the results indicated the changes of NMR parameters are significant just for those atoms placed in the nearest neighboring of the pyrazine-doped ring. Clearly, pyrazine ring doping effect is totally different from Carbon impurity effect on electrostatic properties of BNNTs [36].

## References

- [1] H. W. Kroto, J. R. Heath, S. C. O'Brien, R. F. Curl, and R. E. Smalley, "C<sub>60</sub>: buckminsterfullerene," *Nature*, vol. 318, no. 6042, pp. 162–163, 1985.
- [2] R. W. Cahn, "Nanostructured materials," *Nature*, vol. 348, no. 6300, pp. 389–390, 1990.
- [3] S. Iijima, "Helical microtubules of graphitic carbon," *Nature*, vol. 354, no. 6348, pp. 56–58, 1991.
- [4] M. S. Dresselhaus, G. Dresselhaus, and P. C. Eklund, *Science of Fullerenes and Carbon Nanotubes*, Academic Press, San Diego, Calif, USA, 1996.
- [5] N. G. Chopra, R. J. Luyken, K. Cherrey et al., "Boron nitride nanotubes," *Science*, vol. 269, no. 5226, pp. 966–967, 1995.
- [6] X. Blase, A. Rubio, S. G. Louie, and M. L. Cohen, "Stability and band gap constancy of boron-nitride nanotubes," *Europhysics Letters*, vol. 28, pp. 335–340, 1994.
- [7] A. Rubio, J. L. Corkill, and M. L. Cohen, "Quasiparticle band structures of short-period superlattices and ordered alloys of AlN and GaN," *Physical Review B*, vol. 49, no. 3, pp. 1952–1956, 1994.
- [8] J. Yu, J. Ahn, S. F. Yoon et al., "Semiconducting boron carbonitride nanostructures: nanotubes and nanofibers," *Applied Physics Letters*, vol. 77, no. 13, pp. 1949–1951, 2000.
- [9] D. Golberg, P. Dorozhkin, Y. Bando, M. Hasegawa, and Z. C. Dong, "Semiconducting B-C-N nanotubes with few layers," *Chemical Physics Letters*, vol. 359, pp. 220–228, 2002.
- [10] W. Q. Han and A. Zettl, "Functionalized boron nitride nanotubes with a stannic oxide coating: a novel chemical route to full coverage," *Journal of the American Chemical Society*, vol. 125, no. 8, pp. 2062–2063, 2003.
- [11] C. Tang, Y. Bando, Y. Huang et al., "Fluorination and electrical conductivity of BN nanotubes," *Journal of the American Chemical Society*, vol. 127, no. 18, pp. 6552–6553, 2005.
- [12] H. J. Xiang, J. Yang, J. G. Hou, and Q. Zhu, "Are fluorinated boron nitride nanotubes n-type semiconductors?" *Applied Physics Letters*, vol. 87, no. 24, Article ID 243113, pp. 1–3, 2005.
- [13] Y. Chen, L. T. Chadderton, J. F. Gerald, and J. S. Williams, "A solid-state process for formation of boron nitride nanotubes," *Applied Physics Letters*, vol. 74, no. 20, pp. 2960–2962, 1999.
- [14] E. Hernández, C. Goze, P. Bernier, and A. Rubio, "Elastic properties of C and B<sub>x</sub>C<sub>y</sub>N<sub>z</sub> composite nanotubes," *Physical Review Letters*, vol. 80, no. 20, pp. 4502–4505, 1998.
- [15] A. P. Suryavanshi, M. F. Yu, J. Wen, C. Tang, and Y. Bando, "Elastic modulus and resonance behavior of boron nitride nanotubes," *Applied Physics Letters*, vol. 84, no. 14, pp. 2527–2529, 2004.
- [16] D. Golberg, Y. Bando, K. Kurashima, and T. Sato, "Synthesis and characterization of ropes made of BN multiwalled nanotubes," *Scripta Materialia*, vol. 44, no. 8–9, pp. 1561–1565, 2001.
- [17] Y. Xiao, X. H. Yan, J. X. Cao, J. W. Ding, Y. L. Mao, and J. Xiang, "Specific heat and quantized thermal conductance of single-walled boron nitride nanotubes," *Physical Review B*, vol. 69, no. 20, Article ID 205415, 2004.
- [18] C. W. Chang, W. Q. Han, and A. Zettl, "Thermal conductivity of B-C-N and BN nanotubes," *Applied Physics Letters*, vol. 86, pp. 173102–173103, 2005.
- [19] W. Han, Y. Bando, K. Kurashima, and T. Sato, "Synthesis of boron nitride nanotubes from carbon nanotubes by a substitution reaction," *Applied Physics Letters*, vol. 73, no. 21, pp. 3085–3087, 1998.
- [20] A. Loiseau, F. Willaime, N. Demoncy, G. Hug, and H. Pascard, "Boron nitride nanotubes with reduced numbers of layers synthesized by arc discharge," *Physical Review Letters*, vol. 76, no. 25, pp. 4737–4740, 1996.
- [21] X. Blase, A. Rubio, S. G. Louie, and M. L. Cohen, "Quasiparticle band structure of bulk hexagonal boron nitride and related systems," *Physical Review B*, vol. 51, no. 11, pp. 6868–6875, 1995.
- [22] D. Golberg, Y. Bando, M. Eremets, K. Takemura, K. Kurashima, and H. Yusa, "Nanotubes in boron nitride laser heated at high pressure," *Applied Physics Letters*, vol. 69, no. 14, pp. 2045–2047, 1996.
- [23] D. Golberg, Y. Bando, M. Eremets et al., "Boron nitride nanotube growth defects and their annealing-out under electron irradiation," *Chemical Physics Letters*, vol. 279, no. 3–4, pp. 191–196, 1997.
- [24] O. R. Lourie, C. R. Jones, B. M. Bartlett, P. C. Gibbons, R. S. Ruoff, and W. E. Buhro, "CVD growth of boron nitride nanotubes," *Chemistry of Materials*, vol. 12, no. 7, pp. 1808–1810, 2000.
- [25] E. Bengu and L. D. Marks, "Single-walled BN nanostructures," *Physical Review Letters*, vol. 86, no. 11, pp. 2385–2387, 2001.
- [26] M. Mirzaei and A. Nouri, "The Al-doped BN nanotubes: a DFT study," *Journal of Molecular Structure*, vol. 942, no. 1–3, pp. 83–87, 2010.
- [27] M. Mirzaei, "Calculation of chemical shielding in C-doped zigzag BN nanotubes," *Monatshefte fur Chemie*, vol. 140, no. 11, pp. 1275–1278, 2009.
- [28] A. E. Reed, L. A. Curtiss, and F. Weinhold, "Intermolecular interactions from a natural bond orbital, donor-acceptor viewpoint," *Chemical Reviews*, vol. 88, no. 6, pp. 899–926, 1988.
- [29] D. E. Glendening, A. E. Reed, J. E. Carpenter, and F. Weinhold, NBO, Version 3.1.
- [30] M. J. Frisch, G. W. Trucks, H. B. Schlegel et al., *Gaussian 98*, Gaussian, Pittsburgh, Pa, USA, 1998.
- [31] R. G. Parr and W. Yang, "Density functional approach to the frontier-electron theory of chemical reactivity," *Journal of the American Chemical Society*, vol. 106, no. 14, pp. 4049–4050, 1984.
- [32] K. D. Sen and C. K. Jorgensen, *Electronegativity, Structure and Bonding*, Springer, New York, NY, USA, 1987.
- [33] K. Wolinski, J. F. Hinton, and P. Pulay, "Efficient implementation of the gauge-independent atomic orbital method for NMR chemical shift calculations," *Journal of the American Chemical Society*, vol. 112, no. 23, pp. 8251–8260, 1990.
- [34] R. S. Drago, *Physical Methods for Chemists*, Saunders College Publishing, Orlando, Fla, USA, 2nd edition, 1992.
- [35] U. Haerberlen, *Advances in Magnetic Resonance*, Academic Press, New York, NY, USA, 1976, Edited by J.S. Waugh.
- [36] M. Mirzaei, "The carbon-doped (4,4) boron nitride nanotube: a computational NMR approach," *Physica E*, vol. 41, no. 5, pp. 883–885, 2009.

## Research Article

# Nuclear Magnetic Resonance Parameters of Pure and Diborinin-Doped (6,0) Single-Walled Zigzag BNNT: DFT Study

Sattar Arshadi, Saboora Abedini, Ameneh Asghari, and Fatemeh Alipour Zaghmarzi

*Department of Chemistry, Payame Noor University, Tehran 19395-4697, Iran*

Correspondence should be addressed to Sattar Arshadi, [chemistry\\_arshadi@yahoo.com](mailto:chemistry_arshadi@yahoo.com)

Received 24 June 2012; Revised 14 September 2012; Accepted 4 October 2012

Academic Editor: Sebastian O. Danielache

Copyright © 2013 Sattar Arshadi et al. This is an open access article distributed under the Creative Commons Attribution License, which permits unrestricted use, distribution, and reproduction in any medium, provided the original work is properly cited.

A computational study on the basis of density functional theory (DFT) calculations has been performed to investigate the properties of the electronic structure of (6,0) zigzag boron nitride nanotubes and two models ((a) and (b)) of diborinin-doped boron nitride nanotubes (DBD-BNNTs). The calculated structural energies yield similar values for two models of DBD-BNNTs. Isotropic ( $CS^I$ ) and anisotropic ( $CS^A$ ) chemical shielding parameters of the optimized BNNT and DBD-BNNTs are calculated. The results illustrate that the changes in chemical shielding tensors of  $^{11}\text{B}$  and  $^{15}\text{N}$  nuclei are more significant in the nearest neighborhood of the diborinin ring due to doping process. The changes of the electronic sites of the N atoms are also more significant than those of the B atoms. The dipole moments of the diborinin-doped BNNT structures show changes with respect to the pristine model. It is clear that the doping of diborinin ring decreases the energy gaps of the pure BNNT. For the pure model, the HOMO is located on the nitrogen atoms, and the LUMO is uniformly distributed throughout the B–N bonds. In contrast, for the diborinin-doped models, the majority of the HOMO and LUMO are located at the diborinin-doped regions.

## 1. Introduction

Nanostructures such as nanotube are currently the subject of intense research because of the potential applications in nanoscale electronic and optoelectronic fields [1–4]. After the exploration of carbon nanotubes (CNT) by Iijima in 1991 [1], nanotubes of other chemical compositions such as boron nitride have also been investigated [5]. Boron nitride nanotubes (BNNTs) have been the focus of several experimental and theoretical studies on account of their potential applications in high speed electronics [6]. BNNTs were successfully synthesized [7] shortly after prediction in theory [8].

BNNTs are a typical member of III-V, compound with morphology similar to that of carbon nanotubes (CNTs) but with their own distinct properties. However, the electrical properties of BNNTs are very different from those of CNTs. While CNTs come in three basic forms (metallic, small-gap semiconductor, and modest-gap semiconductor) rely on diameter and chirality, first approximation of BNNTs are electrically uniform with an energy gap of about 4–5 eV [9]. This energy gap is independent of wall number, diameter,

or chirality. For low applied electric fields, BNNTs are thus essentially insulating.

A tubular structure of BN can be formed by rolling up a sheet of hexagonal rings with boron and nitrogen in equal proportions possessing peculiar electrical [10], optical [11], and thermal [12] properties, which drastically differ from those of CNTs. BNNTs have high surface area, unique physical properties and morphology. On top of that, BNNTs possess high chemical stability. These properties make BNNTs one of most promising materials for nanotechnology applications, especially under oxidative, hazardous and high-temperature environments. But there have been quite a few attempts to control the properties by incorporating extrinsic foreign atom doping. These substitutions in BNNT significantly modify the chemical binding configuration, physical, chemical, and optical properties in comparison to pure BNNT [13].

Carbon-, Si-, Ti- and Pt-doped [14–18] BNNTs have been studied, and their results reveal that the electronic properties of BNNTs might be exploited for various applications. Generally, doping of BNNTs with other elements is a promising approach to control their electronic structures.

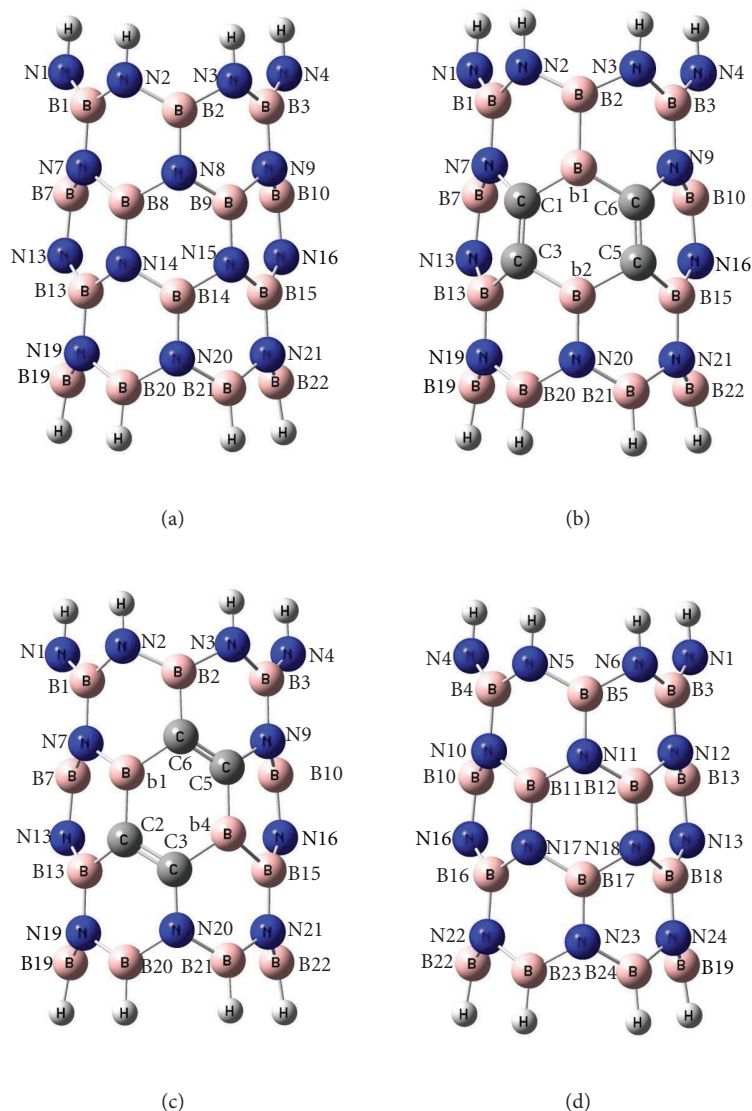


FIGURE 1: Typical geometric structures pure and diborinin-doped (6,0) single-walled zigzag BNNT; (a) front side of pure model, (b) and (c) front side of DBD-BNNTs, and (d) back side of pure and DBD-BNNTs models.

On the other hand, the BNNTs are produced through heating of C templates with  $B_2O_3$  in a flowing  $N_2$  atmosphere at 1503–1773 K. Due to this process, carbon atoms replace with B and N atoms but somewhere, diborinin ring formation as a defect in BNNT structure come into view.

Exploitation of the chemical and physical properties of nanotubes requires understanding and control of their structure during synthesis. While several techniques are used to probe nanotube structure, full characterization is not possible.  $^{11}B$  and  $^{15}N$  NMR spectroscopy have the potential to provide a more detailed structural characterization.

In this direction, we have studied the structure of electronic properties and nuclear magnetic resonance (NMR) parameters of  $^{11}B$  and  $^{15}N$  nuclei for pure (6,0) single-walled zigzag BNNT ((a) model) and DBD-BNNT ((b) and (c) models) *via* density functional theory method (DFT).

The zigzag (6,0) BNNT is chosen here because the zigzag orientation is a preferred growth one and the (6,0) BNNT has a moderate diameter. In addition, we have investigated atomic charge of distribution in nanotubes by natural bond orbital (NBO).

## 2. Models and Computational Details

DFT calculations were carried out using the Gaussian 98 program [19] on the structure of pure and DBD-BNNT BNNTs. DFT has become extremely popular for molecular applications because it accounts for the correlation energy in computationally efficient manner and offers a substantially improved accuracy over conventional approaches. Subsequently, frequency calculations (keyword: FREQ = NORAMAN) were carried out by standard techniques on

the optimized structures. For minimum state species, only real frequency values (with a positive sign) are accepted.

As was pointed out in the previous section, calculations have been performed on (a), (b), and (c) models (Figure 1). Two structural isomers of DBD-BNNTs ((b) and (c) models) were considered in the calculations within four  $sp^2$ -hybridized carbon and two borons atoms (diborinin ring) were substituted instead of three boron and three nitrogen atoms in the middle of the nanotube.

At the first step of this study, each of the considered pure and diborinin-doped representative models of BNNTs was allowed to fully relax during the geometrical optimization and frequency calculation. The geometries were optimized at the B3LYP/6-311G\*\* level of theory. Subsequently, the NBO analysis was carried out on the B3LYP/6-311G\*\* wave functions. From the NBO calculations, highest-occupied molecular orbital (HOMO) and lowest-unoccupied molecular orbital (LUMO) energies, the band gap energies, dipole moments and electronegativity ( $\chi$ ) for (a), (b), and (c) models of BNNTs were obtained.

Also, we investigated electronegativity ( $\chi$ ) in the optimized structures. Within the conceptual framework of DFT, the electronegativity of a system of  $N$  particles, with total energy  $E$  and subject to the external potential  $v(r)$ , is defined as

$$\chi = -\left(\frac{\partial E}{\partial N}\right)_{v(r),T}. \quad (1)$$

In (1),  $\chi$  is the electronegativity [20–25]. Pauling introduced the concept of electronegativity as the power of an atom in a molecule to attract electrons [20]. Using the method of finite difference, an operational and approaching definition of  $\chi$  is:

$$\chi = \frac{1}{2}(\text{IP} + \text{EA}), \quad (2)$$

where IP is the ionization potential and EA is the electron affinity of the system. Within the validity of Koopman's theorem for closed-shell species, the frontier orbital energies are given by

$$-E_{\text{LUMO}} = \text{IP}; \quad -E_{\text{HOMO}} = \text{EA}. \quad (3)$$

Therefore, on the basis of orbitals, we can write

$$\chi = -\frac{1}{2}(E_{\text{LUMO}} + E_{\text{HOMO}}). \quad (4)$$

$E_{\text{LUMO}}$  and  $E_{\text{HOMO}}$  are the energies of the lowest unoccupied and the highest occupied molecular orbitals LUMO and HOMO, respectively.

Finally nuclear magnetic resonance (NMR) parameters at  $^{11}\text{B}$  and  $^{15}\text{N}$  nuclei of the optimized structures have been calculated. As noted, we have carried out these calculations at the GIAO/B3LYP/6-311++G\*\* level, one of the best compromises between accuracy and computer time [26].

Mathematically, the anisotropic and isotropic chemical shifts are described by a 3 by 3 matrix. In this principal axis system, the chemical shift tensor is fully described by the three diagonal elements—the principal components ( $\sigma_{33} >$

$\sigma_{22} > \sigma_{11}$ )—and the three eigenvectors or Euler angles describe the orientation of the principal axes with respect to an arbitrary frame. Therefore, (5) and (6) are used to convert the calculated chemical shielding (CS) tensors to the isotropic ( $CS^I$ ) and anisotropic ( $CS^A$ ) parameters. The isotropic value (the centre of gravity) is the average value of the principal components, and the anisotropy describe the largest separation from the centre of gravity. The evaluated NMR parameters for (b) and (c) models of DBD-BNNTs are listed in Tables 2 and 3, respectively. For the ease of comparison, the NMR parameters for (a) model of pure BNNT are listed in these tables. The following are equations (5) and (6):

$$CS^I \text{ (ppm)} = \frac{(\sigma_{11} + \sigma_{22} + \sigma_{33})}{3}, \quad (5)$$

$$CS^A \text{ (ppm)} = \frac{\sigma_{33} - (\sigma_{11} + \sigma_{22})}{2}. \quad (6)$$

### 3. Result and Discussion

**3.1. Geometries.** As shown in Figure 1, by substituting three B and three N atoms of pure BNNT ((a) model) with four  $sp^2$ -hybridized carbons and two boron atoms, in the middle of the nanotube, (b) and (c) models of DBD-BNNTs are produced.

At the first step, geometrical optimizations and frequency calculations have been successfully carried out for the pure and doped models (a, b, and c) of single-wall (6,0) BNNT at the level of B3LYP/6-311G\*\* basis set. The optimized geometries of pure and doped models of the BNNTs are listed in Figures 2 and 3. These figures present the optimized parameters including the bond lengths and bond angles for three models that investigated (6,0) BNNT. In the pure BNNT (Figure 2(a)), the average B–N bond length is 1.46 Å, consistent with previously reported DFT calculations [27, 28]. This value was also changed by the diborinin-doping in the DBD-BNNT due to existence of B–C, N–C, B–B, and C=C bonds, in addition to, B–N one.

However, the effects of this deformation are consequential, just at the geometrical properties of the nearest atoms to the diborinin-doped ring, whereas those of other atoms are almost remained unchanged. As shown in Figures 2(b) and 2(c), the average C=C and B–C bond lengths (1.36 Å and 1.56 Å, resp.) are different from B–N bond length (1.46 Å). Moreover, the changes of the bond angles are more than those of the bond lengths in the (6,0) zigzag DBD-BNNT (Figures 2 and 3).

The calculated structural energies, LUMO-HOMO gaps, electronegativity ( $\chi$ ), and dipole moments for three models of the investigated BNNTs have been listed in Table 1.

The calculated structural energies of two structural isomers ((b) and (c) models) of DBD-BNNT are equal to –51.2 keV and indicate no difference between them.

For better understanding of the nature of interaction in the diborinin-doped models, we studied the electronic properties of the models. The energies of both the highest occupied molecular orbital (HOMO) and the lowest unoccupied molecular orbital (LUMO) are negative in all of

TABLE 1: B3LYP/6-311G\*\* calculated properties of pure and diborinin-doped ((b) and (c) models) of BNNT.

Systems	HOMO (eV)	LUMO (eV)	$\Delta E_{(LUMO-HOMO)}$ (eV)	$\chi$ (eV)	Dipole moment (Debye)	Energy (keV)
Pure (a)	-6.86	-1.99	4.87	4.42	7.47	-52.2
DBD-BNNT (b)	-5.93	-3.28	2.64	4.61	9.28	-51.2
DBD-BNNT (c)	-5.99	-3.15	2.83	4.57	6.98	-51.2

TABLE 2: The  $CS^I$  and  $CS^A$  parameters of the (b) model of DBD-BNNT.

$^{11}\text{B}$	$CS^I$ (ppm)				$CS^A$ (ppm)						
	Pure	DBD-BNNT	$^{15}\text{N}$	Pure	DBD-BNNT	$^{11}\text{B}$	Pure	DBD-BNNT	$^{15}\text{N}$	Pure	DBD-BNNT
layer 1						layer 1					
		72.5	N1		144.1	B1	43.2	N1		90.8	
		67.2	N2		127.3	B2	80.4	N2		124.7	
	70.5	72.6	N3	147.5	128.1	B3	44.5	N3	95	123.3	
		70.8	N4		144.1	B4		N4		91.4	
		69.8	N5		147.6	B5		N5		95.3	
		70.9	N6		146.9	B6		N6		96.6	
layer 2						layer 2					
		67.3	N7		80.3	B7	43.0	N7		213.0	
		—	N8		—	B8	—	N8		—	
	69	—	N9	114	80.0	B9	40.5	N9	187	213.2	
		67.4	N10		116.4	B10		N10		187.0	
		68.7	N11		113.8	B11		N11		187.9	
		68.3	N12		115.8	B12		N12		187.5	
layer 3						layer 3					
		67.2	N13		94.4	B13	59.5	N13		232.0	
		—	N14		—	B14	—	N14		—	
	69.5	66.9	N15	111	—	B15	43	N15	195.5	—	
		69.4	N16		94.0	B16		N16		232.6	
		68.9	N17		109.7	B17		N17		197.4	
		69.3	N18		110.5	B18		N18		197.0	
layer 4						layer 4					
		64.9	N19		67.9	B19	60.8	N19		257.2	
		63.1	N20		49.1	B20	59.8	N20		267.0	
	64	63.6	N21	75	67.5	B21	60	N21	241.5	258.0	
		65.0	N22		73.9	B22		N22		243.3	
		63.8	N23		75.5	B23		N23		242.2	
		63.9	N24		73.5	B24		N24		243.2	

model systems under study. The calculated energy gap for the pure BNNT is 4.87 eV (Table 1). In comparison to the pure systems, the energy gaps between HOMO and LUMO, ( $\Delta E_{(LUMO-HOMO)}$ ), have small values in (b) and (c) models of DBD-BNNT. The electronic densities of states (DOSs) of pure and diborinin-doped BNNT are plotted in Figure 4 for better understanding, the effect of diborinin ring doping to the electronic structure of BNNT. The electronic structures observed near Fermi level of the pure BNNT (Figure 4(a)) also show significant changes due to the diborinin ring doping (see Figures 4(b)-4(c)). So, the band gaps near Fermi level become sharply narrower. It is clear that the doping of diborinin ring decreases the energy gaps of the pure BNNT.

The HOMO and LUMO, the pure and diborinin-doped models are plotted in Figure 5. For the pure model, the

HOMO is located on the nitrogen atoms of the (6,0) zigzag BNNT model and corresponds to the lone pair of electron on nitrogen atoms. In contrast, the LUMO is uniformly distributed throughout the B-N bonds. For the diborinin-doped models, the majority of the HOMO and LUMO are located at the diborinin-doped regions.

The edges of the armchair BNNTs include N and B atoms in both ends. In contrast to armchair models, edges of the zigzag BNNTs consist of one type atoms, either N or B atoms; if one of the ends is formed by N atoms, the other end is formed by B atoms. The B atoms are slightly positive and the N atoms are slightly negative. Therefore, the zigzag BNNT is a polar material (has a nonzero dipole moment) and this entry could be better seen by the value of its dipole moment. Comparing the values of the dipole moments for the two

TABLE 3: The  $CS^I$  and  $CS^A$  parameters of the (c) model of DBD-BNNT.

$^{11}\text{B}$	$CS^I$ (ppm)				$^{11}\text{B}$	$CS^A$ (ppm)					
	Pure	DBD-BNNT	$^{15}\text{N}$	Pure		Pure	DBD-BNNT	$^{15}\text{N}$	Pure	DBD-BNNT	
layer 1					layer 1						
B1		68.6	N1		143.3	B1		46.2	N1		93.2
B2		65.1	N2		137.6	B2		63.0	N2		102.9
B3	70.5	68.6	N3	147.5	130.3	B3	44.5	48.8	N3	95	129.6
B4		69.5	N4		148.0	B4		46.4	N4		92.8
B5		70.1	N5		148.4	B5		45.8	N5		92.5
B6		69.1	N6		147.8	B6		47.5	N6		92.4
layer 2						layer 2					
B7		68.5	N7		98.2	B7		39.7	N7		211.8
B8		—	N8		—	B8		—	N8		—
B9	69	—	N9	114	86.3	B9	40.5	—	N9	187	184.3
B10		67.9	N10		110.6	B10		39.0	N10		184.0
B11		67.9	N11		111.7	B11		41.1	N11		190.3
B12		67.9	N12		113.6	B12		42.1	N12		185.5
layer 3						layer 3					
B13		66.3	N13		108.0	B13		64.1	N13		205.6
B14		—	N14		—	B14		—	N14		—
B15	69.5	56.6	N15	111	—	B15	43	89.9	N15	195.5	—
B16		70.3	N16		84.8	B16		43.8	N16		243.9
B17		68.8	N17		112.3	B17		43.8	N17		196.5
B18		69.2	N18		111.4	B18		43.0	N18		195.9
layer 4						layer 4					
B19		65.0	N19		67.9	B19		58.3	N19		276.7
B20		69.8	N20		45.9	B20		60.0	N20		256.6
B21	64	66.0	N21	75	65.8	B21	60	55.4	N21	241.5	273.4
B22		66.0	N22		70.7	B22		59.5	N22		247.9
B23		64.5	N23		73.8	B23		58.1	N23		244.5
B24		64.9	N24		70.4	B24		58.1	N24		247.4

diborinin-doped models indicate, that the value for the (b) model is significantly increased ( $D = 9.28$  Debye) whereas for (c) model is significantly reduced ( $D = 6.98$  Debye), compared with the pure model ( $D = 7.47$  Debye), which means that the orientations of diborinin ring in two diborinin-doped models foundation diverse dipole moment for these models (Figure 1 and Table 1).

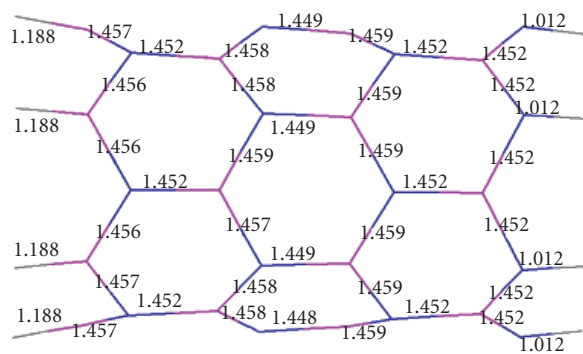
**3.2. NMR Parameter.** NMR spectroscopy has proven to be an exceptionally powerful technique in characterizing molecular systems and structures. So, we have performed theoretical calculations of  $^{11}\text{B}$  and  $^{15}\text{N}$  NMR data for (a), (b), and (c) models to study the influence of diborinin ring doping on the electronic structure properties of the (6,0) BNNT.

**3.2.1. Pure Model.** Tables 2 and 3 present the calculated NMR parameters for various  $^{11}\text{B}$  and  $^{15}\text{N}$  nuclei in the pure (a) model of BNNT. This model includes 24 B and 24 N atoms, where the edges are saturated by 12 H atoms (Figure 1). The edge of this model consists of one type atom, either N or B atoms; if one of the end is formed by N atoms (N-tip), the other ends is formed by B atoms (B-tip).

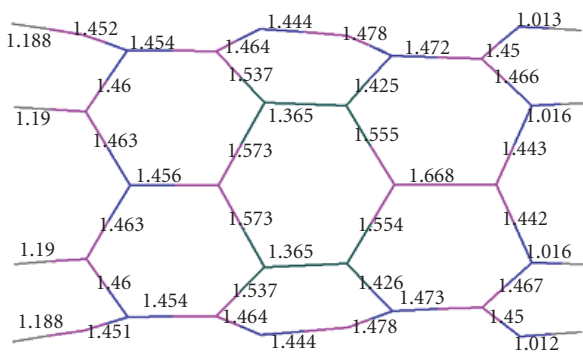
According to the previous studies, to compare CS tensors between pure and doped models,  $^{11}\text{B}$  and  $^{15}\text{N}$  nuclei in the pure (a) model are divided into four different layers which sense similar electrostatic properties in each layer, yielding the same values of the  $CS^I$  and  $CS^A$  parameters [29]. Almost no significant difference is observed in the calculated NMR parameters for the atoms of each layer; hence, just the average values in each layer for  $^{15}\text{N}$  and  $^{11}\text{B}$  nuclei are reported in Tables 2 and 3.

The first layer consists of N1–N6 atoms and the last layer contains B19–B24 atoms, which forms the N-tip and B-tip of the considered models of BNNT, respectively. The values of NMR properties for the  $^{11}\text{B}$  and  $^{15}\text{N}$  nuclei of the pure (a) model indicate that the B-tip has the smallest value of  $CS^I$  for both  $^{11}\text{B}$  (64 ppm) and  $^{15}\text{N}$  (75 ppm) nuclei. Similarly N-tip has the smallest value of  $CS^A$  for both  $^{11}\text{B}$  (44 ppm) and  $^{15}\text{N}$  (95 ppm) nuclei, among the other layers of nuclei.

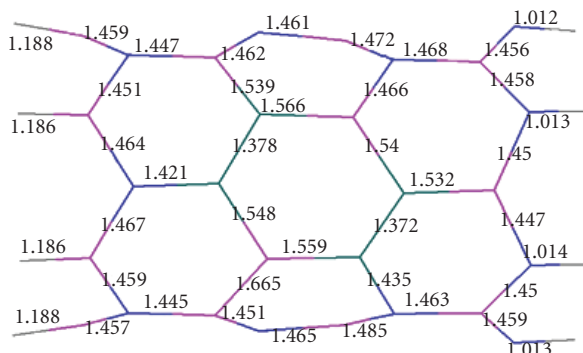
The nature of the valence shells of the N atoms, which have lone pair of electrons, and the B atoms, which have a lack of electrons, is different. Therefore, different behaviors of the CS properties are expected and are also observed for these atoms. For these reasons, the average values of  $CS^I$  are greater



(a)



(b)



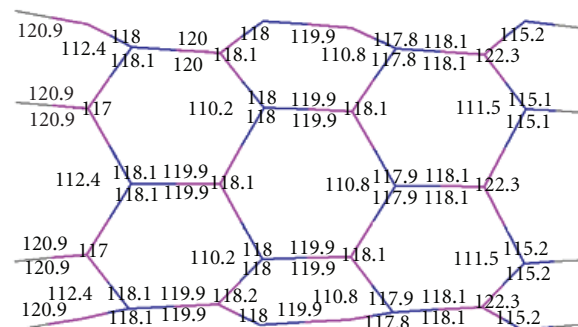
(c)

FIGURE 2: Optimized bond lengths (Å) at B3LYP/6-311G\*\* level; (a) pure model, (b) and (c) diborinin-doped models.

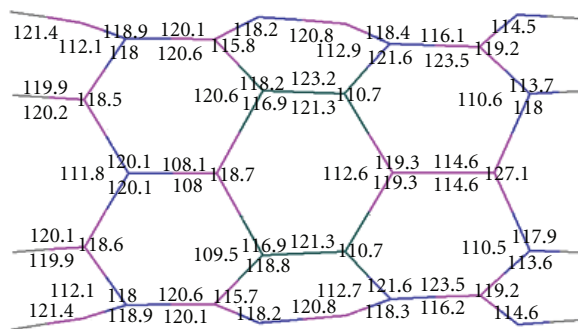
than  $CS^A$  in  $^{11}\text{B}$  nuclei whereas the opposite order have been seen for  $^{15}\text{N}$  nuclei.

**3.2.2. Diborinin-Doped Models.** We characterize  $^{11}\text{B}$  and  $^{15}\text{N}$  NMR parameters of BNNT and illustrate how the diborinin-doping modifies the NMR parameter of the pure BNNT. According to Gauge-Independent Atomic Orbital (GIAO) calculations performed later, doping of diborinin ring in (6,0) BNNT, in both cases of doped models induces significant deformation of the B and N layers. These impurities lead to a significant change of the NMR parameter.

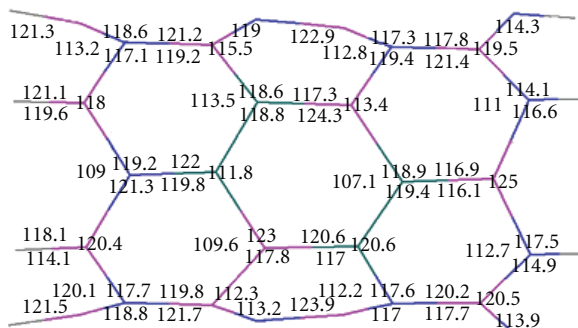
Compared to the pure model, in (b) model of the diborinin-doped (Figure 1(b)), N8, N14, N15, B8, B14 and B9 atoms are, respectively, doped by the b1, C3, C5, C2, b4



(a)



(b)



(c)

FIGURE 3: Optimized bond angles (°) at B3LYP/6-311G\*\* level; (a) pure model, (b) and (c) diborinin-doped models.

and C6 atoms. In contrast of (b) model, in (c) model of the diborinin-doped (Figure 1(c)), N8, N14, N15, B8, B14 and B9 atoms, respectively, are doped by the C6, C2, B4, B1, C3 and C5 atoms.

Among the B atoms of the (b) and (c) models, B2, B13 and B15 are significantly influenced by diborinin-doping due to the (b) model B2, B13 and B15 are directly bonded to the b1, C3 and C5 atoms, respectively while in the (c) model, B2, B13 and B15 are directly bonded to the C6, C2 and b4 atoms respectively, hence, their CS parameters detect some changes due to the diborinin doping. This observation was more significant for N7, N9, and N20 atoms which were directly bonded to the diborinin ring. This is because, in the DBD-BNNT, the CS parameters are proportional to the electronic density at the atomic sites and could detect any perturbation to these sites.

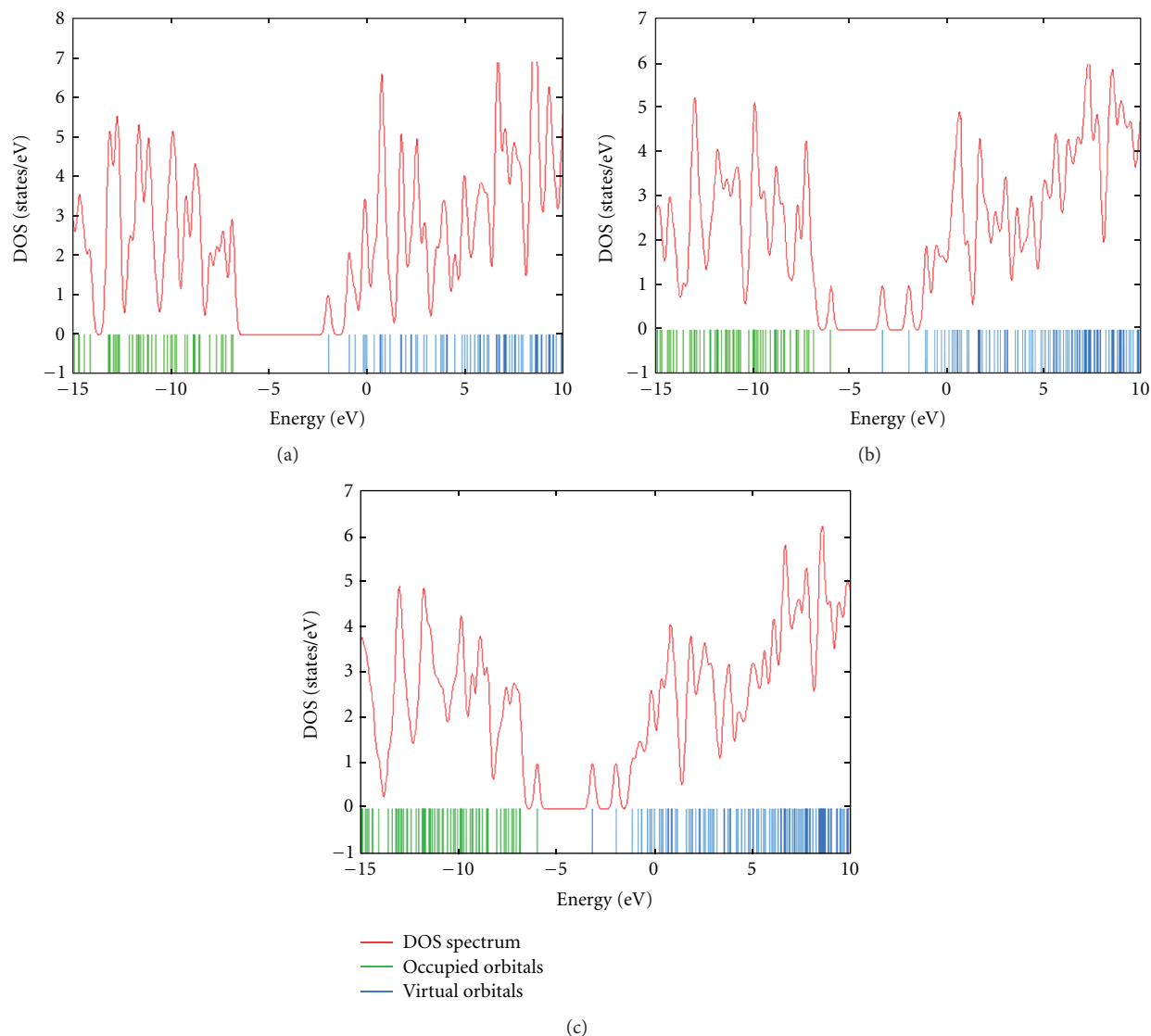


FIGURE 4: The density of states (DOS) of (a) pure model, (b) and (c) diborinin-doped models.

The results of Tables 2 and 3 reveal the significant effect of diborinin-doping at the sites of those  $^{11}\text{B}$  and  $^{15}\text{N}$  nuclei located in the nearest neighborhood (closer distance) of the DBD-BNNTs ((b) and (c) models), but negligible influence at the sites of those nuclei farther from the diborinin-doped rings. Also, in (b) and (c) models, the  $CS^I$  parameters are changed by diborinin-doping, the magnitude of the change for  $^{15}\text{N}$  being more significant rather than that for the  $^{11}\text{B}$  nuclei.

The  $CS^I$  parameters of B20 and B21 which were located in the B-tip of the (c) model are influenced indirectly by the diborinin-doping, whereas those of B20 and B21 in the (b) model remained unchanged.

Meanwhile, the magnitude of changes of the CS tensors at the sites of  $^{15}\text{N}$  nuclei was placed in the nearest neighborhood of diborinin ring is larger for the form (b) than the form (c), whereas the magnitude of changes of the CS tensors at the

sites of  $^{15}\text{N}$  nuclei was placed in the first neighborhood of diborinin ring is larger for the form (c) than the form (b).

In the diborinin-doped models, when compared to the pure model, changes are greater in the values of CS parameters of those N atoms (N7, N9 and N20) which are directly bonded to diborinin ring in the (b) model borininthan in the (c) model whereas, the magnitude of changes of CS parameters of those B atoms (B2, B13, and B15) which are directly bonded to diborinin ring are more in (c) model borininthan in (b) model.

Table 4 shows the average deviations of (b) model (and (c) model in bracket) for  $CS^I$  and  $CS^A$  of  $^{11}\text{B}$  and  $^{15}\text{N}$  in all layers of DBD-BNNT. The positive average deviations show increasing the values of  $CS^I$  and  $CS^A$  in DBD-BNNT models relative to pure model. The changes of CS parameters of B atoms in the diborinin-doped (c) model are generally greater than (b) model. These orders are reverse for N atoms.

TABLE 4: The average deviations of (b) model (and (c) model in brackets) for  $CS^I$  and  $CS^A$  of  $^{11}\text{B}$  and  $^{15}\text{N}$  in N-tip and B-tip of DBD-BNNT.

	$CS^I$		$CS^A$	
	$^{11}\text{B}$	$^{15}\text{N}$	$^{11}\text{B}$	$^{15}\text{N}$
Layer 1 (N-Tip)	0.13 [-2.00]	-7.82 [-4.93]	5.47 [5.12]	8.68 [5.56]
Layer 2	-1.075 [-0.95]	-13.24 [-10.42]	1.1 [-0.025]	10.72 [4.18]
Layer 3	-1.16 [-3.26]	-8.85 [-6.87]	6.74 [13.92]	19.25 [14.97]
Layer 4 (B-Tip)	0.05 [2.03]	-7.1 [-9.25]	-0.33 [-1.77]	10.32 [16.25]

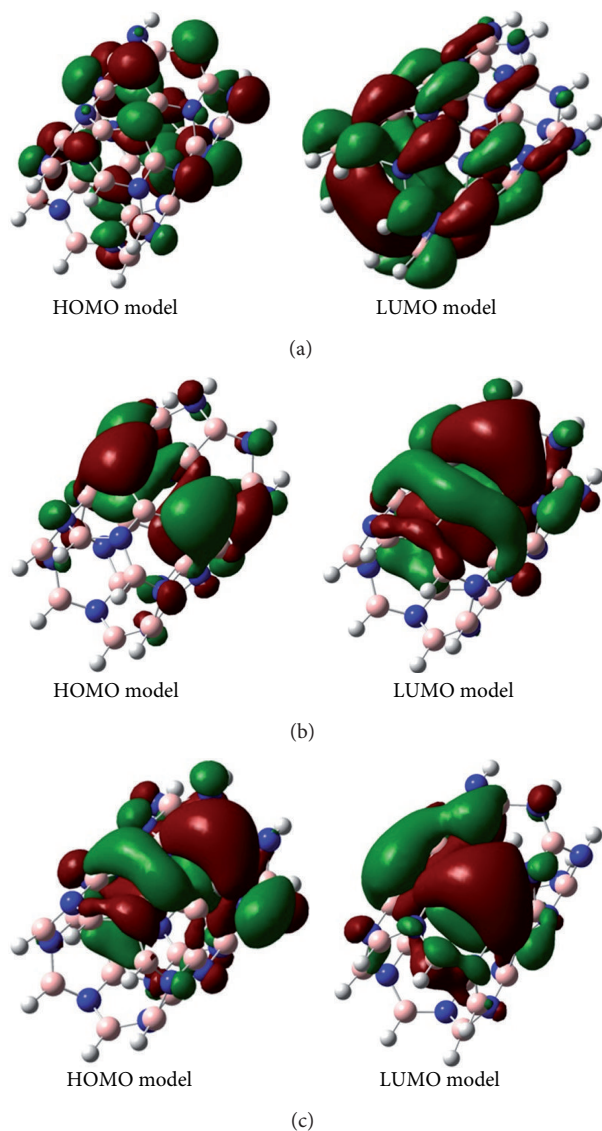


FIGURE 5: HOMO and LUMO orbitals for different models of the BNNTs; (a) pure model, (b) and (c) diborinin-doped models.

As a result, Table 4 shows changes in the average deviations of N atoms are greater than those of B atoms. Also changes of  $CS^I$  and  $CS^A$  of  $^{11}\text{B}$  and  $^{15}\text{N}$  in layer 2 and 3 (directly bonded) are more than N-tip and B-tip of DBD-BNNT.

## 4. Conclusion

In this study, we have used DFT calculations to investigate the properties of the electronic structure of pure and DBD-BNNTs through to simulate the  $^{11}\text{B}$  and  $^{15}\text{N}$  spectra. The calculated structural energies yield similar values for the (b) and (c) models of DBD-BNNTs. However, the band gap differences between the forms (b) and the pure models are more than the differences between the forms (c) and the pure models of the BNNTs. Also, the B-N bond lengths and bond angles detect changes of diborinin-doped models. When diborinin is doped on the BNNT, dipole moment of the pure system is significantly changed. CS parameters detect the effects of diborinin-doping on the properties of nanotubes in comparison with the pure model. For the (b) and (c) models, both of the  $CS^I$  and  $CS^A$  parameters were significantly changed due to the diborinin-doped ring. The changes in the NMR ( $CS^I$ ) parameters due to the diborinin doping are more significant for the N atoms than the B atoms regarding to the pure model.

Results show the Average deviations of (b) model [and (c) model in bracket] for  $CS^I$  and  $CS^A$  of  $^{11}\text{B}$  and  $^{15}\text{N}$  in all layers of DBD-BNNT. The positive average deviations show increasing the values of  $CS^I$  and  $CS^A$  in DBD-BNNT models relative to pure model. In the diborinin-doped (c) model, when compared to the (b) model, changes generally are greater in the values of CS parameters of those B atoms. These orders are reverse for N atoms.

Our results show that changes in the average deviations of N atoms are greater than those of B atoms. Also, changes of  $CS^I$  and  $CS^A$  of  $^{11}\text{B}$  and  $^{15}\text{N}$  in layer 2, and 3 (directly bonded) are more than N-tip and B-tip of DBD-BNNT.

In DOS, the electronic structures observed near Fermi level of the pure BNNT show significant change due to the diborinin ring doping. So the band gaps near Fermi level become sharply narrower. It is clear that the doping of diborinin ring decreases the energy gaps of the pure BNNT.

For the pure model, the HOMO is located on the nitrogen atoms and the LUMO is uniformly distributed throughout the B-N bonds. In contrast, for the diborinin-doped models, the majority of the HOMO and LUMO are located at the diborinin-doped regions.

## Acknowledgment

This paper is dedicated to the beloved colleague Mr. Ali Karimian, who rests in peace at this time; but without his sincere assistance, this work would not be materialized.

## References

- [1] S. Iijima, "Helical microtubules of graphitic carbon," *Nature*, vol. 354, no. 6348, pp. 56–58, 1991.
- [2] J. Hu, T. W. Odom, and C. M. Lieber, "Chemistry and physics in one dimension: synthesis and properties of nanowires and nanotubes," *Accounts of Chemical Research*, vol. 32, no. 5, pp. 435–445, 1999.
- [3] M. Law, J. Goldberger, and P. Yang, "Semiconductor nanotubes and nanowires," *Annual Review of Materials Research*, vol. 34, pp. 83–122, 2004.
- [4] M. S. Gudixsen, L. J. Lauhon, J. Wang, D. C. Smith, and C. M. Lieber, "Growth of nanowire superlattice structures for nanoscale photonics and electronics," *Nature*, vol. 415, no. 6872, pp. 617–620, 2002.
- [5] M. Farahani, T. S. Ahmadi, and A. Seif, "A DFT study of the nuclear magnetic response of the zigzag AlN-BN and BN-AlN nanotube junctions," *Journal of Molecular Structure: THEOCHEM*, vol. 913, no. 1–3, pp. 126–130, 2009.
- [6] N. G. Chopra, R. J. Luyken, K. Cherrey et al., "Boron nitride nanotubes," *Science*, vol. 269, no. 5226, pp. 966–967, 1995.
- [7] A. Rubio, J. L. Corkill, and M. L. Cohen, "Theory of graphitic boron nitride nanotubes," *Physical Review B*, vol. 49, no. 7, pp. 5081–5084, 1994.
- [8] S. Riikonen, A. S. Foster, A. V. Krasheninnikov, and R. M. Nieminen, "Computational study of boron nitride nanotube synthesis: how catalyst morphology stabilizes the boron nitride bond," *Physical Review B*, vol. 80, no. 15, Article ID 155429, 14 pages, 2009.
- [9] A. Zettl, J. Cumings, W. Han, and W. Mickelson, "Boron nitride nanotube peapods," *AIP Conference Proceedings*, vol. 633, pp. 140–144, 2002.
- [10] R. Pati, P. Panigrahi, P. P. Pal, B. Akdim, and R. Pachter, "Gate field induced electronic current modulation in a single wall boron nitride nanotube: molecular scale field effect transistor," *Chemical Physics Letters*, vol. 482, no. 4–6, pp. 312–315, 2009.
- [11] J. S. Lauret, R. Arenal, F. Ducastelle et al., "Optical transitions in single-wall boron nitride nanotubes," *Physical Review Letters*, vol. 94, no. 3, Article ID 037405, 4 pages, 2005.
- [12] Y. Xiao, X. H. Yan, J. Xiang et al., "Specific heat of single-walled boron nitride nanotubes," *Applied Physics Letters*, vol. 84, no. 23, pp. 4626–4628, 2004.
- [13] D. Jana, L. C. Chen, C. W. Chen, and K. H. Chen, "An ab-initio approach to the optical properties of C<sub>x</sub>N<sub>y</sub> single wall nanotubes," *Diamond and Related Materials*, vol. 18, no. 5–8, pp. 1002–1005, 2009.
- [14] R. J. Baierle, P. Piquini, T. M. Schmidt, and A. Fazzio, "Hydrogen adsorption on carbon-doped boron nitride nanotube," *Journal of Physical Chemistry B*, vol. 110, no. 42, pp. 21184–21188, 2006.
- [15] F. Li, Y. Xia, M. Zhao et al., "Theoretical study of hydrogen atom adsorbed on carbon-doped BN nanotubes," *Physics Letters A*, vol. 357, no. 4–5, pp. 369–373, 2006.
- [16] S. A. Shevlin and Z. X. Guo, "Hydrogen sorption in defective hexagonal BN sheets and BN nanotubes," *Physical Review B*, vol. 76, no. 2, Article ID 024104, 11 pages, 2007.
- [17] E. Durgun, Y. R. Jang, and S. Ciraci, "Hydrogen storage capacity of Ti-doped boron-nitride and B Be-substituted carbon nanotubes," *Physical Review B*, vol. 76, no. 7, Article ID 073413, 4 pages, 2007.
- [18] X. Wu, J. L. Yang, and X. C. Zeng, "Adsorption of hydrogen molecules on the platinum-doped boron nitride nanotubes," *Journal of Chemical Physics*, vol. 125, no. 4, Article ID 044704, 6 pages, 2006.
- [19] M. J. Frisch, G. W. Trucks, H. B. Schlegel et al., *GAUSSIAN 98*, Gaussian, Inc., Pittsburgh, Pa, USA, 1998.
- [20] R. G. Pearson, *Hard and Soft Acid and Bases*, Dowden, Hutchinson and Ross, Stroudsburg, Pa, USA, 1973.
- [21] R. G. Pearson, "Hard and soft acids and bases-the evolution of a chemical concept," *Coordination Chemistry Reviews*, vol. 100, pp. 403–425, 1990.
- [22] R. G. Pearson, *Chemical Hardness*, Wiley-VCH, Oxford, UK, 1997.
- [23] P. W. Ayers and R. Parr, "Variational principles for describing chemical reactions: the Fukui function and chemical hardness revisited," *Journal of the American Chemical Society*, vol. 122, no. 9, pp. 2010–2018, 2000.
- [24] L. Pauling, *The Nature of Chemical Bond*, Cornell University Press, New York, NY, USA, 1960.
- [25] K. D. Sen and C. K. Jorgensen, *Electronegativity: Structure and Bonding*, vol. 66, Springer, Berlin, Germany, 1987.
- [26] I. Alkorta and J. Elguero, "Computational NMR spectroscopy," in *Computational Spectroscopy: Methods, Experiments and Applications*, J. Grunenberg, Ed., Wiley-VCH, Weinheim, Germany, 2010.
- [27] M. Mirzaei and M. Miirzaei, "An electronic structure study of O-terminated zigzag BN nanotubes: density functional calculations of the quadrupole coupling constants," *Solid State Communications*, vol. 150, no. 27–28, pp. 1238–1240, 2010.
- [28] M. Mirzaei, "The NMR parameters of the SiC-doped BN nanotubes: a DFT study," *Physica E*, vol. 42, no. 7, pp. 1954–1957, 2010.
- [29] M. Mirzaei, "Calculation of chemical shielding in C-doped zigzag BN nanotubes," *Monatshefte fur Chemie*, vol. 140, no. 11, pp. 1275–1278, 2009.

## Research Article

# ITP Adjuster 1.0: A New Utility Program to Adjust Charges in the Topology Files Generated by the PRODRG Server

Diogo de Jesus Medeiros,<sup>1</sup> Wilian Augusto Cortopassi,<sup>1,2</sup>  
Tanos Celmar Costa França,<sup>2</sup> and André Silva Pimentel<sup>1</sup>

<sup>1</sup> Department of Chemistry, Pontifical Catholic University of Rio de Janeiro, Rua Marquês de São Vicente 225, Gávea, 22453-900 Rio de Janeiro, RJ, Brazil

<sup>2</sup> Laboratory of Molecular Modeling Applied to the Chemical and Biological Defense (LMCBD), Military Institute of Engineering, Praça General Tibúrcio, 80, Urca, 22290-270 Rio de Janeiro, RJ, Brazil

Correspondence should be addressed to Diogo de Jesus Medeiros; dioginnn@hotmail.com

Received 30 June 2012; Accepted 3 August 2012

Academic Editor: Cristiano R. W. Guimarães

Copyright © 2013 Diogo de Jesus Medeiros et al. This is an open access article distributed under the Creative Commons Attribution License, which permits unrestricted use, distribution, and reproduction in any medium, provided the original work is properly cited.

The suitable computation of accurate atomic charges for the GROMACS topology \*.itp files of small molecules, generated in the PRODRG server, has been a tricky task nowadays because it does not calculate atomic charges using an ab initio method. Usually additional steps of structure optimization and charges calculation, followed by a tedious manual replacement of atomic charges in the \*.itp file, are needed. In order to assist this task, we report here the ITP Adjuster 1.0, a utility program developed to perform the replacement of the PRODRG charges in the \*.itp files of small molecules by ab initio charges.

## 1. Introduction

The GROMACS package [1] is extensively used for energy minimizations (EM) and molecular dynamics (MD) simulations of biomolecules such as proteins, nucleic acids, peptides, and drugs [2–11]. The input topology files used by GROMACS [1] for small molecules (\*.itp files) may be generated by the server PRODRG [12]. However, these files must be adjusted for MD due to the charge group concepts adopted by PRODRG [12].

The topology files preparation for performing EM and MD simulations with GROMACS [1] is very important in investigations of biological processes involving drug interactions with their molecular targets. The force fields available for biomolecules in the literature [13–16] are generally based on macromolecules, such as proteins and nucleic acids, making the preparation of consistent and reliable topology files for small ordinary molecules a challenging task. The PRODRG server [12] is a reliable tool for quickly generating topologies and coordinates of ligands in protein-ligand complexes, using the empirical GROMOS96 force field [14],

from a variety of different input files. This tool has been used in several studies and a wide range of knowledge areas [17–25]. This server works with the concept of charge groups, which is defined as a group of bonded atoms that sums an integer total charge. Lemkul et al. [26] investigated the quality of topologies generated by the PRODRG server [12] for small molecules for the GROMOS96 43A1 force field [14] and described their functional groups. Their results show that the atomic partial charges are critically incompatible with the GROMOS force fields. Furthermore, when we use the PRODRG [12] parameters, the behavior of the system is notably different than the one observed using the GROMOS parameters. Thus, they suggest a more consistent strategy for the calculation of partial atomic charges, avoiding the deviation of behavior in the system.

Several computer programs are available for structure optimization and charge calculations using quantum chemical calculations [27–29]. The Frisch et al. software [30] has been reported as the most standard for quantum chemical calculations of small molecules [31–33]. Thus, the ITP adjuster 1.0 was built to make the interface of Frisch et al.

TABLE 1: \*.itp files of folic acid before (left) and after (right) applying ITP Adjuster 1.0.

Nr	Type	resnr	resid	Atom	cgnr	Charge	Mass	Nr	Type	resnr	resid	Atom	cgnr	Charge	Mass
1	CR1	1	FOL	C15	1	0.022	12.0110	1	CR1	1	FOL	C15	1	0.113688	12.0110
2	HC	1	FOL	H15	1	0.058	1.0080	2	HC	1	FOL	H15	1	0.091572	1.0080
3	NR	1	FOL	N3	1	-0.434	14.0067	3	NR	1	FOL	N3	1	-0.504841	14.0067
4	C	1	FOL	C16	1	0.335	12.0110	4	C	1	FOL	C16	1	0.798970	12.0110
5	NR	1	FOL	N6	1	-0.434	14.0067	5	NR	1	FOL	N6	1	-0.821446	14.0067
6	C	1	FOL	C19	1	0.453	12.0110	6	C	1	FOL	C19	1	0.946175	12.0110
7	NT	1	FOL	N7	2	0.082	14.0067	7	NT	1	FOL	N7	2	-0.931989	14.0067
8	H	1	FOL	H72	2	0.027	1.0080	8	H	1	FOL	H72	2	0.414024	1.0080
9	H	1	FOL	H71	2	0.027	1.0080	9	H	1	FOL	H71	2	0.433222	1.0080
10	NR	1	FOL	N5	2	0.061	14.0067	10	NR	1	FOL	N5	2	-0.786769	14.0067
11	H	1	FOL	H53	2	0.027	1.0080	11	H	1	FOL	H53	2	0.414871	1.0080
12	C	1	FOL	C18	2	0.294	12.0110	12	C	1	FOL	C18	2	0.698881	12.0110
13	O	1	FOL	O4	2	-0.676	15.9994	13	O	1	FOL	O4	2	-0.485705	15.9994
14	C	1	FOL	C17	2	0.158	12.0110	14	C	1	FOL	C17	2	-0.275218	12.0110
15	NR	1	FOL	N4	3	-0.619	14.0067	15	NR	1	FOL	N4	3	-0.194434	14.0067
16	C	1	FOL	C14	3	0.127	12.0110	16	C	1	FOL	C14	3	0.172175	12.0110
17	CH2	1	FOL	C13	3	0.161	14.0270	17	CH2	1	FOL	C13	3	0.134163	14.0270
18	N	1	FOL	N2	3	0.127	14.0067	18	N	1	FOL	N2	3	-0.476189	14.0067
19	H	1	FOL	H22	3	0.021	1.0080	19	H	1	FOL	H22	3	0.222443	1.0080
20	C	1	FOL	C3	3	0.127	12.0110	20	C	1	FOL	C3	3	0.404365	12.0110
21	CR1	1	FOL	C4	3	0.015	12.0110	21	CR1	1	FOL	C4	3	-0.305799	12.0110
22	HC	1	FOL	H4	3	0.041	1.0080	22	HC	1	FOL	H4	3	0.156776	1.0080
23	CR1	1	FOL	C5	4	0.000	12.0110	23	CR1	1	FOL	C5	4	-0.091238	12.0110
24	HC	1	FOL	H51	4	0.000	1.0080	24	HC	1	FOL	H51	4	0.118576	1.0080
25	CR1	1	FOL	C2	4	0.000	12.0110	25	CR1	1	FOL	C2	4	-0.334445	12.0110
26	HC	1	FOL	H21	4	0.000	1.0080	26	HC	1	FOL	H21	4	0.172869	1.0080
27	CR1	1	FOL	C1	4	0.000	12.0110	27	CR1	1	FOL	C1	4	-0.022017	12.0110
28	HC	1	FOL	H11	4	0.000	1.0080	28	HC	1	FOL	H11	4	0.106113	1.0080
29	C	1	FOL	C6	4	0.000	12.0110	29	C	1	FOL	C6	4	-0.147662	12.0110
30	C	1	FOL	C7	5	0.429	12.0110	30	C	1	FOL	C7	5	0.566722	12.0110
31	O	1	FOL	O1	5	-0.612	15.9994	31	O	1	FOL	O1	5	-0.487695	15.9994
32	N	1	FOL	N1	5	0.176	14.0067	32	N	1	FOL	N1	5	-0.654534	14.0067
33	H	1	FOL	H12	5	0.030	1.0080	33	H	1	FOL	H12	5	0.322800	1.0080
34	CH1	1	FOL	C8	5	0.229	13.0190	34	CH1	1	FOL	C8	5	0.290274	13.0190
35	C	1	FOL	C12	5	0.428	12.0110	35	C	1	FOL	C12	5	0.640657	12.0110
36	O	1	FOL	O3	5	-0.612	15.9994	36	O	1	FOL	O3	5	-0.499644	15.9994
37	OA	1	FOL	O6	5	-0.149	15.9994	37	OA	1	FOL	O6	5	-0.637158	15.9994
38	H	1	FOL	H6	5	0.081	1.0080	38	H	1	FOL	H6	5	0.456952	1.0080
39	CH2	1	FOL	C9	6	0.198	14.0270	39	CH2	1	FOL	C9	6	0.004713	14.0270
40	CH2	1	FOL	C10	6	0.198	14.0270	40	CH2	1	FOL	C10	6	-0.014129	14.0270
41	C	1	FOL	C11	6	0.384	12.0110	41	C	1	FOL	C11	6	0.703747	12.0110
42	O	1	FOL	O2	6	-0.685	15.9994	42	O	1	FOL	O2	6	-0.512801	15.9994
43	OA	1	FOL	O5	6	-0.167	15.9994	43	OA	1	FOL	O5	6	-0.633904	15.9994
44	H	1	FOL	H52	6	0.072	1.0080	44	H	1	FOL	H52	6	0.432867	1.0080

[30] with the GROMACS package [1]. However, it may also be easily modified to work with different quantum chemical softwares.

There are several problems to adjust the output files of PRODRG [12] based on Frisch et al. [30] output files (\*.out files): (i) the manual edition of the topology charges is an

exhausting, tedious, and time-demanding assignment and, so, very susceptible to mistakes; (ii) PRODRG [12] uses a charge group concept, differently from Frisch et al. [30] and any other quantum chemical softwares; (iii) the numbering of hydrogen atoms in the \*.itp files is incompatible with the output files from quantum chemical softwares; (iv) the bonds

TABLE 2: \*.itp files of cystein before (left) and after (right) applying ITP Adjuster 1.0.

Nr	Type	resnr	resid	Atom	cgnr	Charge	Mass	Nr	Type	resnr	resid	Atom	cgnr	Charge	Mass
1	OA	1	CYS	O2	1	-0.180	15.9994	1	OA	1	CYS	O2	1	-0.553855	15.9994
2	H	1	CYS	H22	1	0.057	1.0080	2	H	1	CYS	H22	1	0.366426	1.0080
3	C	1	CYS	C3	1	0.372	12.0110	3	C	1	CYS	C3	1	0.638891	12.0110
4	O	1	CYS	O1	1	-0.693	15.9994	4	O	1	CYS	O1	1	-0.478926	15.9994
5	CH1	1	CYS	C2	1	0.175	13.0190	5	CH1	1	CYS	C2	1	0.098300	13.0190
6	NT	1	CYS	N1	1	0.066	14.0067	6	NT	1	CYS	N1	1	-0.630975	14.0067
7	H	1	CYS	H16	1	0.012	1.0080	7	H	1	CYS	H16	1	0.282228	1.0080
8	H	1	CYS	H15	1	0.012	1.0080	8	H	1	CYS	H15	1	0.282036	1.0080
9	CH2	1	CYS	C1	1	0.153	14.0270	9	CH2	1	CYS	C1	1	-0.101843	14.0270
10	S	1	CYS	S1	1	0.077	32.0600	10	S	1	CYS	S1	1	0.049643	32.0600
11	H	1	CYS	H13	1	-0.051	1.0080	11	H	1	CYS	H13	1	0.048076	1.0080

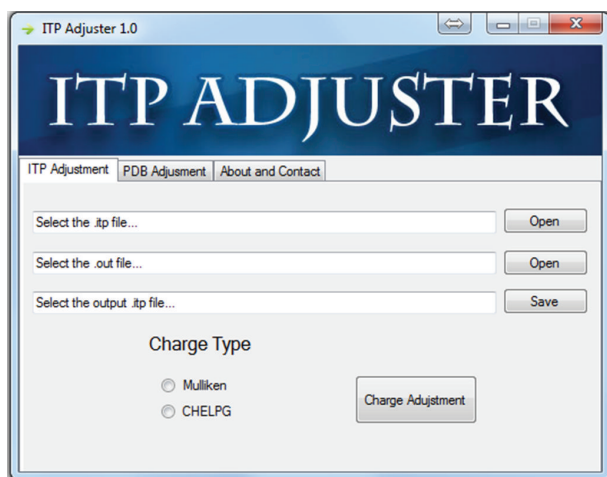


FIGURE 1: The ITP Adjuster interface.

information in the Frisch et al. [30] output files may have some inconsistencies, such as hydrogen atoms bonded to two different atoms.

The ITP Adjuster 1.0 (Figure 1) performs a quick and safe edition of the \*.itp files considering the charge calculations from Frisch et al. [30] using Mulliken or Chelpg (Charges from Electrostatic Potentials) charges. It handles charges of up to six decimal places. At the end of the execution, a message box will inform the total charge of the molecule in the edited \*.itp file, which may be used as a guide to detect inconsistencies between the \*.itp and \*.out files.

## 2. Materials and Methods

*2.1. Considerations for Using ITP Adjuster.* Some requirements for using the ITP Adjuster 1.0 are important to guarantee its proper installation and use, as discussed below.

ITP Adjuster 1.0 needs the Microsoft.Net Framework 4 or later installed for running properly. The authors recommend the Frisch et al. [30] calculations and PRODRG server [12] topology generation. It is highly desirable to have a \*.pdb

file with numbered atom names before submitting it to the PRODRG server [12]. It guarantees the correspondence of the atom names between the \*.out and the final \*.itp files. ITP Adjuster 1.0 also has a functionality named "PDB Adjustment," which verifies a \*.pdb file and, if necessary, numbers the atom names.

The hydrogen charges are based on the information of bonds presented in the Frisch et al. [30] output files, which is necessary to provide an \*.itp file which is compatible with the \*.out file indicated. An usual mistake occurs when the PRODRG server [12] removes hydrogen atoms from oxygen and nitrogen atoms or adds hydrogen atoms that do not exist in the \*.out file. In these cases, the user must use the ADDHYD, DELHYD, PATCH, or a combination of these commands in the PRODRG server [12] in order to correct these inconsistencies before using ITP Adjuster 1.0. Not performing this strategy leads to unreliable final \*.itp files and meaningless total charges.

## 3. Results and Discussion

*3.1. Validating ITP Adjuster 1.0.* We validated the ITP Adjuster 1.0 with the three common molecules in biological systems: folic acid, adenosine-5'-triphosphate (ATP), and cystein. Structures of these molecules are shown in Figure 2. First we built their 3D structures in the \*.pdb format using Gauss View 4.0 and Frisch et al. [30] and submitted them to energy minimization with Frisch et al. [30] using the algorithm B3LYP/3-21G with charge chelpg, in order to generate their \*.out files. Besides, the \*.itp files of each molecule were generated at the PRODRG server [12]. The \*.out and \*.itp files were then loaded into the ITP Adjuster 1.0 to change the charges of the \*.itp files generated by the PRODRG server [12] by using ab initio charges of the \*.out files from Frisch et al. [30]. The results are presented in Tables 1, 2, and 3. As it can be seen, the ITP Adjuster 1.0 was able to recognize the atoms in each file. It properly adjusted the charges without modifying the positions of the atoms. The ITP Adjuster 1.0 was also tested against several other small molecules (data not shown) and, without exception, it was able to adjust charges accordingly.

TABLE 3: \*.itp files of ATP before (left) and after (right) applying ITP Adjuster 1.0.

Nr	Type	resnr	resid	Atom	cgnr	Charge	Mass	Nr	Type	resnr	resid	Atom	cgnr	Charge	Mass
1	OA	1	ATP	O12	1	-0.256	15.9994	1	OA	1	ATP	O12	1	-0.674862	15.9994
2	H	1	ATP	H12	1	0.001	1.0080	2	H	1	ATP	H12	1	0.395648	1.0080
3	P	1	ATP	P3	1	1.081	30.9738	3	P	1	ATP	P3	1	1.542343	30.9738
4	OA	1	ATP	O13	1	-0.256	15.9994	4	OA	1	ATP	O13	1	-0.731008	15.9994
5	H	1	ATP	H13	1	0.001	1.0080	5	H	1	ATP	H13	1	0.418396	1.0080
6	OM	1	ATP	O7	1	-0.151	15.9994	6	OM	1	ATP	O7	1	-0.606703	15.9994
7	OA	1	ATP	O6	1	0.246	15.9994	7	OA	1	ATP	O6	1	-0.781970	15.9994
8	P	1	ATP	P2	1	1.081	30.9738	8	P	1	ATP	P2	1	1.666306	30.9738
9	OA	1	ATP	O11	1	-0.256	15.9994	9	OA	1	ATP	O11	1	-0.709606	15.9994
10	H	1	ATP	H11	1	0.001	1.0080	10	H	1	ATP	H11	1	0.430751	1.0080
11	OM	1	ATP	O5	2	0.000	15.9994	11	OM	1	ATP	O5	2	-0.656411	15.9994
12	OA	1	ATP	O4	3	-0.191	15.9994	12	OA	1	ATP	O4	3	-0.836197	15.9994
13	P	1	ATP	P1	3	1.389	30.9738	13	P	1	ATP	P1	3	1.661303	30.9738
14	OA	1	ATP	O10	3	-0.199	15.9994	14	OA	1	ATP	O10	3	-0.668092	15.9994
15	H	1	ATP	H93	3	0.001	1.0080	15	H	1	ATP	H93	3	0.410779	1.0080
16	OM	1	ATP	O3	4	-0.177	15.9994	16	OM	1	ATP	O3	4	-0.641581	15.9994
17	OA	1	ATP	O2	4	-0.289	15.9994	17	OA	1	ATP	O2	4	-0.604805	15.9994
18	CH2	1	ATP	C10	4	-0.062	12.0110	18	CH2	1	ATP	C10	4	0.301881	12.0110
19	CH1	1	ATP	C9	4	0.093	12.0110	19	CH1	1	ATP	C9	4	0.289979	12.0110
20	OA	1	ATP	O1	4	-0.289	15.9994	20	OA	1	ATP	O1	4	-0.515384	15.9994
21	CH1	1	ATP	C8	4	0.024	12.0110	21	CH1	1	ATP	C8	4	0.189925	12.0110
22	OA	1	ATP	O8	4	-0.301	15.9994	22	OA	1	ATP	O8	4	-0.558061	15.9994
23	H	1	ATP	H82	4	0.001	1.0080	23	H	1	ATP	H82	4	0.358163	1.0080
24	CH1	1	ATP	C7	5	0.047	12.0110	24	CH1	1	ATP	C7	5	0.186587	12.0110
25	OA	1	ATP	O9	5	0.261	15.9994	25	OA	1	ATP	O9	5	-0.541491	15.9994
26	H	1	ATP	H92	5	0.001	1.0080	26	H	1	ATP	H92	5	0.370706	1.0080
27	CH1	1	ATP	C6	5	0.126	12.0110	27	CH1	1	ATP	C6	5	0.578117	12.0110
28	NR	1	ATP	N3	5	0.169	14.0067	28	NR	1	ATP	N3	5	-0.804205	14.0067
29	CR1	1	ATP	C5	5	-0.059	12.0110	29	CR1	1	ATP	C5	5	0.257766	12.0110
30	HC	1	ATP	H51	5	-0.023	1.0080	30	HC	1	ATP	H51	5	0.276650	1.0080
31	NR	1	ATP	N4	6	-0.499	14.0067	31	NR	1	ATP	N4	6	-0.572949	14.0067
32	C	1	ATP	C3	6	0.096	12.0110	32	C	1	ATP	C3	6	0.176370	12.0110
33	C	1	ATP	C4	6	0.247	12.0110	33	C	1	ATP	C4	6	0.666733	12.0110
34	NR	1	ATP	N2	6	-0.512	14.0067	34	NR	1	ATP	N2	6	-0.611459	14.0067
35	CR1	1	ATP	C1	6	-0.048	12.0110	35	CR1	1	ATP	C1	6	0.210905	12.0110
36	HC	1	ATP	H1	6	-0.019	1.0080	36	HC	1	ATP	H1	6	0.220957	1.0080
37	NR	1	ATP	N1	6	-0.512	14.0067	37	NR	1	ATP	N1	6	-0.605878	14.0067
38	C	1	ATP	C2	6	0.247	12.0110	38	C	1	ATP	C2	6	0.640460	12.0110
39	NT	1	ATP	N5	7	0.031	14.0270	39	NT	1	ATP	N5	7	-0.794455	14.0270
40	H	1	ATP	H53	7	-0.016	1.0080	40	H	1	ATP	H53	7	0.327604	1.0080
41	H	1	ATP	H52	7	-0.015	1.0080	41	H	1	ATP	H52	7	0.336786	1.0080

#### 4. Conclusion

We reported here the development of the ITP Adjuster 1.0, a utility program built to adjust ab initio charges into \*.itp files

generated by the PRODRG server [12]. This utility program is already in use in our laboratory and proved to be very accurate in the interface of Frisch et al. [30] and GROMACS [1], providing a friendly user interface and a quick way

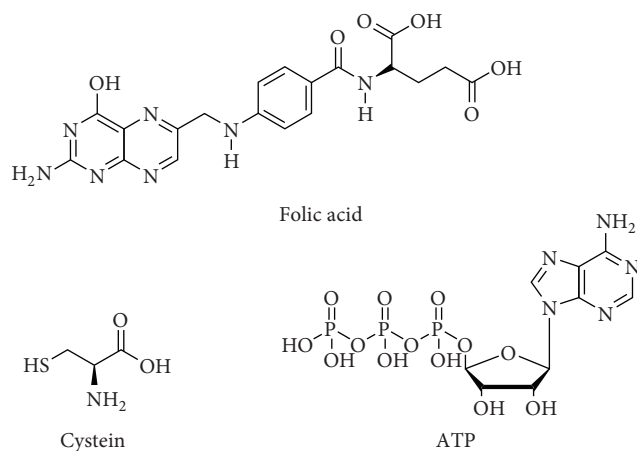


FIGURE 2: Structures of some molecules tested with ATP adjuster 1.0.

to generate suitable topology files to perform EM and MD calculations with the GROMACS package [1].

This utility program is available free of charge by request at lmm@puc-rio.br.

## Conflict of Interests

All the authors declare that there is no conflict of interests related to the publishing of this paper on the Journal of Chemistry or any direct financial relation with the trademarks mentioned in the paper.

## Acknowledgments

The authors thank the Brazilian funding agencies CNPq (Grant no. 304187/2009-7), CAPES (Grant no. 02559/09-9), and FAPERJ (Grant nos. E-26/101.452/2010 and E-26-111.532/2008) for financial support. W. A. Cortopassi also thanks CNPq, FAPERJ, the Estudar Foundation, and DM Branco for financial support and fellowship. A. S. Pimentel and T. C. C. Franca are recipients of the FAPERJ Young Scientist of Our State award.

## References

- [1] B. Hess, C. Kutzner, D. van der Spoel, and E. Lindahl, "GROMACS 4: algorithms for highly efficient, load-balanced, and scalable molecular simulation," *Journal of Chemical Theory and Computation*, vol. 4, no. 3, pp. 435–447, 2008.
- [2] Q. Wang, N. H. Werstik, J. R. Kramer, and R. A. Bell, "Effects of Cu ions and explicit water molecules on the copper binding domain of amyloid precursor protein APP(131-189): a molecular dynamics study," *Journal of Physical Chemistry B*, vol. 115, no. 29, pp. 9224–9235, 2011.
- [3] K. Ohno, T. Mitsui, Y. Tanida et al., "Docking study and binding free energy calculation of poly (ADP-ribose) polymerase inhibitors," *Journal of Molecular Modeling*, vol. 17, no. 2, pp. 383–389, 2011.
- [4] A. Hung and I. Yarovsky, "Inhibition of peptide aggregation by lipids: insights from coarse-grained molecular simulations," *Journal of Molecular Graphics and Modelling*, vol. 29, no. 5, pp. 597–607, 2011.
- [5] P. Lazar, S. Kim, Y. Lee, and K. W. Lee, "Computational approach to ensure the stability of the favorable ATP binding site in *E. coli* Hfq," *Journal of Molecular Graphics and Modelling*, vol. 29, no. 4, pp. 573–580, 2010.
- [6] P. Lazar, Y. Lee, S. Kim, M. Chandrasekaran, and K. W. Lee, "Molecular dynamics simulation study for ionic strength dependence of RNA-host factor interaction in *Staphylococcus aureus* Hfq," *Bulletin of the Korean Chemical Society*, vol. 31, no. 16, pp. 1519–1526, 2010.
- [7] S. J. Irudayam and M. L. Berkowitz, "Influence of the arrangement and secondary structure of melittin peptides on the formation and stability of toroidal pores," *Biochimica et Biophysica Acta*, vol. 1808, no. 9, pp. 2258–2266, 2011.
- [8] R. P. Wesołowski, S. Furmaniak, A. P. Terzyk, and P. A. Gauden, "Simulating the effect of carbon nanotube curvature on adsorption of polycyclic aromatic hydrocarbons," *Adsorption*, vol. 17, no. 1, pp. 1–4, 2011.
- [9] A. J. Bevers and A. Kukol, "Conformational flexibility of the peptide hormone ghrelin in solution and lipid membrane bound: a molecular dynamics study," *Journal of Biomolecular Structure and Dynamics*, vol. 23, no. 4, pp. 357–364, 2006.
- [10] P. Narang, K. Bhushan, S. Bose, and B. Jayaram, "Protein structure evaluation using an all-atom energy based empirical scoring function," *Journal of Biomolecular Structure and Dynamics*, vol. 23, no. 4, pp. 385–406, 2006.
- [11] Y. Tao, Z. H. Rao, and S. Q. Liu, "Insight derived from molecular dynamics simulation into substrate-induced changes in protein motions of proteinase K," *Journal of Biomolecular Structure and Dynamics*, vol. 28, no. 2, pp. 143–157, 2010.
- [12] A. W. Schüttelkopf and D. M. F. van Aalten, "PRODRG: a tool for high-throughput crystallography of protein-ligand complexes," *Acta Crystallographica D*, vol. 60, no. 8, pp. 1355–1363, 2004.
- [13] W. L. Jorgensen and J. Tirado-Rives, "The OPLS potential functions for proteins, energy minimizations for crystals of cyclic peptides and crambin," *Journal of the American Chemical Society*, vol. 110, no. 6, pp. 1657–1666, 1988.
- [14] W. F. van Gunsteren, S. R. Billeter, A. A. Eising et al., "Biomolecular simulation," in *The GROMOS96 Manual and User Guide*, vdf Hochschulverlag AG an der ETH Zürich and BIOMOS b.v., Groningen, The Netherlands, 1996.
- [15] W. D. Cornell, P. Cieplak, C. I. Bayly et al., "A second generation force field for the simulation of proteins, nucleic acids, and organic molecules," *Journal of the American Chemical Society*, vol. 117, no. 19, pp. 5179–5197, 1995.
- [16] S. J. Weiner, P. A. Kollman, D. A. Case et al., "A new force field for molecular mechanical simulation of nucleic acids and proteins," *Journal of the American Chemical Society*, vol. 106, no. 3, pp. 765–784, 1984.
- [17] W. A. Cortopassi, A. A. Oliveira, A. P. Guimarães, M. N. Rennó, A. U. Krettli, and T. C. C. Franca, "Docking studies on the binding of quinoline derivatives and hematin to *Plasmodium falciparum* lactate dehydrogenase," *Journal of Biomolecular Structure and Dynamics*, vol. 29, no. 1, pp. 207–218, 2011.
- [18] J. Penna-Coutinho, W. A. Cortopassi, A. A. Oliveira, T. C. C. Franca, and A. U. Krettli, "Antimalarial activity of potential inhibitors of *Plasmodium falciparum* lactate dehydrogenase

- enzyme selected by docking studies,” *PLoS ONE*, vol. 6, no. 7, Article ID e21237, 2011.
- [19] S. S. Tatke, V. Renugopalakrishnan, and M. Prabhakaran, “Interfacing biological macromolecules with carbon nanotubes and silicon surfaces: a computer modelling and dynamic simulation study,” *Nanotechnology*, vol. 15, no. 10, pp. S684–S690, 2004.
- [20] A. W. Schüttelkopf, O. A. Andersen, F. V. Rao et al., “Screening-based discovery and structural dissection of a novel family 18 chitinase inhibitor,” *The Journal of Biological Chemistry*, vol. 281, no. 37, pp. 27278–27285, 2006.
- [21] M. Subashini, P. V. Devarajan, G. S. Sonavane, and M. Doble, “Molecular dynamics simulation of drug uptake by polymer,” *Journal of Molecular Modeling*, vol. 17, no. 5, pp. 1141–1147, 2011.
- [22] A. P. Guimarães, A. A. Oliveira, E. F. F. Da Cunha, T. C. Ramalho, and T. C. C. França, “Design of new chemotherapeutics against the deadly anthrax disease. Docking and molecular dynamics studies of inhibitors containing pyrrolidine and riboamidrazone rings on nucleoside hydrolase from *Bacillus anthracis*,” *Journal of Biomolecular Structure and Dynamics*, vol. 28, no. 4, pp. 455–469, 2011.
- [23] A. A. Oliveira, M. N. Rennó, C. A. S. Matos et al., “Molecular modeling studies of yersinia pestis dihydrofolate reductase,” *Journal of Biomolecular Structure and Dynamics*, vol. 29, no. 2, pp. 351–367, 2011.
- [24] D. T. Mancini, K. S. Matos, E. F. F. Cunha et al., “Molecular modeling studies on nucleoside hydrolase from the biological warfare agent *Brucella suis*,” *Journal of Biomolecular Structure & Dynamics*, vol. 30, pp. 125–136, 2012.
- [25] A. P. Guimarães, A. A. Oliveira, E. F. F. da Cunha, T. C. Ramalho, and T. C. C. França, “Analysis of *Bacillus anthracis* nucleoside hydrolase via in silico docking with inhibitors and molecular dynamics simulation,” *Journal of Molecular Modeling*, vol. 17, pp. 2939–2951, 2011.
- [26] J. A. Lemkul, W. J. Allen, and D. R. Bevan, “Practical considerations for building GROMOS-compatible small-molecule topologies,” *Journal of Chemical Information and Modeling*, vol. 50, no. 12, pp. 2221–2235, 2010.
- [27] M. W. Schmidt, K. K. Baldridge, J. A. Boatz et al., “General atomic and molecular electronic structure system,” *Journal of Computational Chemistry*, vol. 14, no. 11, pp. 1347–1363, 1993.
- [28] M. Valiev, E. J. Bylaska, N. Govind et al., “NWChem: a comprehensive and scalable open-source solution for large scale molecular simulations,” *Computer Physics Communications*, vol. 181, no. 9, pp. 1477–1489, 2010.
- [29] J. P. Stewart, “MOPAC, 2009,” James Stewart Computational Chemistry, Colorado Springs, CO, USA, 2008, <http://OpenMOPAC.net>.
- [30] M. J. Frisch, G. W. Trucks, H. B. Schlegel et al., Gaussian03 03, Revision C.02, Gaussian03, Inc., Wallingford CT, 2004.
- [31] A. S. Christensen, S. P. A. Sauer, and J. H. Jensen, “Definitive benchmark study of ring current effects on amide proton chemical shifts,” *Journal of Chemical Theory and Computation*, vol. 7, no. 7, pp. 2078–2084, 2011.
- [32] V. W. Day, M. A. Hossain, O. K. Sung, D. Powell, G. Lushington, and K. Bowman-James, “Encircled proton,” *Journal of the American Chemical Society*, vol. 129, no. 28, pp. 8692–8693, 2007.
- [33] L. M. Goldman, D. R. Glowacki, and B. K. Carpenter, “Nonstatistical dynamics in unlikely places: [1,5] Hydrogen migration in chemically activated cyclopentadiene,” *Journal of the American Chemical Society*, vol. 133, no. 14, pp. 5312–5318, 2011.

## Research Article

# On the Difference between Self-Assembling Process of Monomeric and Dimeric Surfactants with the Same Head to Tail Ratio: A Lattice Monte Carlo Simulation

Reza Behjatmanesh-Ardakani and Maryam Farsad

Department of Chemistry, Payame Noor University, P.O. Box 19395-3697, Tehran, Iran

Correspondence should be addressed to Reza Behjatmanesh-Ardakani; [reza\\_b\\_m\\_a@yahoo.com](mailto:reza_b_m_a@yahoo.com)

Received 26 June 2012; Revised 8 August 2012; Accepted 9 August 2012

Academic Editor: André Silva Pimentel

Copyright © 2013 R. Behjatmanesh-Ardakani and M. Farsad. This is an open access article distributed under the Creative Commons Attribution License, which permits unrestricted use, distribution, and reproduction in any medium, provided the original work is properly cited.

Experimental data show that gemini surfactants have critical micelle concentrations that are almost tenfold lower than the CMCs of single chain ones. It is believed that the spacer groups play an important role in this subject. Short hydrophilic or long hydrophobic spacers can reduce CMC dramatically. In this paper, self-assembling processes of double-chain and one-chain surfactants with the same head to tail ratio are compared. Dimeric chain structure is exactly double of single chain. In other words, hydrophilic-lyophilic balances of two chain models are the same. Two single chains are connected head-to-head to form a dimeric chain, without introducing extra head or tail beads as a spacer group. Premicellar, micellar, and shape/phase transition ranges of both models are investigated. To do this, lattice Monte Carlo simulation in canonical ensemble has been used. Results show that without introducing extra beads as spacer group, the CMC of  $(H_3T_3)_2$  as a dimeric surfactant is much lower than the CMC of its similar single chain,  $H_3T_3$ . For dimeric case of study, it is shown that bolaform aggregates are formed.

## 1. Introduction

Gemini surfactants are relatively new type of surface active materials. They can self-assemble in a wide range from nanoscale (spherical micelles) to meso-scale aggregates (vesicles, monolayers, bilayers, and so on) [1]. A gemini surfactant contains two conventional single chain surfactant whose heads are connected by a hydrophobic or hydrophilic part named as spacer [2]. Gemini surfactants have very low critical micelle concentration (CMC) compared with the corresponding single chain surfactants. Unlike to the conventional amphiphile molecules with spherical micelles, gemini surfactants form unusual aggregation morphologies such as vesicles and bilayers [3, 4].

There are many experimental studies on gemini surfactants; however, surprisingly, only a few theoretical studies are found in the literature. The first molecular dynamics simulation of gemini amphiphiles has been conducted by Karaborni et al. [5], who used coarse-grained model to simulate gemini surfactants with different hydrophobic spacer

lengths. Their results showed that the structures of aggregates depend on the number of oil-like spacer between head parts. With single spacer, linear thread-like micelles are formed and for longer spacer, mixture of spheroid and tree-like aggregates are produced. Using Smit's model [6], Maiti et al. developed a simple coarse-grained model of surfactant oligomers containing dimeric and trimeric amphiphiles [7]. Their molecular dynamics simulation results exhibited formation of closed-loop micelles for dimeric and trimeric surfactants. Wu et al. performed large scale coarse-grained molecular dynamics simulations to study self-assembling process of 12-S-12 gemini surfactants with  $S = 6, 12, \text{ and } 20$  [8]. In their study, free gemini molecules aggregate into the oligomers (premicelles) and then these small clusters merge with each other to form larger clusters such as vesicles.

The first Monte Carlo simulation study on the self-assembling process of lattice gemini amphiphiles goes back to the work of Bernardes [9]. In later work, the author has tested effects of chain rigidity on the aggregate shapes [10]. Maiti and Chowdhury carried out Monte Carlo simulation

similar to the Bernardes' model and investigated three factors containing length of spacer, length of tail, and bending rigidity of spacer and/or tails on the critical micelle concentration of a lattice gemini amphiphile [11, 12]. They have shown, in agreement to the experimental results, their simulated CMC reached a maximum at a certain length of spacer. In later work, Maiti and his coworkers studied cross-linking between one-tailed micelles by gemini surfactants [13]. Layn et al. have used lattice Monte Carlo and quasichemical theory to investigate phase behavior of simple gemini surfactant with only hydrophilic spacer [14]. They have studied effects of oil length, surfactant rigidity, and temperature on the phase behavior. Recently, Davis and Panagiotopoulos have used grand canonical Monte Carlo simulation of mixture of one-tailed and double-tailed nonionic amphiphile to study the effect of addition of a micellizing amphiphile on the behavior of another phase separating amphiphile [15]. Very recently, Jackson et al. investigated assembling processes of two-headed linear surfactants by two dimensional lattice Monte Carlo simulations [16].

In the present work, we have compared self-assembling process for two lattice amphiphiles with the same head to tail ratio. Both of amphiphiles are symmetrical. Dimeric chains are double of single chains that connected head-to-head. In this work, we have not considered any extra hydrophilic or hydrophobic beads between heads as a spacer group to investigate how aggregates are formed without spacer groups. Meanwhile, different thermodynamic behaviors are compared including CMC, pre-micellar concentration, size distribution, polydispersity, and aggregation number. It is shown that transition points in graphs of polydispersity, aggregation number, and pre-micellar concentration, match with the CMC point in graph of monomer concentration.

## 2. Model

The model is based on the hydrophobic interactions as a main driving force of micellization process. Details of the model can be found in previous studies [17, 18]. Here, we only summarize it. A simple cubic lattice with the size of  $80 \times 80 \times 80$ ,  $100 \times 100 \times 100$ , or  $200 \times 200 \times 200$  is used as a box of simulation. In all simulations, a water molecule occupies only a single lattice site. Surfactant molecules are modeled as short chains on the lattice. One-tailed and double-tailed surfactants are modeled by  $H_iT_j$  and  $(H_iT_j)_2$  or  $T_jH_{2i}T_j$ , respectively. "H" and "T" denote a head and a tail, respectively. The integers "i" and "j" denote the length of head and tail parts, respectively. In this study, symmetrical monomeric and dimeric surfactants with  $i = j = 3$  are considered. The structures of a monomeric and a dimeric lattice surfactant have been shown in Figure 1. A lattice bead interacts only with its six nearest neighbor beads, thus the coordination number is equal to six ( $z = 6$ ). Periodic boundary conditions and excluded volumes are used to mimic the box of simulation as the bulk of solution. Canonical ensemble with the constants of  $N$ ,  $V$ , and  $T$  is used

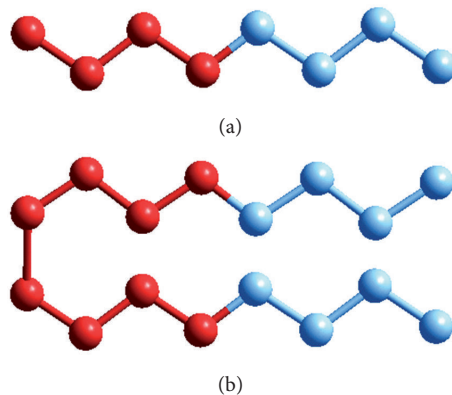


FIGURE 1: Structure of (a) monomeric and (b) dimeric studied lattice surfactants. Red beads are heads and light blue beads are tails.

for ensemble-averaging. The potential model is as previous and defined as follows [17, 18]:

$$\frac{E}{k_B T} = \frac{\varepsilon}{k_B T} (n_{T,W} + n_{T,H}), \quad (1)$$

where  $n_{T,W}$  and  $n_{T,H}$  are the numbers of tail-water and tail-head pairs, respectively, and  $\varepsilon/(k_B T)$  is the dimensionless interactions parameter. In the present work, we have set  $\varepsilon/(k_B T) = 0.7$ . Previously, it has been shown that this value of interaction parameter gives rise to micellization [18]. Only hydrophobicity of surfactant molecules, as a main characteristic of amphiphile molecules, is considered in the potential model.

We have used reptation [19] and configurational bias Monte Carlo [20] algorithms to move surfactant molecules. Our simulations are based on the standard Metropolis algorithm in which the probability of  $P = \text{Min}(1, \exp(-\beta\Delta E))$  for reptation and  $P = \text{Min}(1, (W(n))/(W(o))e^{-\beta\Delta E})$  for configurational bias Monte Carlo moves are used, where  $\Delta E$  is the difference of the total energy between new trial and old configurations,  $\beta$  is  $1/(k_B T)$ , and  $P$  is the probability by which new trial configuration is accepted. The Rosenbluth weight ( $W$ ) is number of solvent sites ( $z_s(i)$ ) around the next bead to be removed or regrown.

Source codes were written in Fortran77 language, and compiled with intel Fortran Composer Xe compiler under the Centos linux. Nearly  $10^{11}$  moves have been used to equilibrate initial configurations, and  $2 \times 10^{11}$  moves were used for ensemble averaging. 2000 snapshots have been used for ensemble averaging to get smooth graphs.

**2.1. Definition of Parameters.** Two kinds of concentration have been defined: total volume fraction ( $V_{\text{tot}}$ ) and cluster number density ( $X_n$ ) with aggregation number  $n$  ( $n \geq 1$ ),

$$V_{\text{tot}} = \frac{\text{total sites of surfactant molecules}}{\text{total sites of lattice}}, \quad (2)$$

$$X_n = \frac{\text{total number of molecules in cluster}}{\text{total sites of the lattice}}.$$

According to  $X_n$ , concentration of free surfactant molecules is defined as:

$$X_1 = \frac{\text{total number of free molecules}}{\text{total sites of the lattice}}. \quad (3)$$

A surfactant is considered as a free molecule whenever all nearest neighbors of its tail sites are water molecules. Two surfactant molecules are considered to be in the same cluster if at least one tail site of the first molecule is the nearest neighbor of any tail site of the second molecule. Premicelles are small aggregates, usually with aggregation number less than ten [21]. Premicellar concentration is defined as  $\sum_{n=2}^{10} nX_n$ . Polydispersity is defined as  $I_p = N_w/N_n$ , where  $N_n$  is number-averaged aggregation number, and  $N_w$  is weight-averaged aggregation number.  $N_n$  and  $N_w$  are defined as follows:

$$N_n = \frac{\sum_{n=2}^{n_{\max}} nX_n}{\sum_{n=2}^{n_{\max}} X_n}, \quad (4)$$

$$N_w = \frac{\sum_{n=2}^{n_{\max}} n^2 X_n}{\sum_{n=2}^{n_{\max}} nX_n}.$$

A free molecule is not considered in the above summation, and  $n_{\max}$  is the maximum aggregation number in all of the snapshots considered in the ensemble averaging.

### 3. Results and Discussion

Surfactant solutions may be classified into three concentration ranges: premicellar, micellar, and phase/shape transition ranges. For dimeric surfactants, almost all previous studies focused on the micellar and/or phase/shape transition ranges. In this paper, properties of single and double chain surfactant solution in three above ranges are reviewed and compared.

Premicelles are aggregates with small aggregation number. Often, clusters with aggregation number less or equal to ten are referred as premicelles [21]. Figures 2 and 3 show the premicellar concentration of single and double chain surfactants. The graphs show that the concentration of premicelles for single chain surfactant is higher than nearly tenfold of that of dimeric one. At first, premicellar concentration increases in sigmoidal fashion up to a maximal value, and then relaxes to the lower values. This relaxation is much slower for dimeric chain compared to monomeric surfactant. This behavior is very similar to the graphs of CMC determination (Figures 4 and 5).

The second range belongs to the micellar phase. The concentration at which micelles begin to be formed is named as critical micelle concentration (CMC). Various definitions for the CMC have been used in the literature. We have defined CMC as a surfactant concentration at which free molecules reach maximal value. Figures 4 and 5 show CMC graphs for both single and double chain surfactants. On the basis of the definition, CMC for  $H_3T_3$  is nearly equal to  $V_{\text{tot}} = 0.06$ , and for  $(H_3T_3)_2$  is equal to  $V_{\text{tot}} = 0.014$ . CMC of dimeric surfactant is much lower than monomeric one. As is clear from above figures, premicellar behaviors are similar to the free surfactant concentration changes.

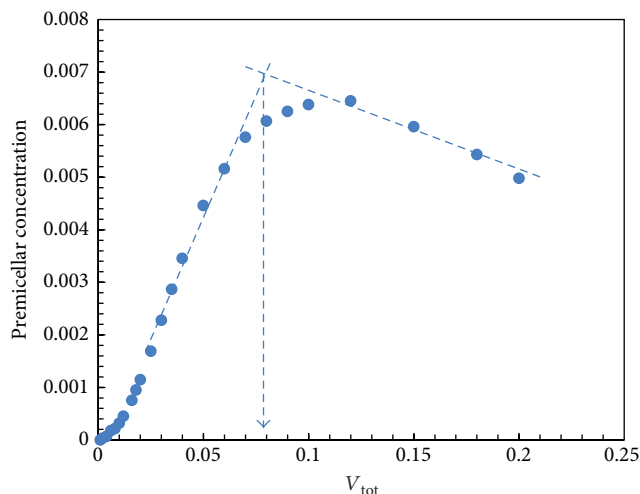


FIGURE 2: Premicellar number density (summation of  $nX_n$  with  $2 \leq n \leq 10$ ) versus total volume fraction ( $V_{\text{tot}}$ ) of surfactant. The graph belongs to  $H_3T_3$  as a single chain surfactant. Maximum concentration is found near to CMC. After CMC, premicelles reduce rapidly.

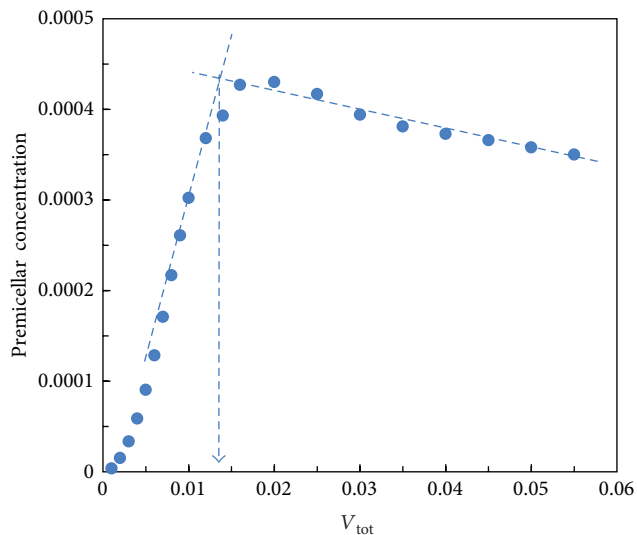


FIGURE 3: Premicellar number density (summation of  $nX_n$  with  $2 \leq n \leq 10$ ) versus total volume fraction ( $V_{\text{tot}}$ ) of surfactant. The graph belongs to  $(H_3T_3)_2$  as a double chain surfactant. Maximum concentration is found near to CMC. After CMC, premicelles remain nearly constant.

At CMC, premicelles reach maximal values, and at higher concentration small aggregates grow and form larger clusters. After CMC, premicellar concentration reduces and system tends to be more monodispersed. Polydispersity is defined as the ratio of weight-averaged aggregation number ( $N_w$ ) to number-averaged aggregation number ( $N_n$ ). Figures 6 and 7 show polydispersity changes for single and double chain surfactants. Data show that for both systems there is a break point on the curve of polydispersity. This occurs at

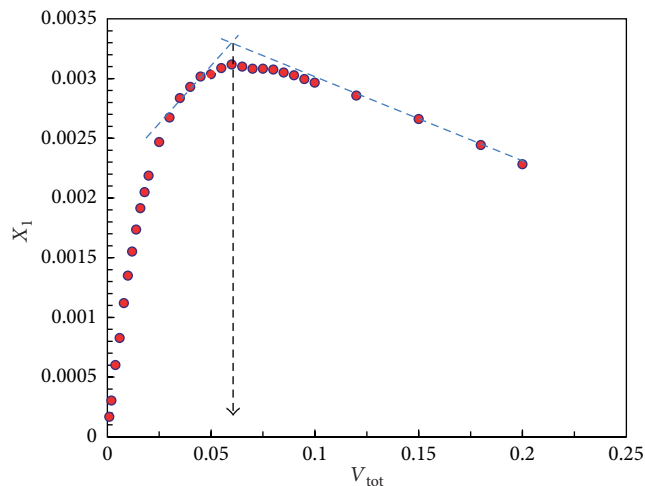


FIGURE 4: Free surfactant molecule number density ( $X_1$ ) versus total volume fraction ( $V_{tot}$ ). The graph belongs to  $H_3T_3$  as a single chain surfactant. This graph is often used for determination of the CMC.

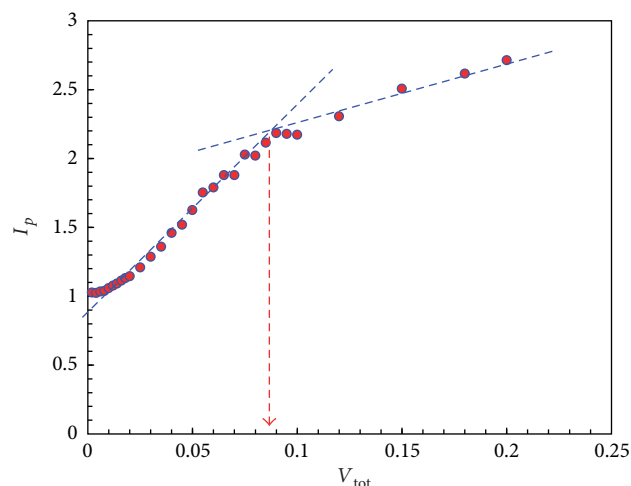


FIGURE 6: Polydispersity ( $I_p$ ) versus total volume fraction ( $V_{tot}$ ) for  $H_3T_3$  as a single chain surfactant. From this graph CMC is estimated by 0.09. The slope of the graph reduces after CMC.

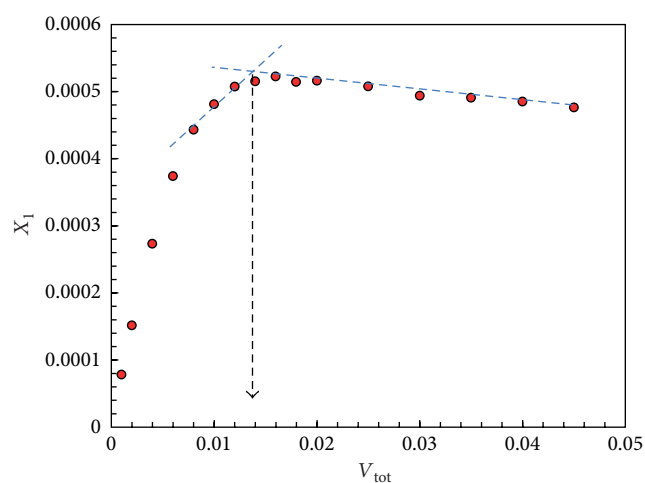


FIGURE 5: Free surfactant molecule number density ( $X_1$ ) versus total volume fraction ( $V_{tot}$ ). The graph belongs to  $(H_3T_3)_2$  as a double chain surfactant. This graph is often used for determination of the CMC.

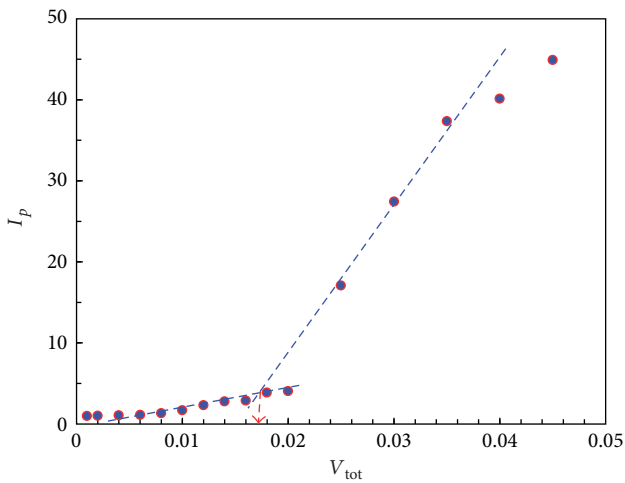


FIGURE 7: Polydispersity ( $I_p$ ) versus total volume fraction ( $V_{tot}$ ) for  $(H_3T_3)_2$  as a double chain surfactant. From this graph CMC is estimated nearly 0.02. The slope of the graph increases after CMC.

volume fractions of 0.09 and 0.018 for  $H_3T_3$  and  $(H_3T_3)_2$ , respectively.

Another important issue in the micellar phase is about cluster size distribution. It is believed that CMC relates to the horizontal inflection point at cluster size distribution [22]. Figures 8 and 9 show the inflection point at cluster size distribution for single and double chain surfactants, respectively. The inflection point occurs at concentration of 0.1 and 0.015 for single and double chain surfactant, respectively. Comparing these values with the critical points of Figures 2 to 7 (which can be named as their CMCs), it shows that there is a close connection between inflection points in above figures (Figures 8 and 9) and critical points of Figure 2 to Figure 7, that is, the inflection points can be

considered as CMC points. Similarity of these critical values shows that the idea of [22] is correct.

The third concentration range of surfactant systems contains shape/phase transition. In some papers, additional peaks in cluster size distribution have been interpreted as a clue for shape/phase transition in surfactant systems [23]. In our previous paper, we have proved that a true simulation should have one peak in cluster size distribution [18]. Figure 10 shows the cluster size distribution for double chain surfactant. It shows that the peak in the distribution shifts to higher values at higher concentration. We have repeated simulation for greater box  $100 \times 100 \times 100$  to test the size effect. Figure 11 shows the results for greater box. There are two important points on this figure. First, as for smaller box, peak shifts to larger values, and second, for greater lattice at

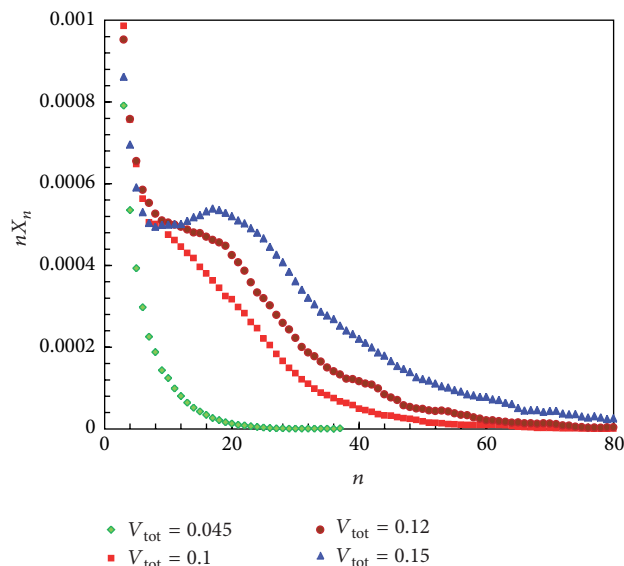


FIGURE 8: Cluster size distribution ( $nX_n$ ) for the micellar range of concentration of  $H_3T_3$  as a single chain surfactant. Inflection point occurs at  $V_{tot} = 0.1$  which agree with CMC of  $H_3T_3$ .

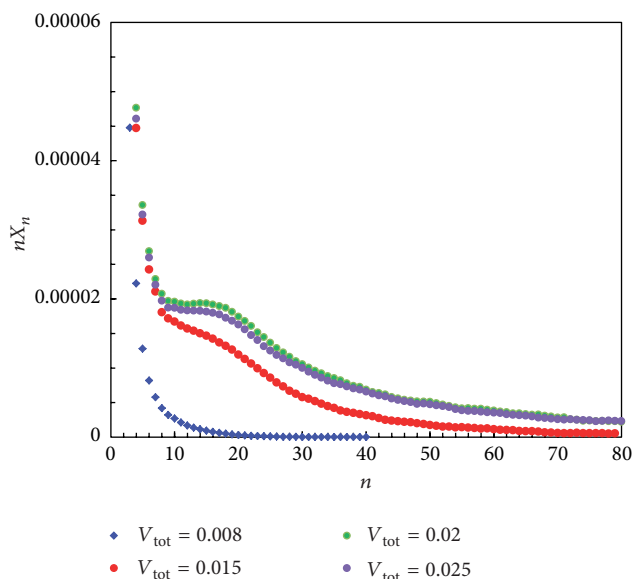


FIGURE 9: Cluster size distribution ( $nX_n$ ) for the micellar range of concentration of  $(H_3T_3)_2$  as a double chain surfactant. Inflection point occurs at  $V_{tot} = 0.016$  which agree with CMC of  $(H_3T_3)_2$ .

a certain concentration, peak appeared at higher aggregation number. It can be concluded that for double chain surfactant, with enlarging the box to infinite, aggregation number becomes very large, that is, phase separation occurs. On the other hand, for  $H_3T_3$ , even at high concentration of 0.15, there is not any shift in the position of peak. Another clue for this subject is tracing weight-average aggregation number ( $N_w$ ). Figures 12 and 13 show  $N_w$  for single and double chain surfactants. As is clear for double chain surfactant,  $N_w$  increases rapidly.

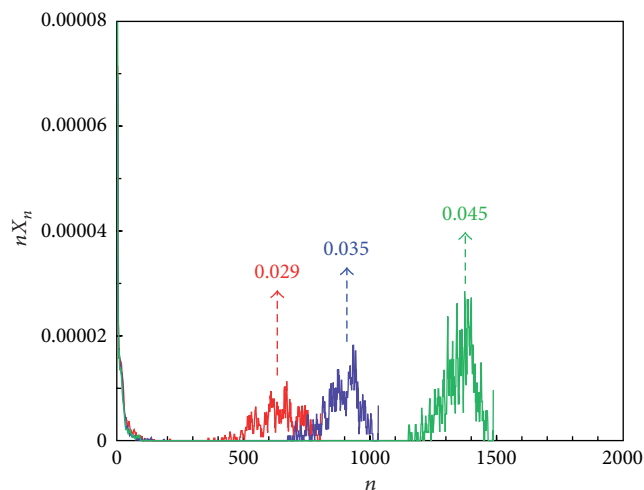


FIGURE 10: Cluster size distribution ( $nX_n$ ) for the phase transition range of concentration of  $(H_3T_3)_2$  as a double chain surfactant. Peak of distribution shifts to higher values of aggregation number. Lattice size is  $80 \times 80 \times 80$ .

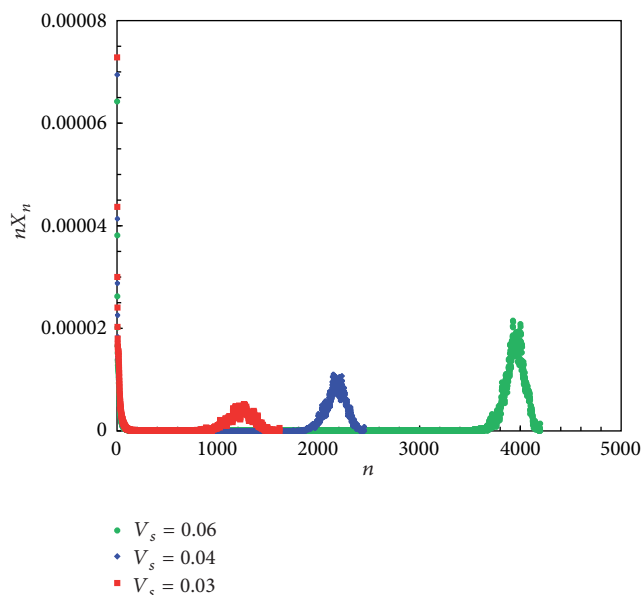


FIGURE 11: Same as Figure 9 but for  $100 \times 100 \times 100$  lattice size.

The ratio of head to tail for both single and double chain surfactants is the same. Each dimeric molecule is equal to two single chain molecules, so, it is expected that the properties of single chain molecule to be similar to double chain at twice concentration of dimeric molecule; however, this is not the case. Looking at the structure of aggregates of double chain molecule help us to understand the differences. Figure 14 shows the structures of aggregates at concentrations of 0.016, 0.02, and 0.07. The figure shows how head groups connect separate micelles. At high concentration we encounter with large bolaform aggregates in which spacer groups play a connection role. Figure 15 shows snapshot of box of simulation at volume fraction of 0.06. It shows that

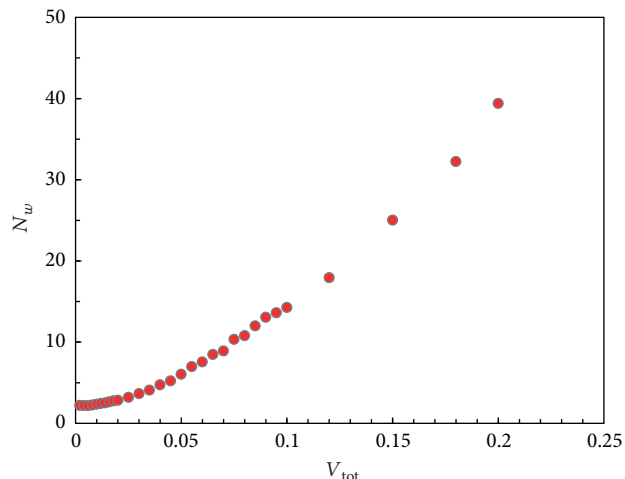


FIGURE 12: Weight-average aggregation number ( $N_w$ ) for  $H_3T_3$  as a single chain surfactant. Aggregation number increases slowly.

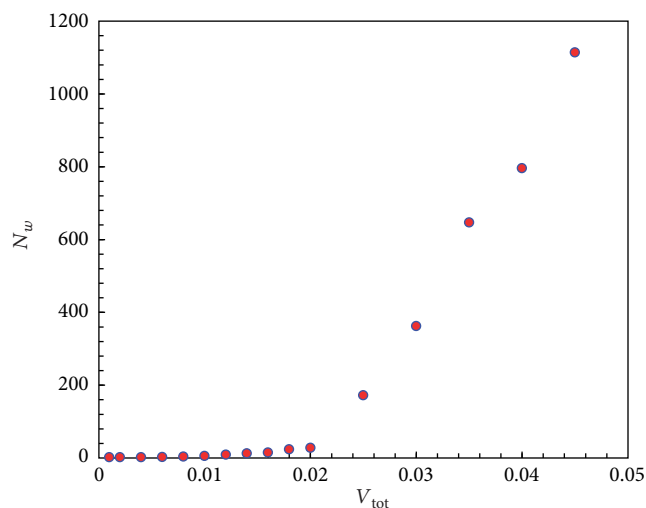


FIGURE 13: Weight-average aggregation number ( $N_w$ ) for  $(H_3T_3)_2$  as a double chain surfactant. Aggregation number increases very rapidly.

very large aggregates are formed at nearly low concentration. All results show that to reduce dramatically CMC or increase aggregation number, it is sufficient that two single chains are connected from head positions, and it is not necessary to introduce any extra hydrophobic or hydrophilic spacer groups.

#### 4. Conclusion

In this paper, we have chosen very similar single and double chain surfactant with the same head to tail ratio. Each double chain molecule equals to two single chains in number of heads and tails. To build a dimeric chain from two single chains, heads are connected without introducing any hydrophobic or hydrophilic spacer groups. It is shown that

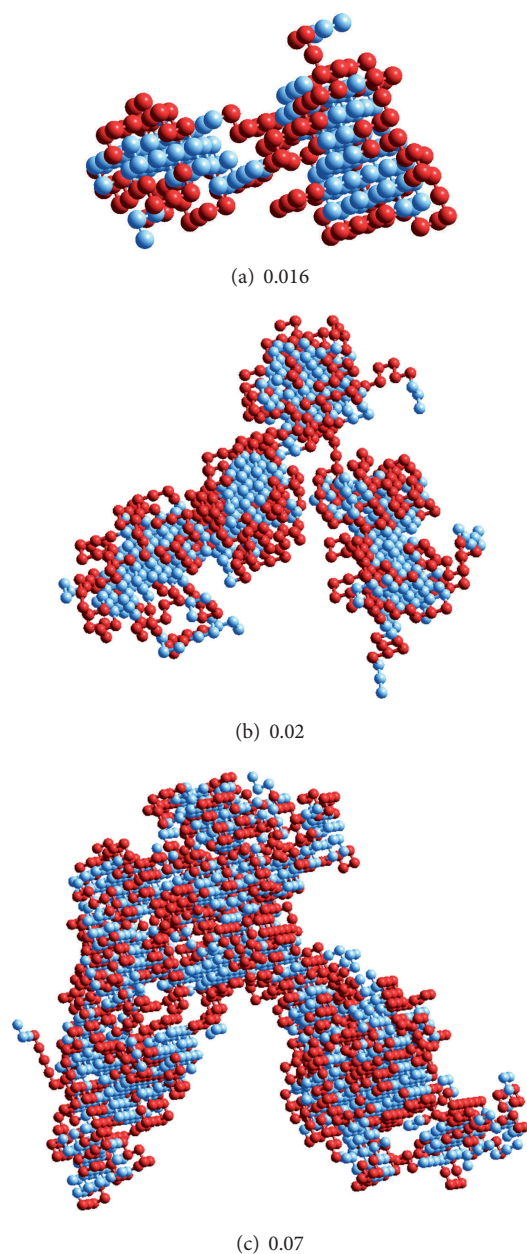


FIGURE 14: Structure of aggregates of  $(H_3T_3)_2$  at volume fractions of (a) 0.016, (b) 0.02, and (c) 0.07. The structures show that head groups of the molecule (green beads) play a connector role to join separate micelles. At high concentrations bolaform micelles are formed.

the properties of double chain surfactant are very different from single chain surfactant. Its CMC is nearly tenfold lower than the CMC of single chain molecule; its aggregation number is greater than 30 times of aggregation number of single chain surfactant, and the cluster size distribution shows a kind of phase transition that is not present for single chains. It has been shown that head groups of double chain surfactants as spacer groups are the main factor for these differences. They play a connector role by which separate micelle are joined to each other. In addition, results show that CMC can be estimated from free monomer concentration,

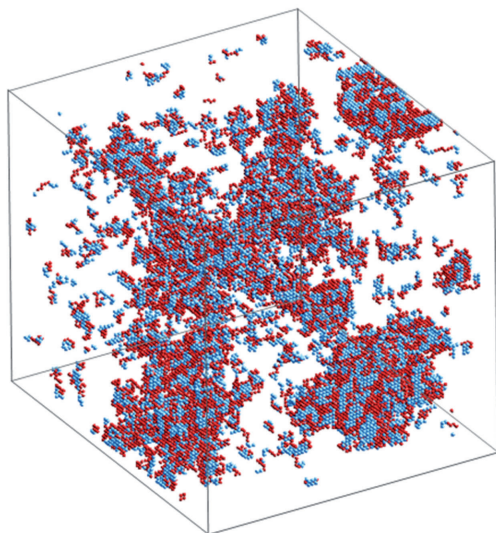


FIGURE 15: Snapshot of box of simulation of  $(H_3T_3)_2$  at volume fraction of 0.06.

premicellar concentration, aggregation number, and polydispersity graphs. As a main result, it is shown that how without introducing extra hydrophobic or hydrophilic spacer groups, dimeric amphiphiles behave similar to gemini surfactants.

## References

- [1] Q. Huo, R. Leon, P. M. Petroff, and G. D. Stucky, "Mesostucture design with gemini surfactants: supercage formation in a three-dimensional hexagonal array," *Science*, vol. 268, no. 5215, pp. 1324–1327, 1995.
- [2] R. Zana and J. Xia, *Gemini Surfactants: Synthesis, Interfacial and Solution-Phase Behavior, and Applications*, Marcel Dekker, New York, NY, USA, 2004.
- [3] R. Zana and Y. Talmon, "Dependence of aggregate morphology on structure of dimeric surfactants," *Nature*, vol. 362, no. 6417, pp. 228–230, 1993.
- [4] D. Danino, Y. Talmon, H. Levy, G. Beinert, and R. Zana, "Branched threadlike micelles in an aqueous solution of a trimeric surfactant," *Science*, vol. 269, no. 5229, pp. 1420–1421, 1995.
- [5] S. Karaborni, K. Esselink, P. A. J. Hilbers et al., "Simulating the self-assembly of gemini (dimeric) surfactants," *Science*, vol. 266, no. 5183, pp. 254–256, 1994.
- [6] B. Smit, P. A. J. Hilbers, K. Esselink, L. A. M. Rupert, N. M. Van Os, and A. G. Schlijper, "Computer simulations of a water/oil interface in the presence of micelles," *Nature*, vol. 348, no. 6302, pp. 624–625, 1990.
- [7] P. K. Maiti, Y. Lansac, M. A. Glaser, N. A. Clark, and Y. Rouault, "Self-assembly in surfactant oligomers: a coarse-grained description through molecular dynamics simulations," *Langmuir*, vol. 18, no. 5, pp. 1908–1918, 2002.
- [8] R. Wu, M. Deng, B. Kong, and X. Yang, "Coarse-grained molecular dynamics simulation of ammonium surfactant self-assemblies: micelles and vesicles," *Journal of Physical Chemistry B*, vol. 113, no. 45, pp. 15010–15016, 2009.
- [9] A. T. Bernardes, "Monte Carlo simulation of vesicle self-organisation," *Journal de Physique II*, vol. 6, no. 2, pp. 169–174, 1996.
- [10] A. T. Bernardes, "Computer simulations of spontaneous vesicle formation," *Langmuir*, vol. 12, no. 24, pp. 5763–5767, 1996.
- [11] P. K. Maiti and D. Chowdhury, "Micellar aggregates of gemini surfactants: Monte Carlo simulation of a microscopic model," *Europhysics Letters*, vol. 41, no. 2, pp. 183–188, 1998.
- [12] P. K. Maiti and D. Chowdhury, "A microscopic model of gemini surfactants: self-assemblies in water and at air-water interface," *Journal of Chemical Physics*, vol. 109, no. 12, pp. 5126–5133, 1998.
- [13] P. K. Maiti, K. Kremer, O. Flimm, D. Chowdhury, and D. Stauffer, "Cross-linking of micelles by gemini surfactants," *Langmuir*, vol. 16, no. 8, pp. 3784–3790, 2000.
- [14] K. M. Layn, P. G. Debenedetti, and R. K. Prud'homme, "A theoretical study of Gemini surfactant phase behavior," *Journal of Chemical Physics*, vol. 109, no. 13, pp. 5651–5658, 1998.
- [15] J. R. Davis and A. Z. Panagiotopoulos, "Micellization and phase separation in binary amphiphile mixtures," *Molecular Physics*, vol. 107, no. 22, pp. 2359–2366, 2009.
- [16] D. R. Jackson, A. Mohareb, J. MacNeil, M. S. G. Razul, D. G. Marangoni, and P. H. Poole, "Simulations of a lattice model of two-headed linear amphiphiles: influence of amphiphile asymmetry," *Journal of Chemical Physics*, vol. 134, no. 20, Article ID 204503, 2011.
- [17] R. Behjatmanesh-Ardakani, "Polymer-centered theory in comparison with surfactant-centered theory: a lattice Monte Carlo study," *Journal of Chemical Physics*, vol. 122, no. 20, Article ID 204903, pp. 1–5, 2005.
- [18] R. Behjatmanesh-Ardakani, "Additional peaks in the cluster size distribution of amphiphile + water systems: a clue for shape/phase transition or statistical uncertainty," *Theoretical Chemistry Accounts*, vol. 118, no. 4, pp. 799–805, 2007.
- [19] P. G. De Gennes, "Reptation of a polymer chain in the presence of fixed obstacles," *The Journal of Chemical Physics*, vol. 55, no. 2, pp. 572–579, 1971.
- [20] J. I. Siepmann and D. Frenkel, "Configurational bias Monte Carlo: a new sampling scheme for flexible chains," *Molecular Physics*, vol. 75, pp. 59–70, 1992.
- [21] S. K. Talsania, Y. Wang, R. Rajagopalan, and K. K. Mohanty, "Monte Carlo simulations for micellar encapsulation," *Journal of Colloid and Interface Science*, vol. 190, no. 1, pp. 92–103, 1997.
- [22] E. Ruckenstein and R. Nagarajan, "Critical micelle concentration and the transition point for micellar size distribution," *Journal of Physical Chemistry*, vol. 85, no. 20, pp. 3010–3014, 1981.
- [23] M. Lísal, C. K. Hall, K. E. Gubbins, and A. Z. Panagiotopoulos, "Self-assembly of surfactants in a supercritical solvent from lattice Monte Carlo simulations," *Journal of Chemical Physics*, vol. 116, no. 3, pp. 1171–1184, 2002.

## Research Article

# Adsorption of Trinitrotoluene on a MgO(001) Surface Including Surface Relaxation Effects

Thiago Guerra<sup>1</sup> and Itamar Borges Jr.<sup>1,2</sup>

<sup>1</sup>Programa de Pós-Graduação em Engenharia de Defesa, Instituto Militar de Engenharia, 80, 22290-270 Rio de Janeiro, RJ, Brazil

<sup>2</sup>Departamento de Química, Instituto Militar de Engenharia, Praça General Tibúrcio, 80, 22290-270 Rio de Janeiro, RJ, Brazil

Correspondence should be addressed to Itamar Borges Jr.; [itamar@ime.eb.br](mailto:itamar@ime.eb.br)

Received 28 June 2012; Revised 31 July 2012; Accepted 31 July 2012

Academic Editor: Cristiano R. W. Guimarães

Copyright © 2013 T. Guerra and I. Borges Jr. This is an open access article distributed under the Creative Commons Attribution License, which permits unrestricted use, distribution, and reproduction in any medium, provided the original work is properly cited.

A thorough investigation of 2,4,6-trinitrotoluene (TNT) adsorption on a MgO(001) surface was carried out using density functional theory (DFT) combined with periodic boundary conditions. Four different initial orientations of the TNT molecule, adsorbed on two different representations of the MgO(001) surface, were investigated. In the first surface representation, there were two fixed layers of atoms and in the second the surface had three layers, with the uppermost fully relaxed in geometry optimizations. Electron density difference maps for each case were computed and provided a detailed picture of the interactions. The results showed a physical adsorption process for both surface representations. In the most favorable situation—TNT adsorbed on the surface with three layers—the computed adsorption energy was  $-9.89$  kcal/mol. The importance of allowing the uppermost layer of the surface to fully relax upon molecular desorption was shown.

## 1. Introduction

Explosives and propellants—energetic materials—have a large spectrum of military and civilian applications. Investigations of these materials involve complex physical-chemical processes and experimental work can be dangerous. For these reasons, theoretical work on these substances can be especially valuable.

We have been working on several aspects of energetic materials employing a variety of theoretical chemistry/molecular modeling tools. We have focused on excited states [1–4], decomposition processes [5], and sensitivity properties [6, 7]. Concerning catalytic studies, we studied a variety of processes on oxides [8] and layered hydroxides [9, 10]. In this work, we examine a possible role of magnesium oxides in the decomposition of a nitroaromatic explosive, TNT (2,4,6-trinitrotoluene).

TNT (2,4,6-trinitrotoluene) is an explosive material widely used for military and civilian purposes [11]. As a result of widespread use, residual TNT in both soil and groundwater has been detected [12, 13]. In particular, the presence of TNT and its degradation products in aquatic environment

was associated with adverse impacts on biological receptors and communities [13, 14]. TNT was listed as a significant pollutant to public health and aquatic life.

TNT-contaminated water can be treated by various methods, including activated carbon adsorption [15, 16], supercritical water oxidation [17], Fenton reagent oxidation [18], and photocatalytic oxidation [19, 20]. In spite of their usefulness for TNT degradation, residual products from these treatments are still potentially harmful.

Magnesium oxide (MgO), also named periclase, is an important mineral with rock-salt structure readily cleaving along the (001) direction, the most stable surface. After cleavage, the terminated surface exposes equal numbers of cations and anions. There is only a slight reconstruction on clean MgO(001) surface, an rumpling of the topmost surface atoms due to different magnitudes of mutual induced polarizations of the  $Mg^{2+}$  and  $O^{2-}$  ions [21]. In heterogeneous catalysis, several reactions take advantage of acid-basic properties of the MgO surface [8, 22].

DFT cluster models and periodic boundary condition calculations indicated that alkaline oxides such as CaO and BaO chemisorb  $NO_x$  species [23–25]. Moreover, adsorption

of  $\text{NO}_2/\text{NO}_2$ ,  $\text{NO}/\text{NO}_2$ , or  $\text{NO}/\text{NO}$  molecular pairs was studied, and it was found that a cooperative effect contributes to increase adsorption energy of the pair [26–28]. Although  $\text{NO}$  and  $\text{NO}_2$  are both radicals, thereby being highly reactive, considering the large availability of magnesium oxides for catalytic applications, we could ask if the TNT molecule, having three nitro groups, could favorably adsorb on a  $\text{MgO}$  (001) surface through a cooperative effect thus leading to possible deactivation. Answer to this question was the main motivation of the present work. We also investigated the effect of different surface models in the adsorption.

## 2. Theoretical Methods

We used the density functional theory (DFT) [29, 30] combined with periodic boundary conditions and the PW91 generalized gradient approximation (GGA) exchange-correlation functional of Perdew and Wang [31]. The open-source PWSCF package (Quantum-ESPRESSO is a community project for high-quality quantum-simulation software, based on density-functional theory and coordinated by Paolo Giannozzi. See <http://www.quantum-espresso.org> and <http://www.pwscf.org>), employed for all calculations, uses pseudopotentials to describe core electrons, periodic boundary conditions, and plane-wave basis sets.

The convergence criterion for the electronic self-consistent cycle was fixed to  $10^{-7}$  eV per cell. The Kohn-Sham orbitals were expanded in a plane wave basis set with a maximum kinetic energy (ecut) of 40 Ry (544 eV). The Fermi energy was calculated using the Gaussian broadening technique with a smearing parameter of 0.005 Ry. We used the Vanderbilt [32] ultrasoft pseudopotentials for the C, H, O, N, and Mg atoms. For Mg atoms we used a pseudocore scheme including the 2p electrons in the valence shell. The electron density was computed at the  $\Gamma$  point in the first Brillouin zone of the super cell [33].

The  $\text{MgO}$  primitive cell has two atoms and the following original parameters:  $a = b = c = 4.212 \text{ \AA}$ ,  $\alpha = \beta = \gamma = 90^\circ$ . The starting geometry for optimization of the clean  $\text{MgO}$  surface was the experimental bulk geometry [34] with  $\text{Mg-O}$  distances equal  $2.106 \text{ \AA}$ . After geometry optimization, the  $\text{Mg-O}$  distance converged to  $2.104 \text{ \AA}$ , and this value was used for the reported calculations. The construction of the supercells employed in the calculations was based on this optimized structure. We used periodic slab geometries consisting of three  $\text{MgO}$  layers with a  $5 \times 5$  super-cell (a total of 50 atoms per layer with 25 Mg and 25 O atoms); a vacuum layer of  $15 \text{ \AA}$  was added in the “z” direction—this value was found to eliminate spurious interactions between surface replicas generated by the periodic boundary conditions. The supercell angles had the same values of the  $\text{MgO}$  experimental geometry. For all calculated structures, the super-cell angles and lattice parameters were kept fixed for the two-layer surface, and when a third layer in the uppermost position was added, it was allowed to fully relax along with the adsorbed molecule. For all structures, the equilibrium positions of the nuclei were found by minimizing the total energy.

For all initial TNT geometries, the molecule was placed in a certain orientation above the top face of the super-cell. Four initial adsorption positions were considered to converge the system to local minima, and for all of them, the TNT molecule starting orientation was laid always parallel to the  $\text{MgO}$  surface. The TNT starting positions were

*Position 1.* The oxygen atoms of two nitro groups were placed directly above surface magnesium atoms;

*Position 2.* The molecule was rotated  $30^\circ$  with respect to the previous position;

*Position 3.* The molecule was rotated  $60^\circ$  with respect to Position 1 of the molecule;

*Position 4.* At this position, the molecule was positioned in such way that oxygen atoms of one nitro group of the molecule faced the magnesium atoms of the  $\text{MgO}$  surface.

In order to analyze the contribution of the additional relaxed layer, we carried out two types of calculations. In the first, we optimized the geometry of the adsorbed TNT on a surface containing only two atomic layers, both fixed in bulk positions and not optimized. In the other calculations, we added a third atomic layer which was allowed to fully relax in the optimization process while the other two were kept frozen at their bulk positions.

We relaxed exclusively the uppermost layer in the three layer surface model because only the geometric parameters of this monolayer are affected in molecular adsorption processes and suffer reconstruction. According to low-energy electron diffraction surface experiments, the best model for this surface corresponds to an inward relaxation of no more than 2.5% of the lattice constant in the superficial monolayer and a rumpling of less than about 2% of the  $\text{O}_2^-$  ions compared to the  $\text{Mg}_2^+$  ions [35]. Therefore, our three-layer model is quite realistic, as we have shown before [8].

The adsorption energy ( $E_{\text{ads}}$ ), considering only electronic contributions, was computed according to the total energy difference:

$$E_{\text{ads}} = E_{T(\text{TNT}/\text{MgO})} - [E_{\text{MgO}} + E_{\text{TNT}}]. \quad (1)$$

The electron density difference plots were calculated according to the expression:

$$\rho_{\text{diff}}(\mathbf{r}) = \rho_{\text{TNT}/\text{surf}}(\mathbf{r}) - \rho_{\text{surf}}(\mathbf{r}) - \rho_{\text{TNT}}(\mathbf{r}). \quad (2)$$

Pictures constructed according to the previous equation depict regions of electronic charge accumulation and depletion, thereby providing a visualization of interactions between the atoms of the system. The electronic density difference  $\rho_{\text{diff}}(\mathbf{r})$  was calculated for a regularly spaced set of points in the three-dimensional unitary cell. All points where  $\rho_{\text{diff}}(\mathbf{r}) \geq 0.003 \text{ eV/\AA}^3$  were drawn as red, and points where  $\rho_{\text{diff}}(\mathbf{r}) \leq -0.003 \text{ eV/\AA}^3$  were drawn as blue. Similar electronic density difference pictures can be produced from cluster calculations [5], that is, without using periodic boundary conditions.

It is important to note that calculations were extremely demanding computationally due to the size of the TNT molecule and the super-cell. We are unaware of similar adsorption calculations of a molecule as large as TNT.

### 3. Results and Discussion

**3.1. Geometries and Adsorption Energies.** The optimized geometry of the isolated TNT molecule, starting structure for adsorption calculations, is shown in Figure 1. The C–C ring distances have small differences, the largest one being 0.041 Å between the largest ( $C_2$ – $C_3$ ) and the smallest ( $C_5$ – $C_6$ ). The largest C–C bond distances involve the  $C_2$  carbon bonded to the methyl group—we have shown before that this atom has the largest site dipole value in TNT [7]. The C–N bonds next to  $CH_3$  are larger by 0.032 Å compared to the other C–N bond. Finally, the N–O bonds differ by only 0.003 Å, with an average bond length of 1.236 Å.

Adsorption calculations starting from an upward TNT position for both types of surfaces did not lead to molecular distortion. This starting orientation was by far the most energetically unfavorable situation; thus it will not be further discussed.

Now we discuss TNT adsorption on the MgO surface with two fixed layers. In Position 1 (Figures 2(a) and 2(b)) the undistorted molecule converged to a distance of 3.4 Å from the surface compared to the starting distance (2.3 Å)—this convergence to farther distances happened in all cases (reported distances refer to the atom closest to the surface, which may differ depending on the situation). An  $NO_2$  group was the closest to the surface, thus having the largest interaction. The adsorption distance from Position 2 (Figures 2(c) and 2(d)) is 3.1 Å, but TNT in this case suffered an appreciable distortion. The electron-withdrawing nitro groups deformed distinctly depending on the surface site. Most of the molecule-surface interaction occurs between TNT electronegative oxygen atoms and  $Mg^{2+}$  acid surface sites; TNT oxygen atoms at the same time are repelled by the  $O_2^-$  basic sites. The ring and the  $CH_3$  group were also distorted by the surface interaction.

From Position 3, the molecule adsorbed at a separation distance of 3.3 Å (Figures 2(e) and 2(f)) while from Position 4 adsorbed at 3.2 Å. In both cases, similar to Position 1 adsorption, the molecule almost did not suffer distortion. From calculated electronic adsorption energies, TNT adsorption on the 2-layer surface had the following order of decreased stability: 4 (–5.48 kcal/mol), 1 (–5.38 kcal/mol), 3 (–4.26 kcal/mol) and 2 (–3.07 kcal/mol).

TNT adsorption on the three-layer model surface, with the uppermost fully relaxed in geometry optimizations, had some differences compared to the two-layer case. The converged molecule-surface distances for TNT adsorption on the three-layer surface are akin to the two layer case, with final molecule-surface distances around 3.3 Å.

Adsorption from Position 1 (Figures 3(a) and 3(b)) is rather similar in comparison to the two-layer surface, but with important differences: the molecule adsorbed with the ring more planar and the  $CH_3$  group less distorted, both resembling more the initial geometry. On the other hand, the  $NO_2$  groups showed larger distortion, thus indicating their greater interaction with the first layer of the surface, now allowed to fully relax. For Position 2 adsorption (Figures 3(c) and 3(d)), similar to Position 1, the ring planarity was also maintained, but with the molecular orientation more

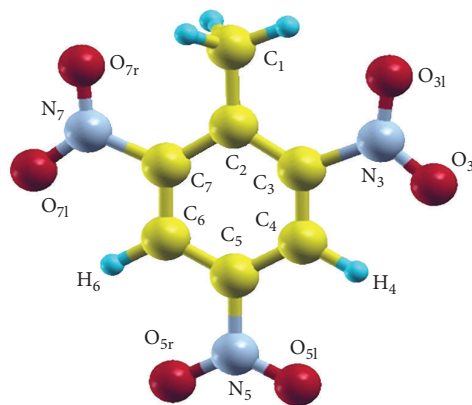


FIGURE 1: DFT-optimized TNT molecular geometry.

parallel to the surface. In comparison to the two-layer case, the nitro groups were less torsioned though the methyl group distorted considerably, the latter effect probably due to a more favorably position of the methyl hydrogen atoms in relation to the  $O^{2-}$  surface atoms.

For Position 3 adsorption on the three-layer surface (Figures 3(e) and 3(f)), the molecule preserved its quite symmetrical geometry: the ring remained planar and the nitro groups next to the methyl group were practically symmetrical, both torsioned in the same direction. The methyl group bent in a way to have one of its hydrogen atoms pointing to an  $O^{2-}$  surface site and the other H atom converged to a position above the ring. Compared to the two-layer case, the methyl group suffered a considerable distortion. Finally, for Position 4 adsorption (Figures 3(g) and 3(h)) both the nitro and methyl groups deformed, the same happening with the carbon ring; three oxygen atoms of distinct nitro groups converged to a position maximizing their interaction with  $Mg^{2+}$  surface sites.

In general, it could be noticed that the largest effect for TNT adsorbed on MgO(001) was the interaction of nitro groups with the surface. The  $NO_2$  group mostly interacting with the surface had the largest C–N distances, a further indication of weakening of these bonds.

The computed electronic adsorption energies for the three layer surface were in order of decreased stability: 1 (–9.80 kcal/mol), 4 (–9.72 kcal/mol), 3 (–9.09 kcal/mol), and 2 (–7.82 kcal/mol). The first three figures are rather similar, virtually identical for starting Positions 1 and 4, all of them characteristic of physisorption. For two-layer surface adsorption, Position 4 was more stable with Position 1 following just the reversed order of the three-layer surface case. Moreover, the adsorption energies for the two-layer surface are about half the values of the three-layer case, thereby displaying the importance of including a third uppermost relaxed layer.

**3.2. Electronic Density Differences for TNT Adsorption on the Three-Layer Surface.** The analysis of the electronic density

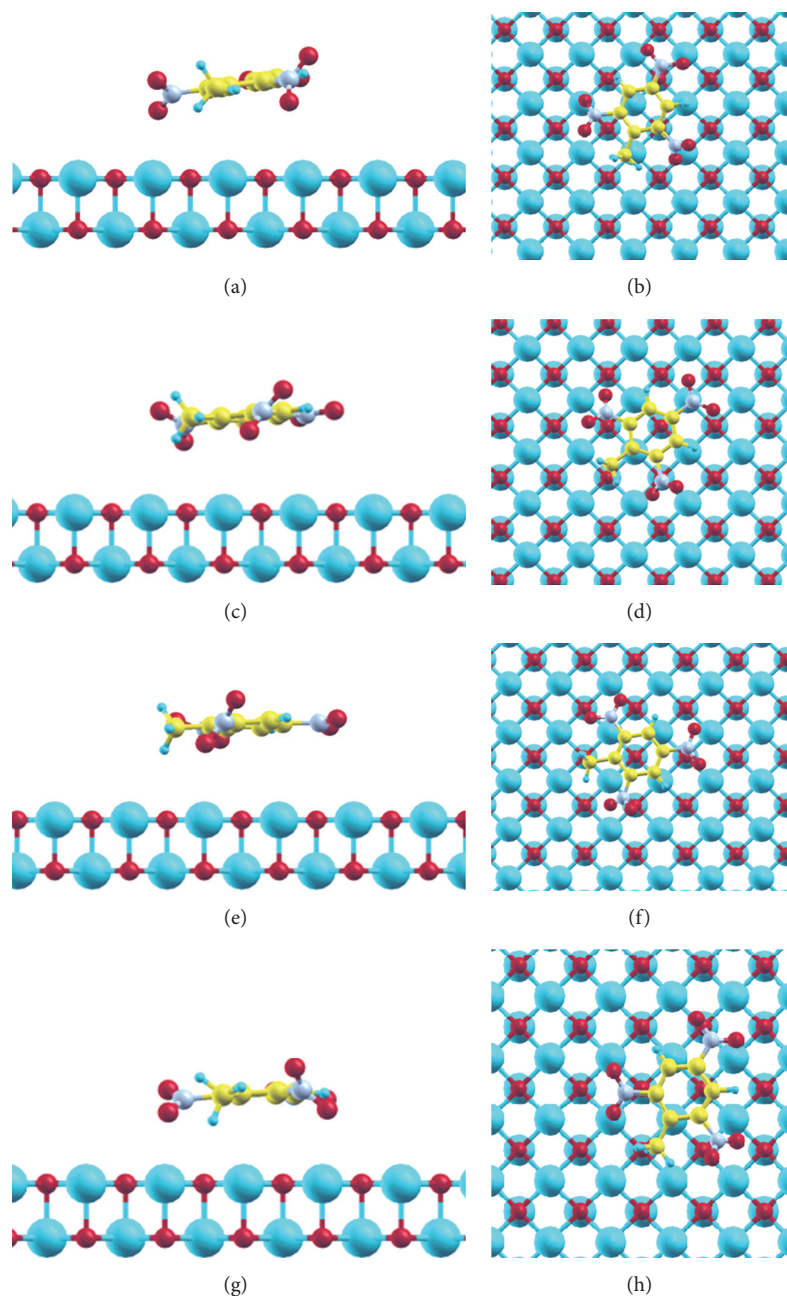


FIGURE 2: Converged geometries of the TNT molecule adsorbed on the MgO(001) surface with two fixed layers. (a) side view and (b) up view of Position 1; (c) Side view and (d) up view of Position 2; (e) side view and (f) up view of Position 3; (g) side view and (h) up view of Position 4.

difference provides a detailed picture of interactions in the adsorption process.

For Position 1 adsorption (Figure 4(a)), the most favorable energetically for adsorption on the three-layer surface, there is a molecular polarization induced by the surface, present in all TNT atoms but with electron accumulation concentrated on the neighborhood of the electron-withdrawing nitro groups and electron depletion below the ring. On the other hand, the TNT molecule considerably polarized the surface, especially the first layer close to the molecule,

thus depleting the surface of electrons. The surface was also similarly polarized for the other three adsorption positions.

In Position 2 (Figure 4(b)), the molecule is rather parallel to the surface and all TNT atoms are polarized. In contrast to Position 1, there is in Position 2 adsorption a remarkable electron accumulation at the top of the atoms, farther from the surface. Below the ring there is considerable electron depletion and, in contrast with Position 1, electron accumulation below the ring, closer to the surface. The strongest interactions, indicated by charge accumulation, are localized

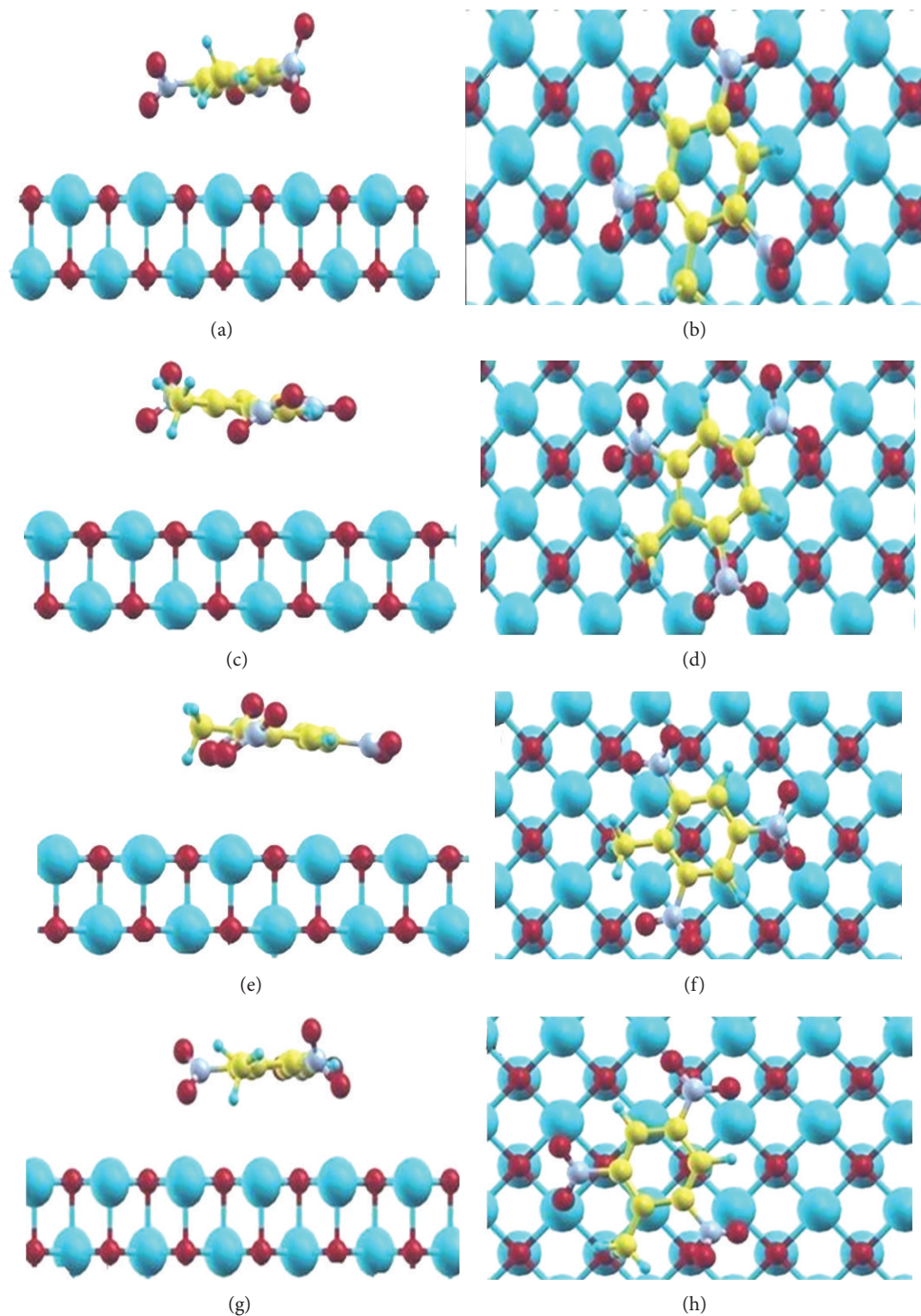


FIGURE 3: Converged geometries of the TNT molecule above the MgO(001) surface: three layer surface, uppermost layer fully relaxed. (a) side view and (b) up view of position 1; (c) side view and (d) up view of position; (e) side view and (f) up view of position 3 and; (g) side view and (h) up view of position 4.

on the nitro groups next to the methyl group, with the remaining nitro group, distinctive of Position 1 adsorption, having a region of electron depletion around it. These patterns of electronic density explain the fact that adsorption from Position 2 is the less favorable energetically.

In Position 3 (Figure 4(c)), one of the nitro groups, due to greater proximity of the surface, interacts more strongly

with  $\text{Mg}^{2+}$  ionic sites. There is electron depletion on the nitro group opposed to the methyl group and as well below the ring.

Adsorption from Position 4 was energetically the most favorable for the two-layer surface; this situation changed for the three-layer surface, being now the second most stable, energetically close (or rather indistinguishable) to the most stable (Position 1). All TNT atoms for Position 4

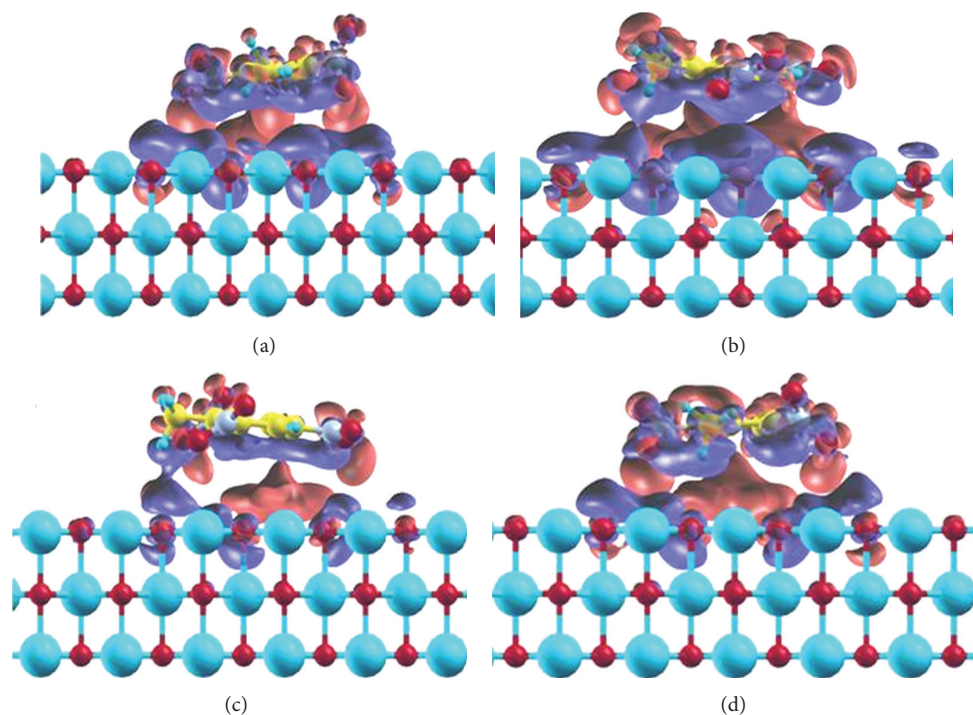


FIGURE 4: Electronic charge density of the systems adsorbed on the MgO surface with three layers, the uppermost fully relaxed. (a) Side view of Position 1; (b) side view of Position 2; (c) side view of Position 3; (d) side view of Position 4. Blue color indicates regions of charge accumulation while red ones indicate charge depletion.

adsorption were polarized, especially the nitro groups next to the methyl group and the methyl group itself, there was also electron depletion below the ring, and the surface was also polarized. This situation, as expected, was not very different for adsorption from Position 1.

#### 4. Conclusion

In this work we studied adsorption of a TNT molecule on a MgO(001) surface using DFT methods combined with periodic boundary conditions. Electronic adsorption energies and electron density difference maps were computed. A large  $5 \times 5$  super-cell was necessary to represent accurately the surface. We investigated desorption from four different initial positions of the TNT molecule and two different representations of the surface, one with two fixed layers of atoms and the other one with three layers, the uppermost being fully relaxed, thereby allowing a thorough investigation of TNT adsorption processes on MgO(001).

In other (unpublished) work, calculations of TNT adsorption on a fully optimized  $\text{Mg}_{36}\text{O}_{36}$  model cluster resulted in adsorption energies about six times larger than present values, thus confirming the importance of an accurate representation of the surface for adsorption studies. We particularly stress here the crucial role played by the Madelung (i.e., long range) potential in the description of the surface, adequately included in the present work.

Overall, the adsorbed molecules converged to a molecule-surface distance of about 3.3 Å. We showed that the presence of an uppermost fully relaxed layer in the three-layer surface representation led to important differences when compared to adsorption on the surface with two fixed layers.

The computed electronic adsorption energies, converged molecule-surface adsorption distances, and electron density difference maps characterized a typical physisorption process, which is dominated by dispersion interactions. The electron density difference maps showed differences and similarities depending on the converged adsorption geometries. For instance, the most stable three-layer adsorptions (Position 1 and Position 4), very close in energy, showed similar features in their electron density difference plots: all atoms, especially the nitro groups, were considerably polarized and there was electron depletion below the molecular ring.

We have shown in this work that TNT desorption on MgO(001) is governed by physical interactions. Despite previous evidence of cooperative effects favoring  $\text{NO}_2$  and chemisorption of similar small molecules on a MgO(001) surface, contrary to our initial expectations, a similar behavior was not found for TNT (with has three nitro groups) adsorption on the same surface. Therefore, although the MgO(001) catalyst did not present a cooperative effect, further theoretical investigations should be done in order to confirm the role of the MgO(001) surface in TNT deactivation. In spite of that, we have showed that the wealth of information DFT calculations, combined with periodic

boundary conditions, can provide for desorption studies of such large molecules as TNT.

## Acknowledgments

This work has been supported by the Brazilian agencies CNPq, Faperj, and CAPES. The authors thank especially Professor M. A. C. Nascimento (UFRJ, Brazil) for providing computer resources for some calculations of this work.

## References

- [1] I. Borges, "Excited electronic and ionized states of N,N-dimethylnitramine," *Chemical Physics*, vol. 349, no. 1–3, pp. 256–262, 2008.
- [2] I. Borges, "Excited electronic and ionized states of the nitramide molecule,  $H_2NNO_2$ , studied by the symmetry-adapted-cluster configuration interaction method," *Theoretical Chemistry Accounts*, vol. 121, no. 5–6, pp. 239–246, 2008.
- [3] I. Borges, A. J. A. Aquino, M. Barbatti, and H. Lischka, "The electronically excited states of RDX (hexahydro-1,3,5-trinitro-1,3,5-triazine): vertical excitations," *International Journal of Quantum Chemistry*, vol. 109, no. 11, pp. 2348–2355, 2009.
- [4] I. Borges, M. Barbatti, A. J. A. Aquino, and H. Lischka, "Electronic spectra of nitroethylene," *International Journal of Quantum Chemistry*, vol. 112, no. 4, pp. 1225–1232, 2012.
- [5] T. F. Moraes and I. Borges, "Nuclear fukui functions and the deformed atoms in molecules representation of the electron density: application to gas-Phase RDX (hexahydro-1,3,5-trinitro-1,3,5-triazine) electronic structure and decomposition," *International Journal of Quantum Chemistry*, vol. 111, no. 7–8, pp. 1444–1452, 2011.
- [6] I. Borges, "Conformations and charge distributions of diazocyclopropanes," *International Journal of Quantum Chemistry*, vol. 108, no. 13, pp. 2615–2622, 2008.
- [7] G. Anders and I. Borges, "Topological analysis of the molecular charge density and impact sensitivity models of energetic molecules," *The Journal of Physical Chemistry A*, vol. 115, no. 32, pp. 9055–9068, 2011.
- [8] R. S. Alvim, I. Borges, D. G. Costa, and A. A. Leitao, "Density-functional theory simulation of the dissociative chemisorption of water molecules on the MgO(001) surface," *The Journal of Physical Chemistry C*, vol. 116, no. 1, pp. 738–744, 2012.
- [9] V. S. Vaiss, R. A. Berg, A. R. Ferreira, I. Borges, and A. A. Leitao, "Theoretical study of the reaction between HF molecules and hydroxyl layers of  $Mg(OH)_2$ ," *Journal of Physical Chemistry A*, vol. 113, no. 23, pp. 6494–6499, 2009.
- [10] V. S. Vaiss, I. Borges, and A. A. Leitao, "Sarin degradation using brucite," *The Journal of Physical Chemistry C*, vol. 115, no. 50, pp. 24937–24944, 2011.
- [11] K. S. Ro, A. Venugopal, D. D. Adrian et al., "Solubility of 2,4,6-trinitrotoluene (TNT) in water," *Journal of Chemical and Engineering Data*, vol. 41, no. 4, pp. 758–761, 1996.
- [12] N. J. Duijm and F. Markert, "Assessment of technologies for disposing explosive waste," *Journal of Hazardous Materials*, vol. 90, no. 2, pp. 137–153, 2002.
- [13] J. M. Conder, T. W. La Point, J. A. Steevens, and G. R. Lotufo, "Recommendations for the assessment of TNT toxicity in sediment," *Environmental Toxicology and Chemistry*, vol. 23, no. 1, pp. 141–149, 2004.
- [14] J. C. Pennington and J. M. Brannon, "Environmental fate of explosives," *Thermochimica Acta*, vol. 384, no. 1–2, pp. 163–172, 2002.
- [15] C. Rajagopal and J. C. Kapoor, "Development of adsorptive removal process for treatment of explosives contaminated wastewater using activated carbon," *Journal of Hazardous Materials*, vol. 87, no. 1–3, pp. 73–98, 2001.
- [16] J. W. Lee, T. H. Yang, W. G. Shim, T. O. Kwon, and I. S. Moon, "Equilibria and dynamics of liquid-phase trinitrotoluene adsorption on granular activated carbon: effect of temperature and pH," *Journal of Hazardous Materials*, vol. 141, no. 1, pp. 185–192, 2007.
- [17] S. J. Chang and Y. C. Liu, "Degradation mechanism of 2,4,6-trinitrotoluene in supercritical water oxidation," *Journal of Environmental Sciences*, vol. 19, no. 12, pp. 1430–1435, 2007.
- [18] S. Y. Oh, P. C. Chiu, B. J. Kim, and D. K. Cha, "Enhancing Fenton oxidation of TNT and RDX through pretreatment with zero-valent iron," *Water Research*, vol. 37, no. 17, pp. 4275–4283, 2003.
- [19] H. S. Son, S. J. Lee, I. H. Cho, and K. D. Zoh, "Kinetics and mechanism of TNT degradation in  $TiO_2$  photocatalysis," *Chemosphere*, vol. 57, no. 4, pp. 309–317, 2004.
- [20] D. C. Schmelling and K. A. Gray, "Photocatalytic transformation and mineralization of 2,4,6-trinitrotoluene (TNT) in  $TiO_2$  slurries," *Water Research*, vol. 29, no. 12, pp. 2651–2662, 1995.
- [21] S. Sawada and K. Nakamura, "Theory of surface rumpling in rock-salt structured ionic crystals," *Journal of Physics C*, vol. 12, no. 6, pp. 1183–1193, 1979.
- [22] M. L. Bailly, C. Chizallet, G. Costentin, J. M. Krafft, H. Lauron-Pernot, and M. Che, "A spectroscopy and catalysis study of the nature of active sites of MgO catalysts: thermodynamic brønsted basicity versus reactivity of basic sites," *Journal of Catalysis*, vol. 235, no. 2, pp. 413–422, 2005.
- [23] M. Miletic, J. L. Gland, K. C. Hass, and W. F. Schneider, "First-principles characterization of  $NO_x$  adsorption on MgO," *Journal of Physical Chemistry B*, vol. 107, no. 1, pp. 157–163, 2003.
- [24] M. M. Branda, C. Di Valentin, and G. Pacchioni, "NO and  $NO_2$  adsorption on terrace, step, and corner sites of the BaO surface from DFT calculations," *Journal of Physical Chemistry B*, vol. 108, no. 15, pp. 4752–4758, 2004.
- [25] C. di Valentin, G. Pacchioni, and M. Bernasconi, "Ab initio molecular dynamics simulation of NO reactivity on the CaO(001) surface," *Journal of Physical Chemistry B*, vol. 110, no. 16, pp. 8357–8362, 2006.
- [26] M. Miletic, J. L. Gland, K. C. Hass, and W. F. Schneider, "Characterization of adsorption trends of  $NO_2$ , nitrite, and nitrate on MgO terraces," *Surface Science*, vol. 546, no. 2–3, pp. 75–86, 2003.
- [27] W. F. Schneider, "Qualitative differences in the adsorption chemistry of acidic ( $CO_2$ ,  $SO_x$ ) and Amphiphilic ( $NO_x$ ) species on the alkaline earth oxides," *The Journal of Physical Chemistry B*, vol. 108, pp. 273–282, 2004.
- [28] P. Broqvist, I. Panas, and H. Grönbeck, "The nature of  $NO_x$  species on BaO(100): an Ab initio molecular dynamics study," *Journal of Physical Chemistry B*, vol. 109, no. 32, pp. 15410–15416, 2005.
- [29] P. Hohenberg and W. Kohn, "Inhomogeneous electron gas," *Physical Review*, vol. 136, no. 3, pp. B864–B871, 1964.
- [30] W. Kohn and L. J. Sham, "Self-consistent equations including exchange and correlation effects," *Physical Review*, vol. 140, no. 4, pp. A1133–A1138, 1965.

- [31] J. P. Perdew and Y. Wang, "Accurate and simple analytic representation of the electron-gas correlation energy," *Physical Review B*, vol. 45, no. 23, pp. 13244–13249, 1992.
- [32] D. Vanderbilt, "Soft self-consistent pseudopotentials in a generalized eigenvalue formalism," *Physical Review B*, vol. 41, no. 11, pp. 7892–7895, 1990.
- [33] M. C. Payne, M. P. Teter, D. C. Allan, T. A. Arias, and J. D. Joannopoulos, "Iterative minimization techniques for ab initio total-energy calculations: molecular dynamics and conjugate gradients," *Reviews of Modern Physics*, vol. 64, no. 4, pp. 1045–1097, 1992.
- [34] A. F. Wells, *Structural Inorganic Chemistry*, Clarendon Press, Oxford, UK, 5th edition, 1984.
- [35] V. E. Henrich and P. A. Cox, *The Surface Science of Metal Oxides*, Cambridge University Press, Cambridge, UK, 1994.